

Investigation into the developing
mechanism of idiopathic scoliosis by
means of computational mechanics

Han SUN

Investigation into the developing mechanism of idiopathic scoliosis by means of computational mechanics

Han SUN

Doctoral dissertation,
Graduate School of Information Science,
Nagoya University

January 2016

Abstract

Investigation into the developing mechanism of idiopathic scoliosis by means of computational mechanics

Idiopathic scoliosis comprises spinal irregularity with lateral curvatures together with rotation without any marked abnormality of the vertebrae or associated musculoskeletal condition. Since almost all cases of the disorder appear during adolescence, particularly during growth spurts, growth has been recognized as associated with the etiology of idiopathic scoliosis in some way. The objective of the present thesis is to investigate the etiology and the developing mechanism of idiopathic scoliosis by means of computational mechanics.

The thesis consists of seven chapters.

Chapter 1 reviews the relevant background literature including the information of the characteristic, the classification, the harm, and the treatments of idiopathic scoliosis. A large number of hypotheses and physical models have been proposed for the pathogenesis of idiopathic scoliosis. From the point of view of the mechanics, we classify these concepts into the following issues. (1) The growth itself is asymmetrical. (2) The buckling by symmetrical growth of the vertebral bodies induces the deformation of scoliosis (the buckling hypothesis). For the buckling hypothesis, we review the literature and points out that Dickson presented an important observation of a flattening of the thoracic spine in the specimens of the idiopathic scoliosis. They identified the trigger of the rotational instability as a median plane asymmetry, that is, the flattening or decreasing of normal thoracic kyphosis at the apex of the curvature, and they declared this instability to be a buckling phenomenon.

In Chapter 2, in order to demonstrate the buckling hypothesis, we introduced the theory for buckling phenomenon caused by the growth of vertebral bodies, and analyzed the buckling phenomena using three types of plate models simplified the spine. We analyzed linear buckling modes caused by the growth deformation using the finite element method, and we confirmed the existence of buckling phenomena and clarified the range of the geometrical parameters in which this buckling occurs. By the comparison of the ranges between the three models, we obtained the following results. (1) The growth of the frontal part of spine in depth around 10 mm from the frontal plain causes the buckling phenomena most easily. (2) The model with physiological curvature enlarges the buckling area than the strait model. (3) The structure having holes in the rear part also enlarges the buckling area. These results support the buckling hypothesis as a cause of initiation of the idiopathic scoliosis.

However, the results in Chapter 2 are only valid for infinitesimal deformation and not applicable to estimate the stability for post-buckling behavior. Thus, in Chapter 3, we conducted the theory for post-buckling deformation caused by the growth of vertebral bodies considering the geometrical nonlinearity, and demonstrated the nonlinear post-buckling simulation using the simple plate model. In these analyses, the buckling modes obtained from the linear buckling analyses of the simple plate model in Chapter 2 were chosen as the initial imperfections of the plate model. To solve unstable nonlinear post-buckling deformation, the incremental Arc-length method was employed. From the results, the stable post-buckling deformations were obtained in almost modes of the simple plate model, while an unstable post-buckling deformation was confirmed after introducing the initial imperfection to the 3rd buckling mode.

In Chapter 4, based on the results from Chapter 2, the similar linear buckling analysis was performed using the spine finite element model without rib cage instead of the simple plate models. The spine finite element model consisted of 69,658 nodes and 59,356 elements. For the boundary conditions, we assumed that the sacrum was fixed. From the results, the 4th buckling mode which is similar to the clinical scoliosis deformity was obtained. By a comparison of different growth regions, we investigated the influence of the region of the buckling

phenomena on the physiological curvature of the spine. We found when the growth of the frontal parts of spine in depth around 10 mm, the spine model was in the easiest state to get buckled. This result accords with the result in Chapter 2.

Chapter 5 explores post-buckling deformations caused by the growth of vertebral bodies using the spine models by the Arc-length Method. The 4th mode obtained from the linear buckling analysis of the spine model in Chapter 4 was chosen as the initial perfection of the spine model for post-buckling analysis. However, we did not obtain any deformation similar to the clinical modes. Thus, we shrank the width of the spine model, and fixed the node at the center of front boundary of C7 in horizontal plane considering the controllability of posture. From the results, the existence of the non-linear buckling phenomena was confirmed. However, the magnitude of the deformations are too small to explain the pathogenesis of the severe deformity observed in patients of idiopathic scoliosis. Thus, although the buckling hypothesis can explain the pathogenesis of the onset in the idiopathic scoliosis, it cannot explain the developing mechanism.

In Chapter 6, in order to investigate the mechanism of progression of the idiopathic scoliosis, the influence of bone remodeling after the buckling was analyzed. The bone remodeling is a phenomenon of absorption and formation of the bone which occurs according to the change in the mechanical and physiological circumstance. In this study, the bone formation was simulated by increasing of the volume of the bone in proportion to the strain distribution which was obtained from the nonlinear post-buckling deformation analysis in Chapter 5, while the bone resorption was simulated by decreasing of the volume of the bone in proportion to the strain distribution. From the results, it is confirmed that the bone formation corrects the original curve, while the bone resorption worsens the original curve. These results suggested that, the bone resorption with respect to strain at post-buckling can be a candidate of the developing mechanism of the idiopathic scoliosis.

Chapter 7 presents the conclusions conducted from this study and suggestions for the future work on the topic. From the investigation in Chapters 2 and 4, since the linear buckling modes are similar to the scoliotic modes, the buckling hypothesis is effective as the pathogen-

esis of the onset in the idiopathic scoliosis. However, from the results in Chapters 3 and 4, since any severe scoliotic curve is not obtained by the post-buckling deformation analysis, it is difficult to explain the pathogenesis of the progression by the buckling hypothesis. On the other hand, the investigation of bone remodeling in Chapter 6 declares that the bone resorption in proportion to the strain at the post-buckling deformation progress the scoliotic curves. Thus, based on the results obtained in the present study, it is concluded that the buckling phenomena with respect to the growth deformation of the vertebral bodies can be a pathogenesis of the onset of the idiopathic scoliosis, and the bone resorption in proportion to the strain at the post-buckling deformation can be a mechanism developing the idiopathic scoliosis.

Contents

Abstract	5
1 Introduction	15
1.1 Spine	15
1.2 Idiopathic scoliosis	17
1.3 The classification of idiopathic scoliosis	20
1.4 The harm	24
1.5 Treatment of scoliosis	26
1.5.1 Nonsurgical treatment	26
1.5.2 Surgical treatment	27
1.6 Etiology of idiopathic scoliosis	28
1.6.1 Physiological etiology	31
1.6.2 Asymmetric growth hypothesis	31
1.6.3 Buckling hypothesis	32
1.7 Objectives of this thesis	34
1.8 Structure of this thesis	35
2 Lin. Buckling Analy. for Plate	37
2.1 Buckling hypothesis	37
2.1.1 Lucas's experiment	38
2.1.2 Dickson's experiment	39
2.1.3 Previous research	39
2.2 Buckling	41
2.2.1 Basics of buckling theory	41
2.2.2 Buckling analysis through FEM	43
2.3 Growth deformation problem	43
2.4 Buckling problem	46

2.5	Finite element analysis	47
2.6	Finite element Models	49
2.6.1	Young's modulus	49
2.6.2	Model 1	51
2.6.3	Model 2	53
2.6.4	Model 3	53
2.7	Results	56
2.8	Discussion	59
2.9	Conclusion	60
3	Nonl. post-buckling analy. for plate	61
3.1	Nonlinear buckling analysis	61
3.2	Arc-length Method	64
3.3	The effect of geometric imperfection	65
3.4	Nonl. buckling analy. by FEM	66
3.4.1	Elastic deformation problem by means of non-elastic strain	66
3.4.2	Nonlinear buckling analysis	69
3.5	Post-buckling analysis in Abaqus	72
3.6	Model	72
3.7	Result	75
3.8	Discussion	75
3.9	Conclusion	81
4	Lin. Buckling Analy. for Spine	83
4.1	The structure of the spine	83
4.1.1	Classification of bone	83
4.1.2	The structure of the spine	84
4.1.3	The joints of vertebrae	86
4.2	Previous researches	88
4.3	The manufacture of the spine model	96
4.4	The finite element model of spine	100
4.4.1	The element	100
4.4.2	The boundary conditions and growth region	104
4.5	Results	108
4.6	Discussion	117
4.7	Conclusion	118

5	Nonl. post-buckling analy. for spine	119
5.1	The normal model	119
5.2	The narrow model	120
5.2.1	The spine model with half width	120
5.2.2	The new boundary condition	125
5.3	Discussion	125
5.4	Conclusion	128
6	Bone remodeling	131
6.1	Bone remodeling	131
6.2	Remodeling analysis	133
6.3	Results and discussion	135
6.4	Conclusion	141
7	Conclusion	143
7.1	Achievement of this research	143
7.2	Future work	145
	References	146

List of Figures

1.1	Spine [1]	16
1.2	A radiograph of a 11-year-old female idiopathic scoliosis patient [2]	18
1.3	Cobb angle	19
1.4	The classification for idiopathic scoliosis [3]	21
1.5	King's classification	22
1.6	Lenke's classification	24
1.7	Lenke's classification: lumbar spine modifiers A, B, and C	25
1.8	Lenke's classification : Sagittal Thoracic Modifiers (−, N, or +)	26
1.9	Surgery with Harrington instrumentation [4]	29
1.10	Surgery with Luque instrumentation [4]	29
1.11	Surgery with Cotrel-Dubousset instrumentation [4]	30
2.1	Lucas horizontal lateral loading test [5]	38
2.2	Changes in height with aging for adolescents [6]	40
2.3	Fourth buckling mode from previous research [7]	41
2.4	Euler buckling	42
2.5	Lucas's horizontal lateral loading test method [5]	49
2.6	The plate model in order to repeat Lucas's loading test [5]	50
2.7	Model 1	52
2.8	Maps of the existence of buckling modes when $g = 10$ mm for Model 1	52
2.9	Model 2	54
2.10	Maps of the existence of buckling modes when $g = 10$ mm for Model 2	54

2.11	Model 3	55
2.12	Maps of the existence of buckling modes when $g = 10$ mm for Model 3	55
2.13	Shapes of the buckling modes for Model 1 at $(w_F, w_B) = (16 \text{ mm}, 16 \text{ mm})$ when $g = 10 \text{ mm}$ via RADIOSS 11.0 (Altair Engineering, Inc.)	57
2.14	Shapes of the buckling modes for Model 1 at $(w_F, w_B) = (16 \text{ mm}, 16 \text{ mm})$ when $g = 10 \text{ mm}$ via Abaqus 6.12 Edition (Abaqus, Inc.)	58
2.15	Dependency of depth g of growth domain on the buckling coefficient ζ for Model 1 and Model 2 at $(w_F, w_B) = (16 \text{ mm}, 16 \text{ mm})$	59
3.1	Typical unstable static problem	62
3.2	The shortcomings of classical Newton-Raphson Method	62
3.3	The Arc-length Method	63
3.4	A schematic principle for Imperfection [8]	66
3.5	Flowchart of post-buckling analysis procedure in Abaqus	73
3.6	The plate model	74
3.7	The 1st Mode from nonlinear growth deformations of plate model with initial imperfections ($\lambda = 12.16$)	76
3.8	History of load proportionality factor for the 1st Mode	76
3.9	The 2nd Mode from nonlinear growth deformations of plate model with initial imperfections ($\lambda = 45.59$)	77
3.10	History of load proportionality factor for the 2nd Mode	77
3.11	The 3rd Mode from nonlinear growth deformations of plate model with initial imperfections ($\lambda = 50.54$)	78
3.12	History of load proportionality factor for the 3rd Mode	78
3.13	The 4th Mode from nonlinear growth deformations of plate model with initial imperfections ($\lambda = 9.359$)	79
3.14	History of load proportionality factor for the 4th Mode	79
3.15	History of load proportionality factor for the 3rd mode	80
4.1	The structure of the bone	84
4.2	Spine [1]	85
4.3	Cross sectional view of lumbar vertebrae [1]	87
4.4	Articular capsule of thoracic vertebrae [1]	87
4.5	Previous spine model (1995)	89

4.6	Previous spine model (1996)	90
4.7	Typical buckling modes [9]	92
4.8	Critical growth at generating buckling phenomena . . .	93
4.9	Loading factor vs. displacement at the front-center point on the 8th thoracic vertebra [10].	94
4.10	Displacement of the center points in all vertebrae [10].	95
4.11	Finite element division for T8 thoracic vertebrae	97
4.12	The finite element model of the 2nd cervical vertebra .	97
4.13	The finite element model of the 5th cervical vertebra .	98
4.14	The finite element model of the 7th thoracic vertebra .	98
4.15	The finite element model of the 3rd lumbar vertebra . .	99
4.16	Finite element mesh for T9-T10	101
4.17	Finite element model of spine with rib cage	102
4.18	Finite element model of spine without rib cage	103
4.19	The boundary condition for the spine model	106
4.20	Growth region [11]	107
4.21	The 1st Mode of spine model ($\zeta_1 = 1.046$)	109
4.22	The 2nd Mode of spine model ($\zeta_2 = 2.272$)	110
4.23	The 3rd Mode of spine model ($\zeta_3 = 2.521$)	111
4.24	The 4th Mode of spine model ($\zeta_4 = 5.203$)	112
4.25	The 5th Mode of spine model ($\zeta_5 = 5.936$)	113
4.26	The 6th Mode of spine model ($\zeta_6 = 7.242$)	114
4.27	The 7th Mode of spine model ($\zeta_7 = 13.564$)	115
4.28	The 8th Mode of spine model ($\zeta_8 = 15.094$)	116
5.1	The boundary condition for the spine model	121
5.2	The 4th linear mode of spine model ($\zeta_4 = 5.203$)	121
5.3	The nonlinear post-buckling analysis for the 4th Mode ($\lambda = 28.89$)	122
5.4	History of load proportionality factor for the spine model	122
5.5	The boundary condition for the half width spine model	123
5.6	The 4th linear buckling mode of half width spine model ($\zeta = 12.701$)	123
5.7	Nonlinear growth deformations of half width spine mod- els with initial imperfections of the 4th buckling mode ($\lambda = 72.95$)	124

5.8	History of load proportionality factor for the half width spine model	124
5.9	The new boundary condition for the half width spine model	126
5.10	Nonlinear growth deformations of half width spine models with initial imperfections of the 4th buckling mode ($\lambda = 90.1$, Cobb angle $\alpha = 7.5^\circ$)	127
5.11	History of load proportionality factor for the half width spine model	127
5.12	The 4th linear buckling mode of half width spine model ($\zeta = 12.701$)	129
6.1	Fung Principle	132
6.2	Bone remodeling	134
6.3	The point when Arc-length $\lambda = 50$	136
6.4	The strain distribution during nonlinear post-buckling analysis when Arc-length $\lambda = 50$	137
6.5	The boundary condition for bone remodeling analysis .	138
6.6	Comparison between before bone formation and after bone formation ($\lambda = 50$).	139
6.7	Comparison between before bone resorption and after bone resorption ($\lambda = 50$) (The biggest spatial displacement is around 16.97mm.)	140

List of Tables

4.1	Using rate for each type of element	101
4.2	Finite element qualities of the spine model	105
4.3	Material properties of each vertebra	105
4.4	Growth proportion α	106
4.5	Growth rate of vertebrae for normal girls	117
4.6	Load Proportionality Factor at the 4th buckling ζ_4 with respect to depth of growth domain Ω_G	117

Chapter 1

Introduction

Scoliosis is a condition in which the spine curves sideways including rotation or twisting. Idiopathic scoliosis is the most common type of scoliosis, that appear during adolescence, especially during growth spurts. The cause of this disorder still remains unknown.

A brief description of the following sections is given below: Section 1.1 introduces the construction of the human spine. Section 1.2 presents the definition and characteristic of idiopathic scoliosis. The natural history of classification of idiopathic scoliosis is stated in Section 1.3. The harm of idiopathic scoliosis is introduced in Section 1.4. Section 1.5 explains the current spectrum of considerations for surgery treatment and bracing treatment. Section 1.6 reviews the current issues of debate about etiology of idiopathic scoliosis. Section 1.7 summarizes the background, previous study and objective of this research. Lastly, the structure of this thesis is introduced in Section 1.8.

1.1 Spine

The human vertebral column is also named as the backbone or spine. There are a total of 33 vertebrae in the human vertebral column. These vertebrae are divided into five regions, the cervical spine, thoracic spine, lumbar spine, sacrum and coccyx [12]. There are seven cervical vertebrae, twelve thoracic vertebrae and five lumbar vertebrae, as shown in Figure 1.1.

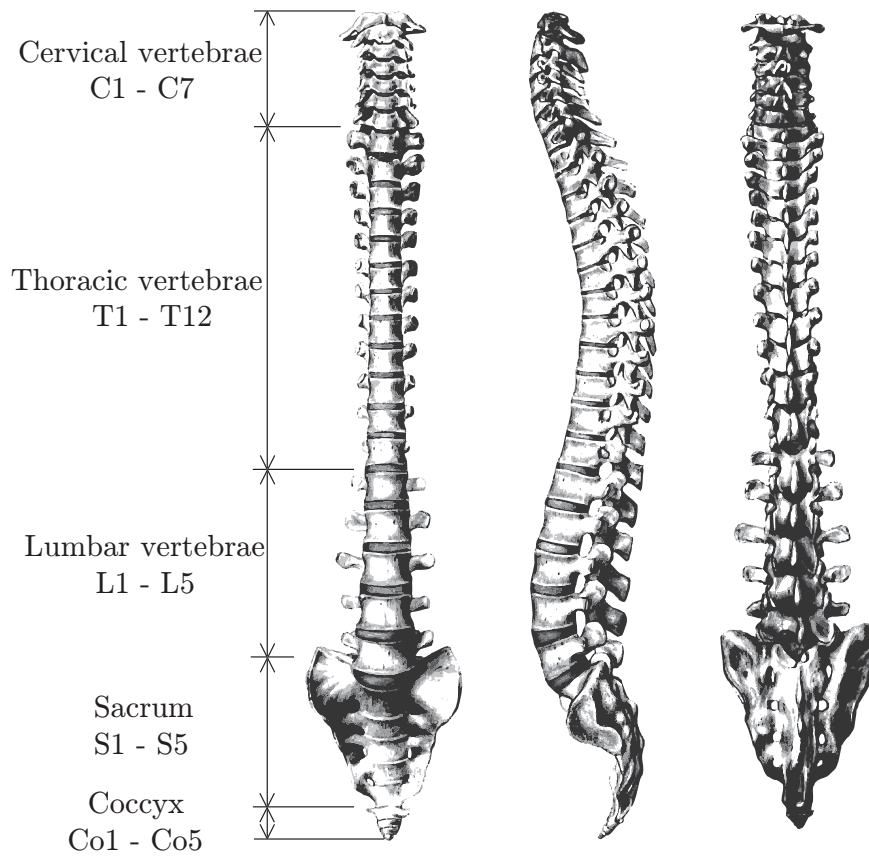


Figure 1.1: Spine [1]

Spinal curvature disease can be classified into three types as below.

(1) Kyphosis.

Kyphosis refers to the top back of spine (in the thoracic or thoracolumbar spine) significantly outwards, and commonly called as roundback.

(2) Lordosis.

Lordosis refers to an excessive curvature at the lower back of the spine, and commonly named as sway back.

(3) Scoliosis.

Scoliosis refers to the spine curves right or left including rotation or twisting, occurring in 0.5% of the population. There are also several different types of scoliosis classified based on the patient's age. They are the infantile scoliosis (from birth to 3 years old), juvenile scoliosis (from 3 to 9 years old), and idiopathic scoliosis (10 to 18 years old). The idiopathic scoliosis is the most common type with unknown hypothesis on the etiology.

1.2 Idiopathic scoliosis

Idiopathic scoliosis comprise spinal irregularity with lateral curvatures together with rotation without any marked abnormality of the vertebrae or associated musculoskeletal condition. The cause of this disorder still remains unknown. Since almost all cases of the disorder appear during adolescence, particularly during growth spurts, growth has been recognized as associated with the etiology of idiopathic scoliosis in some way.

The degree of curvature for scoliosis is measured by Cobb angle from a radiograph on the coronal plane. The Cobb angle is defined as the angle between the two lines drawn parallel to the superior endplate of the superior end vertebra and parallel to the inferior endplate of the inferior end vertebra [13], as shown in Figure 1.3. A Cobb angle over 10° is generally considered as clinically significant scoliosis.



Figure 1.2: A radiograph of a 11-year-old female idiopathic scoliosis patient [2]

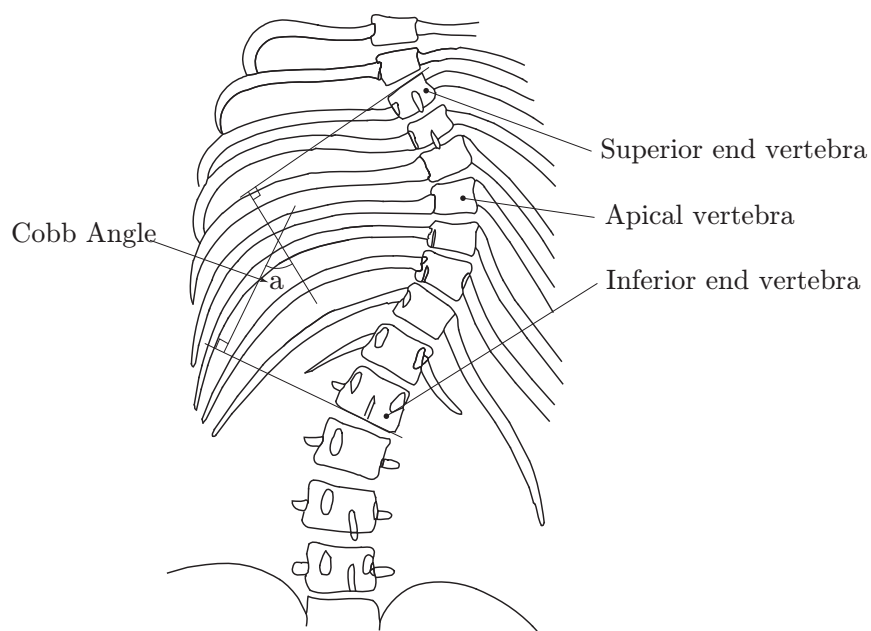


Figure 1.3: Schematic example of the Cobb angle [14]

The prevalence of idiopathic scoliosis is estimated 2% to 3% of adolescence whose Cobb angle is more than 10° [15]. The Cobb angle around 40° makes up 0.1% of the idiopathic scoliosis population [16]. The scoliotic curves between 20° and 30° are generally 0.3 to 0.5% of the idiopathic scoliosis population.

Idiopathic scoliosis also has a predominance of female patients. The male-to-female ration is around 1:10 for the Cobb angle greater than 30° [17]. Ueno [18] studied the prevalence of Cobb angle of Japanese children over 10 in an 11 to 12 year olds age group and a 13 to 14 year olds age group. The prevalence was 0.04% in 11 to 12 year olds and 0.25% in 13 to 14 year olds for the boys. Unfortunately, in the girls groups, the prevalence was 0.78% in 11 to 12 year olds and 2.51% in 13 to 14 year olds.

1.3 The classification of idiopathic scoliosis

Several classification systems for idiopathic scoliosis have been represented and widely used around the world. However, each system still needs to be modified for various shortcomings.

Ponseti's Classification

Ponseti and Friedman [19] firstly made classification of idiopathic scoliosis in 1950. This system is defined on the basis of scoliostic curves and location of the spine. The four types of scoliosis are called as thoracic, thoracolumbar, lumbar and double major, which are shown in Figure 1.4. However, this simple classification does not satisfy the needs to formulate strategies for care [20].

King's Classification

King et al. [21] proposed a new classification system which is more accurate and useful than Ponseti's Classification systems in 1983. Figure 1.5 shows the classification where

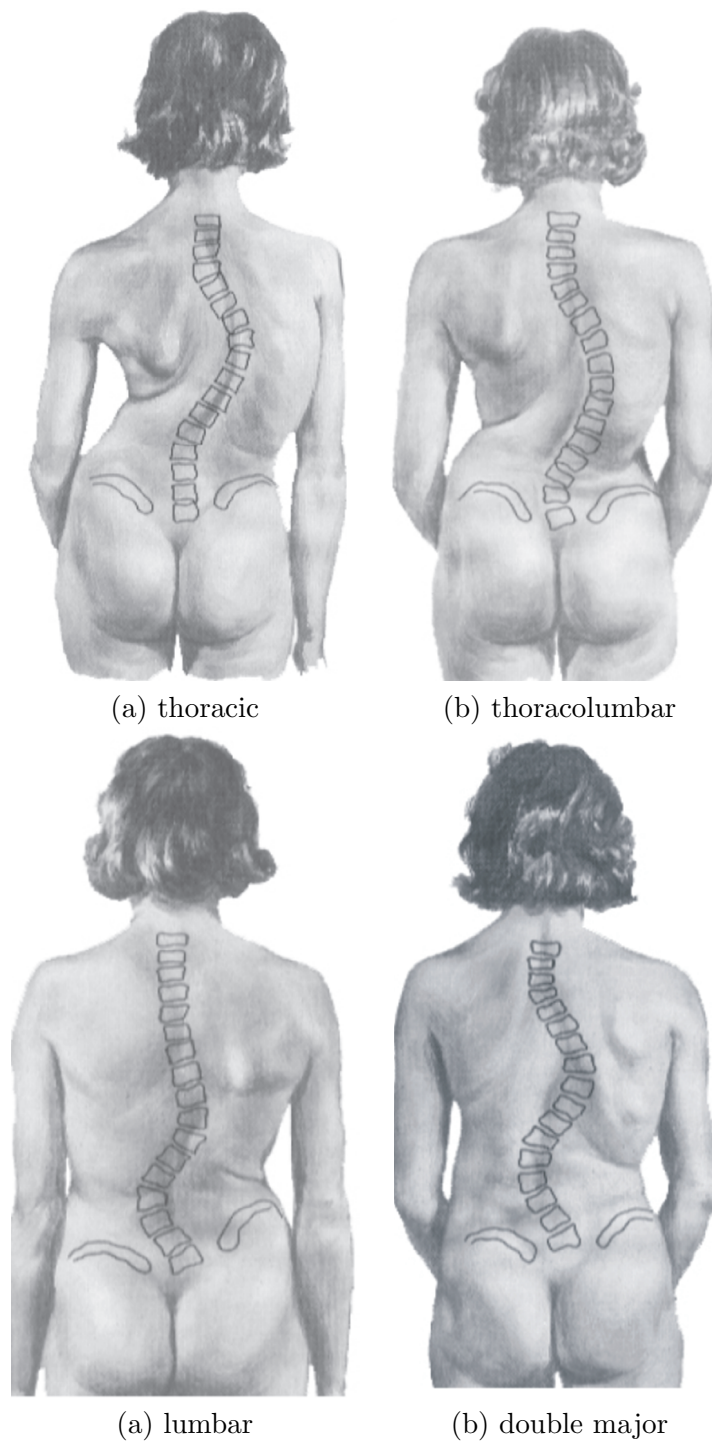


Figure 1.4: The classification for idiopathic scoliosis [3]

Type I Thoracic and lumbar curve, the lumbar curve has bigger magnitude and more rigid,

Type II Thoracic and lumbar curve, the thoracic curve has bigger magnitude and more rigid,

Type III Single thoracic curve without lumbar curve,

Type IV Long thoracic curve with L4 tilted into curve,

Type V Double thoracic curve.

It is helpful to treatment strategy considering the curve pattern of scoliosis. Since King's classification systems offered more appropriate guidelines, Harrington instrumentation was widely used as a kind of scoliosis instrumentation in the early 1980s [22]. Nevertheless, the King's classification is not a complete system for all scoliosis types, because of the ignore of double major and triple curves [20].

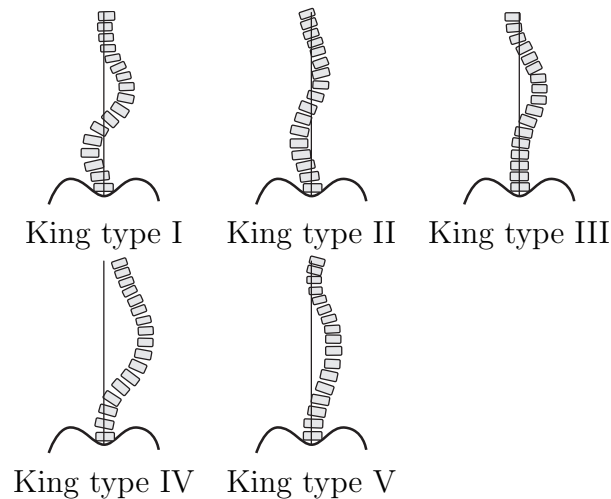


Figure 1.5: King's classification [23]

Lenke's Classification

On the basis of King's classification, Lenke et al. [24] [25] [26] created a new classification system to address the potential problems. The Lenke's Classification was theorized to consist of three components: curve type (Type 1 to 6), a sagittal thoracic modifier (−, N or +), and lumbar spine modifier (A, B or C). Figure 1.6 shows the classification where

Type 1 main thoracic,

Type 2 double thoracic,

Type 3 double major,

Type 4 triple major,

Type 5 thoracolumbar/lumbar (TL/L),

Type 6 thoracolumbar/lumbar - main thoracic (TL/L-MT),

Lumbar Modifier A The central sacral vertical line (CSVL) falls between lumbar pedicles up to stable vertebra,

Lumbar Modifier B The central sacral vertical line (CSVL) falls between medial border of lumbar concave pedicle and lateral margin of apical vertebral body or bodies,

Lumbar Modifier C The central sacral vertical line (CSVL) falls medial to lateral aspect of lumbar apical vertebral body or bodies.

and

N Normal,

PT Proximal thoracic,

TL Thoracolumbar,

PT+TL Proximal thoracic and thoracolumbar.

The Lenke's classification offers significant information for the type of surgery and other treatments. Although comparing with other classifications it is much more reliable and accurate, the Lenke's classification also cannot be called perfect. In some cases, the surgery type chosen based on the Lenke's classification cannot match the clinical scoliosis type [27] [28] [29].

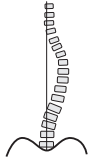
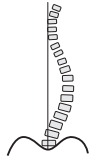
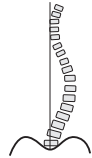
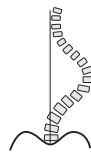
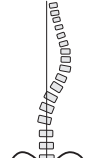

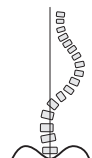
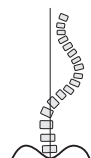
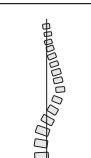
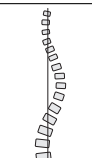
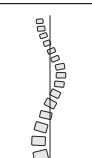
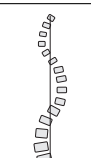
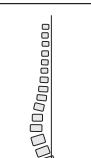
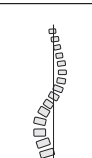
Lumbar Spine Modifier	Type 1	Type 2	Type 3	Type 4	Type 5	Type 6
A						
B						
C						

Figure 1.6: Lenke's classification [23]

1.4 The harm

In general, the scoliosis threatens vital organs, specifically the lungs and heart. If the Cobb angle exceeds 70° , the twisting of the spine can cause the ribs to press against the lungs, do harm to breath, cause lack of oxygen, and even damage to the heart. If the Cobb angle is

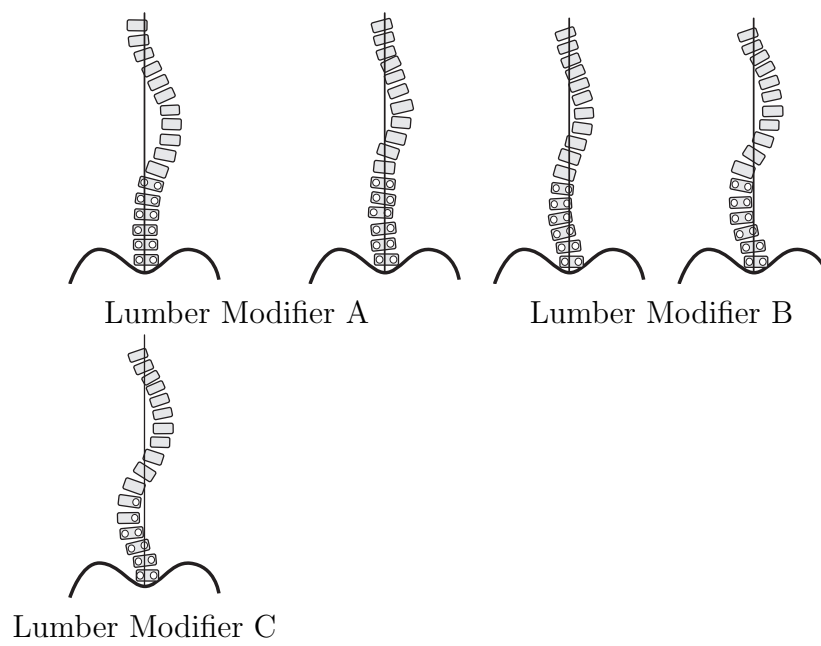


Figure 1.7: Lenke's classification: lumbar spine modifiers A, B, and C (CSVL = Center Sacral Vertical Line) [23]

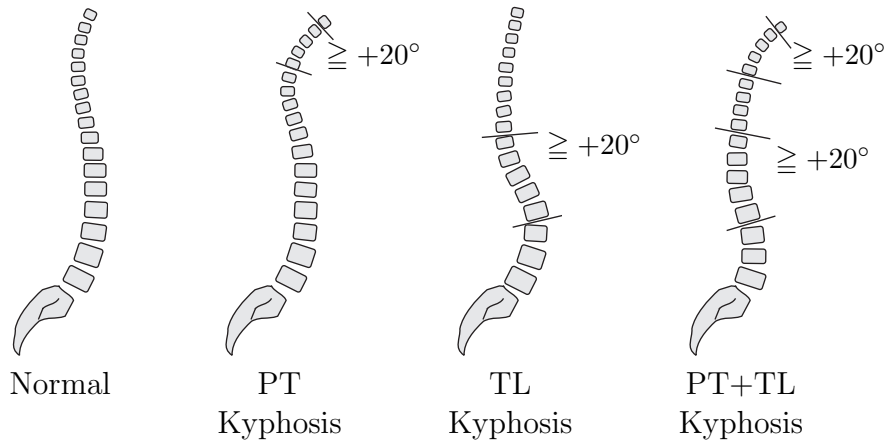


Figure 1.8: Lenke's classification: Sagittal Thoracic Modifiers ($-$, N , or $+$) [23]

over 100° , patients are susceptible to lung infections, pneumonia and even death.

Stuart et al. [30] studied 194 patients with untreated adolescent idiopathic scoliosis between 1932 and 1948. They noticed the backache was common for the patients and found the mortality rate was 15%. If patients with severe scoliosis do not accept treatment, the spine would continue to progress slightly in their rest life.

1.5 Treatment of scoliosis

The treatment for idiopathic scoliosis approaches vary internationally, and can be classified into two types, the nonsurgical treatment and surgical treatment.

1.5.1 Nonsurgical treatment

There are different kinds of nonsurgical methods to treat idiopathic scoliosis, such as traction treatment, bracing treatment and so on. Bracing treatment is widely used to avoid surgery.

Patients with a curve that is between 20° to 30° and still under growth remaining are recommended to take bracing treatment. There are many kinds of brace designed to match different types of scoliotic curves. The brace is used to wrap around the patient body along with a pelvic unit. The main objective of bracing treatment is to prevent the progression of scoliotic curves for the growing children. It can not be used to reduce the degree of the curves. Some researchers found bracing treatment is unable to heal patients whose scoliotic curves are more than 45° [31]. If the patient has curve degree greater than 30° and almost mature, bracing treatment may not be suitable.

There are also some other nonsurgical treatments such as surface electrical stimulation [32], gymnastics [33], plantar orthosis [34], cast correction [35], and so on. However, these treatments are available for the mild scoliosis patients. For the severe patients, the surgical treatment maybe suitable option. At present, the spine medical community advocates bracing treatment as the only nonsurgical treatment for idiopathic scoliosis.

1.5.2 Surgical treatment

Surgical treatment is recommended for patients who have scoliotic curves more than 30° while still growing, or are continuing to progress more than 30° when growth stopped.

In 1962, Harrington [36] claimed a method to treat scoliosis by poster fusion which has widely practiced operation at that time. The Harrington system consists of a distraction rod and two hooks at the ends of the rod, as shown in Figure 1.9. The distraction rod can attach to the spine with the two hooks. This system can help correct the scoliotic curve by stretching or distracting the spine. This method is so successful that remained popular for more than 20 years.

In the early 1970's, Luque [37] devised a more stable and flexible systems named segmental spinal instrumentation (SSI) with two flexible L-shaped rods and wires, as shown in Figure 1.10. The difference from the Harrington systems is the wires which are threaded through the canal at every vertebra. The wires are also used as the multiple points of fixation around the rods. This system can also help correct the scoliotic curves with rotation.

In 1984, Cotrel and Dubousset [38] [39] developed a new system named Cotrel-Dubousset instrumentation involves two flexible rods and multiple hooks. This system consists of two steel rods which allows segmental fixation through conical pedicle screws and lamina hooks, as shown in Figure 1.11. Compared with early systems, the Cotrel-Dubousset instrumentation offers better lateral and frontal curve correction even with rotation, and reduction in deformation of rib hump.

Finite element method (FEM) is also used before spinal surgery to predict the outcome of the surgery, comparing the different instrumentations and various type of scoliotic curves between different patients. In 1993, Stockes [40] used finite element models with individual geometry from 3D stereo roentgenographic reconstructions of the scoliotic spine, and tested the application of these models to simulation of Harrington distraction rod surgery. Gardner-Morset [41] also examined the derotation maneuver using Cotrel-Dubousset instrumentations through finite element simulations.

1.6 Etiology of idiopathic scoliosis

Intensive research is ongoing throughout the world, and many possible causal factors and theories have been evaluated. Genetic factors and melatonin have been suggested to play an important role of idiopathic scoliosis, but no genes or mechanism have been demonstrated with this etiology.

The function of the spine is to support the structure of the body, and thus mechanical phenomena can be considered to be the cause of the spine being bent. In order to predict the natural history of this condition in a patient and to estimate the effects of treatment, the mechanical aspects of the etiology are more important than any genetic or physiological factors.

A large number of hypotheses and physical models have been proposed for the pathogenesis of idiopathic scoliosis. From the point of view of the mechanics of the spine, these concepts can be divided into two systems as follows: the growth itself is asymmetrical, or (the buckling hypothesis) the buckling is induced by symmetrical growth of the

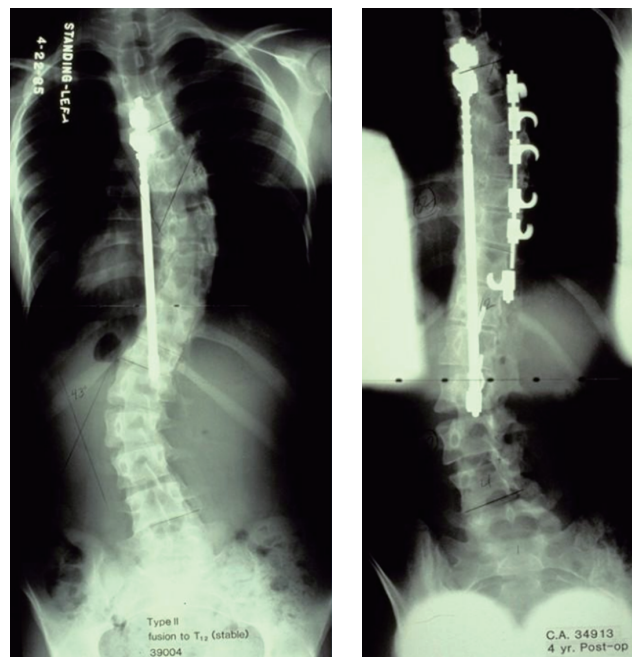


Figure 1.9: Surgery with Harrington instrumentation [4]

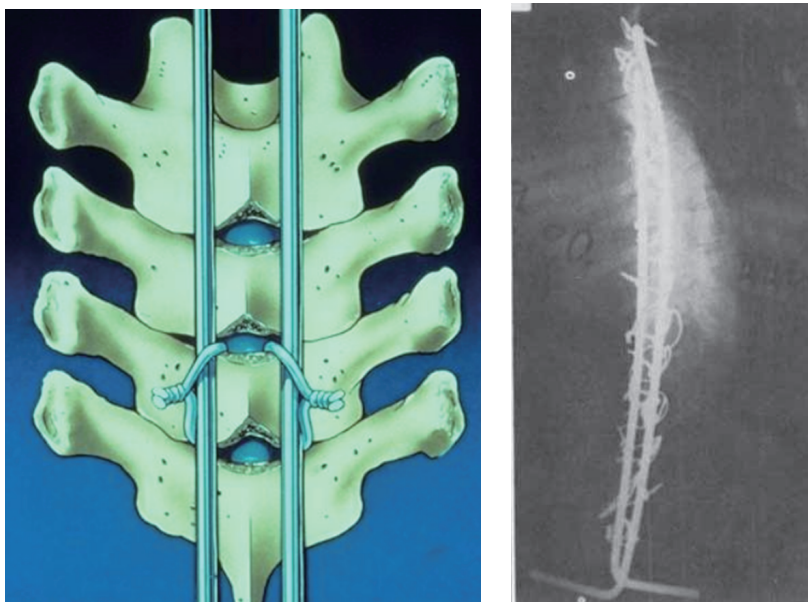


Figure 1.10: Surgery with Luque instrumentation [4]

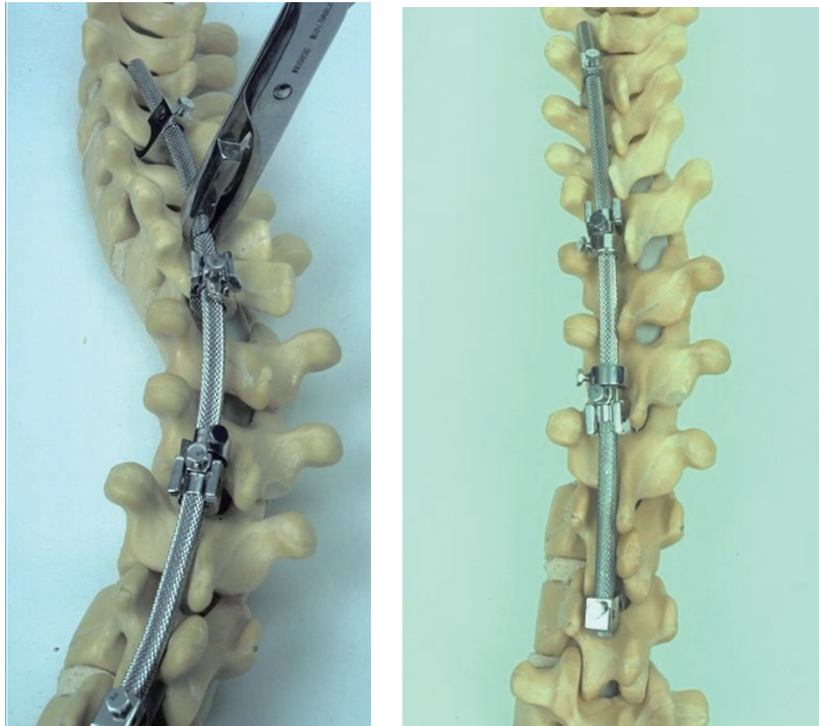


Figure 1.11: Surgery with Cotrel-Dubousset instrumentation [4]

vertebral bodies. The details of asymmetrical growth and buckling etiology will be discussed in the next subtopic.

1.6.1 Physiological etiology

The role of genetic factors or hereditary in the cause of idiopathic scoliosis has a widespread influence.

Harrington [42] investigated the relationship between morbidity and general population. Harrington found a 27% prevalence of patients who had mother also had a scoliotic curve that exceeded 15°. Population studies reflects the fact that 11% of the first-degree relatives are affected, as are 2.4% of second-degree relatives, and 1.4% of third-degree relatives. However, Lowe denied this kind of family sample and claimed it is difficult to yield exact evidences for genetic linkage [43].

Patrick et al. [44] selected 57 individuals for genotyping, and investigated chromosomal relationship on blood lymphocytes from individual in every family. One of the pedigrees of families with a strong evidence that a potential scoliotic gene lays in two chromosomes. However, Patrick found no dominant idiopathic scoliosis gene has been identified.

The abnormality in melatonin metabolism also thought to cause idiopathic scoliosis. Some scientists indicated animals such as chickens, rats with pinealectomy which could decrease melatonin can also result in scoliosis. However, this etiology can not be proved from other reports [45] [46]. Moreover, patients with idiopathic scoliosis are also able to form melatonin, or impaired sleep or immune function. On the basis of the available data, it remains unclear whether melatonin can cause idiopathic scoliosis or not. In terms of physiological factors, no mechanism associated with bending has been proven to have a correlation with melatonin [47] [48]. Moreover, it seems unlikely that scoliosis just results from the absence of melatonin. Future research is also needed to explore the relationship between melatonin production and growth mechanisms.

1.6.2 Asymmetric growth hypothesis

For the hypothesis of asymmetrical growth, Normelli et al. [49] studied the length and ash weight of ribs in cadaveric specimens from normal women and scoliosis female patients. They found the rib on the concave side were longer and slender between the patients with right convex thorax idiopathic scoliosis and the group of normal females. They also found the asymmetric rib growth is the beginning of the rotation and deviation of the scoliotic spine.

Sevastik et al. [50] compared the growth of normal adult rabbits groups and another groups whose ribs were elongated on the right side by 1 cm by application of a metallic expander. They found the force generated by mechanical elongation of one rib developed the scoliosis, rotation of the vertebrae, and a decrease in the sagittal curvatures of the spine.

Stokes and Laible [51] put asymmetrical growth into a human thorax finite element model to examine the hypothesis that asymmetrical growth might result in the scoliosis deformation. Their findings produced spinal curves, which are too small to demonstrate the curvatures of scoliosis patients.

Stokes and Gardner-Morse [52] found it seems impossible that scoliosis can be explained in terms of forces such as asymmetric thoracic growth, or asymmetric vertebral development, after investigating with a FEM ligamentous spine. Stokes et al. [53] also developed a rat tail model to investigate the hypothesis that vertebral wedging during growth to scoliosis results from asymmetric loading in a “vicious cycle.” The results confirmed that vertebral growth is modulated by loading, according to the Hueter-Volkman principle.

Hutnh et al. [54] later incorporated growth modulation and pedicle growth into a spine finite element model. They found simulations with asymmetrical pedicle geometry did not produce scoliotic curves, rotation of spine, or wedging.

1.6.3 Buckling hypothesis

For the buckling hypothesis, we reviewed the literature and investigated the buckling phenomenon induced by the growth of vertebral bodies. We focused on remarks on flattening of the thoracic spine

during growth spurt. Adams [55] in 1865 pointed out the lordosis occurs in the thoracic region. Dickson et al. [56] [57] [58] presented an important observation of a flattening of the thoracic spine during a growth spurt. They identified the trigger of the rotational instability as a median plane asymmetry, that is, the flattening or reversal of normal thoracic kyphosis at the apex of the curvature, and they declared this instability to be a buckling phenomenon.

Porter [59] investigated the degree of spine deformity of the patients who had probable idiopathic scoliosis during the adolescent growth spurt, and compared the discrepancy in length of the vertebral canal and the anterior spinal column in skeletons. They found there may be impaired growth in the length of the spinal cord, the posterior parts are tethered, and when the spine continue to grow, they become lordotic and then rotate.

Chu et al. [60] claimed that there was obvious reduction of vertebral column ratios in the idiopathic scoliosis patients, and declared an abnormal growth between the neural and the skeletal systems. They assert the functional tethering and relative shortening of spinal cord might result in the idiopathic scoliosis.

Shinoda et al. [61] [62] paid attention on the influence from the restraint of rib cage to idiopathic scoliosis. They claimed the existing of the rib cage makes the buckling phenomenon occurs with rapidly growing of spine, which causes the spine to become the scoliotic shape.

For years, predecessors in this research reviewed the literature and investigated the buckling phenomenon induced by the growth of vertebral bodies [63] [64]. In an attempt to confirm the buckling hypothesis, a numerical simulation of growth and the resulting buckling phenomena was done by means of finite element analysis. It previously was observed that growth was induced in the T4 to T10 vertebrae. Only the sacrum was assumed to be stationary. From the growth analysis, a deformation process that mitigated thoracic kyphosis was obtained as observed in healthy children during early adolescence. From the buckling analysis, the first to the fourth buckling modes that correspond to the first side bending, first forward bending, first rotation, and second side bending modes were obtained. The shape of the fourth buckling mode (second side bending mode) was in good agreement with the clinical shape. Considering the potential for controlling these modes

by posture change, it is concluded that the second bending mode in the coronal plane is one of the most likely etiologic candidates in the mechanics of thoracic idiopathic scoliosis.

Aoyama et al. [10] developed a program to analyze deformation histories caused by the growth of vertebral bodies considering the geometrical nonlinearity and investigated buckling phenomena. We assumed that growth represents generation of non-elastic bulk strain. To exclude modes correctable by posture change, we considered constraints at the cervical spine. Using the developed program, we analyzed deformation histories induced by the growth of vertebral bodies and obtained deformation histories including buckling phenomena with side-bending modes similar to clinical curves. However, the magnitudes of deformations were in the sub-millimeter order that is too small for the etiology of idiopathic scoliosis by itself.

1.7 Objectives of this thesis

A large number of hypotheses and physical models have been proposed for the pathogenesis of idiopathic scoliosis. For the buckling hypothesis, we reviewed the literature and investigated the buckling phenomenon induced by the growth of vertebral bodies. Dickson et al. [56] presented an important observation of a flattening of the thoracic spine during a growth spurt. They identified the trigger of the rotational instability as a median plane asymmetry, that is, the flattening or reversal of normal thoracic kyphosis at the apex of the curvature, and they declared this instability to be a buckling phenomenon.

Based on Dickson's buckling hypothesis, predecessors in this research used the linear buckling theory to analyze the buckling phenomenon induced by the growth of vertebral bodies using finite element models of the spine. Using a commercial program (MSC.Nastran 7.0), the fourth and sixth buckling modes were obtained, which are similar to the clinical single and double-major curves, respectively [64].

However, when using a program based on nonlinear buckling theory, no clear buckling modes that were similar to the clinical modes could be observed [10]. After this investigation, the linear buckling modes were reanalyzed by using another commercial program, and

this program did not identify any buckling phenomena.

This led us to wonder whether the buckling phenomenon actually existed, and so, as presented here, we returned to the starting point. We used three types of simple model having different properties to confirm the existence of the buckling phenomenon and we then clarified the range in which the buckling phenomena occur. The reason why we use the simple models is to show clearly the buckling mechanism induced by the growth of vertebral bodies even through different softwares. We need to compare the results of the three models in order to evaluate the reliability of buckling hypothesis. After the linear buckling simulations, the existence of the nonlinear post-buckling phenomena is also needed to be confirmed by the simple plate model.

If the buckling hypothesis could be confirmed by using simple plate models, we would use finite element model of spine to investigate whether this hypothesis is the cause of initiation of the idiopathic scoliosis or not. Moreover, not only the buckling hypothesis is examined, the developing mechanism of idiopathic scoliosis is also investigated by FEM in this research.

1.8 Structure of this thesis

A brief description of the following chapters are given as followed.

Chapter 1 reviews the relevant background literature including the information of the characteristic, the classification, the harm, the treatments of idiopathic scoliosis.

Chapter 2 explores the linear buckling behaviour of simple models to investigate the buckling hypothesis. We assumed that the growth of the vertebral bodies can be modeled by the generation of a non-elastic bulk strain. We use FEM to analyze linear buckling modes caused by the growth deformation, and we confirm the existence of the buckling phenomena and clarify the range of the geometrical parameters in which this buckling occurs. Our results support the buckling hypothesis that a flattening or reversal of normal thoracic kyphosis at the apex of the curvature of the spine causes the buckling phenomenon.

Chapter 3 presents post-buckling simulations caused by the growth considering the geometrical nonlinearity using the simple plate models.

To solve unstable nonlinear buckling behaviors, the incremental Arc-length Method is employed. From the results, the stable post-buckling deformations were obtained in almost simple plate models, while an unstable post-buckling deformation was confirmed after introducing the initial imperfection to the 3rd buckling mode.

Chapter 4 introduces the details of the spine finite element model we used in this study. The linear buckling analysis of the spine model is investigated, based on the results we got from the simple plate models. The 4th buckling mode which is similar to the clinical scoliosis deformity were obtained. By a comparison of different growth regions, we investigate the influence of the region of the buckling phenomena on the physiological curvature of the spine and the intervertebral articulation.

Chapter 5 explores post-buckling simulations caused by the growth of vertebral bodies considering the geometrical nonlinearity using spine models by Arc-length Method. From the results, the existence of the non-linear buckling phenomena was confirmed in the spine model with half width. Thus, the pathogenesis of the onset in the idiopathic scoliosis can be explained by the buckling hypothesis. However, the magnitudes of the post-buckling deformations are too small to explain the pathogenesis of the severe deformity observed in patients of idiopathic scoliosis.

Chapter 6 extends the nonlinear remodeling simulations for the spine models with the growth data from the post-buckling simulation. The bone formation and resorption are simulated by positive and negative volume changes in proportion to the strain from the post-buckling simulations. The results suggests the bone resorption caused the severe deformity as clinical scoliotic curves.

Chapter 7 presents the conclusions produced from the study and suggestions for the future work on the topic.

Chapter 2

Linear Buckling Analysis for Plate Model

This chapter presents the linear buckling theory and the linear buckling analysis by using simple plate models.

Firstly, the origin of buckling hypothesis and previous studies are introduced in Section 2.1. The basic information of linear buckling simulation by FEM is presented in Section 2.2. The formulations of the linear buckling problems and numerical solutions of the FEM are stated in Section 2.3, Section 2.4, and Section 2.5. In order to verify Dickson's buckling theory, we returned to the starting point, using simple models to investigate the existence of the buckling phenomenon. We used three types of simple plate model having different geometrical properties to confirm the range of the geometrical parameters in which this buckling occurs. The details of the three simple models are introduced in Section 2.6. The simulation results of these three simple models are described in Section 2.7. These results also support Dickson's buckling hypothesis that a flattening or reversal of normal thoracic kyphosis at the apex of the curvature of the spine causes the buckling phenomenon.

2.1 Buckling hypothesis

Intensive researches for the pathogenesis of idiopathic scoliosis is ongoing throughout the world, and many possible causal factors and

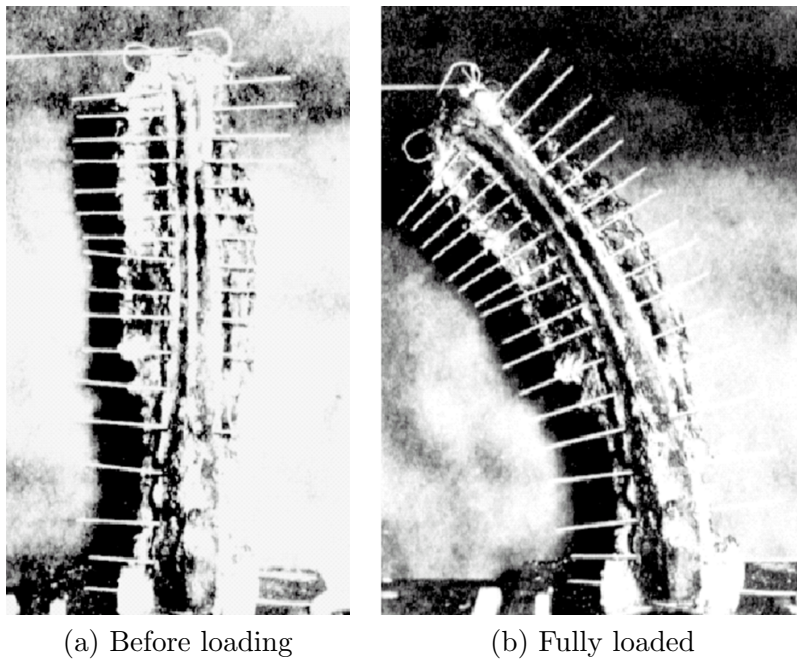


Figure 2.1: Lucas horizontal lateral loading test [5]

theories have been evaluated. We reviewed lots of literature about the hypothesis on the etiology of idiopathic scoliosis, and more attention have been paid to the buckling hypothesis.

2.1.1 Lucas's experiment

Lucas and Bresler [5] used ligamentous adult spine from the dead bodies to investigate the relationship between spinal stability and the cause of scoliosis. They assumed the spine as an elastic rod and calculated the critical load to make the spine buckled by Euler equation. With a weight-pulley system, the spines were put increasing horizontal lateral loading until buckling occurred, as shown in the Figure 2.1. They found applying a vertical load near the value of 20 kN at the top of the spine could make the spine to be buckled.

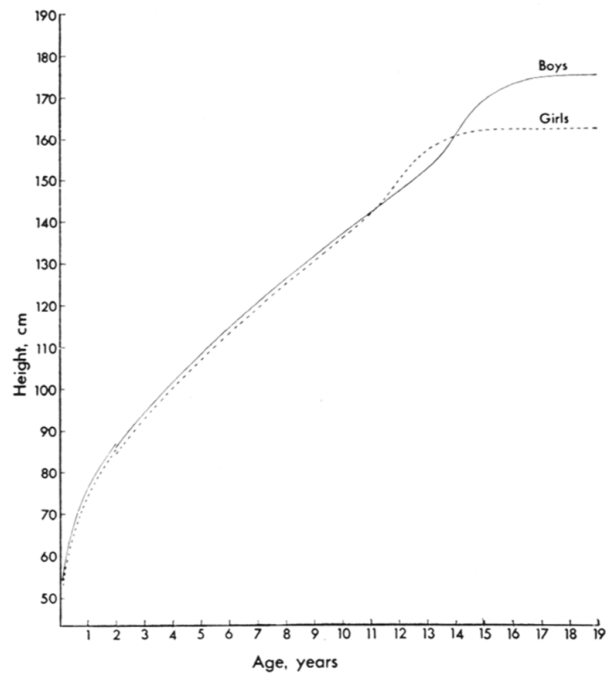
2.1.2 Dickson's experiment

Dickson et al. [56] presented an important observation of a flattening of the thoracic spine during a growth spurt. They found the thoracic kyphosis reduces in size from age of 8 to 14 year olds for the both girls and boys. Especially at the age of 12, the thoracic kyphosis at the apex of the curvature reach the minimum in size, and turn to be flattening or reversal. In generally, boys on average mature later than the girls. However, when the thoracic kyphosis is at its minimum for girls, they are also undergoing the peak adolescent growth. This reduction of thoracic kyphosis also raises the possibility of idiopathic scoliosis. Dickson identified the trigger of the rotational instability as a median plane asymmetry, that is, the flattening or reversal of normal thoracic kyphosis at the apex of the curvature, and they declared this instability to be a buckling phenomenon.

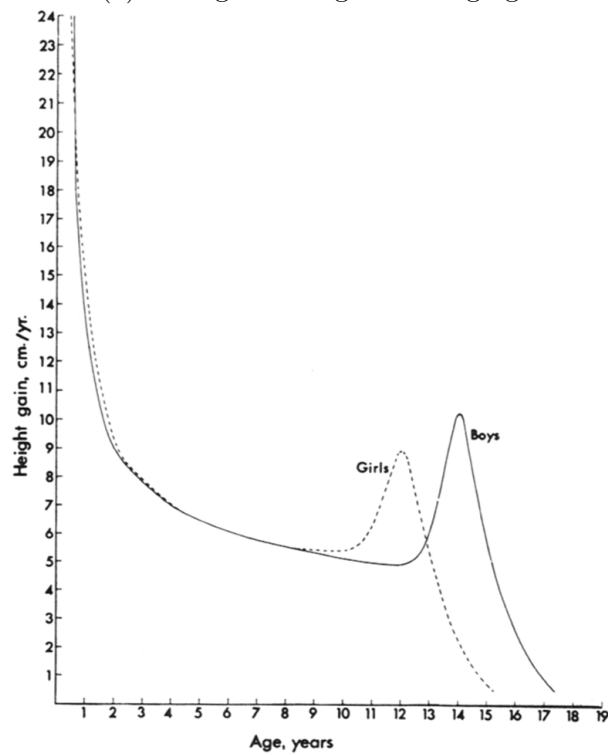
2.1.3 Previous research

Based on Dickson's buckling hypothesis, the previous research in our group used the linear buckling theory to analyze the buckling phenomenon induced by the growth of vertebral bodies using finite element models of the spine. By using a commercial program (MSC.Nastran 7.0), we obtained the fourth and sixth buckling modes, which are similar to the clinical single and double-major curves, respectively [64]. Figure 2.3 shows the result of the fourth buckling mode induced by the growth of vertebral bodies from T4 to T10.

However, previous results from a program based on nonlinear buckling theory indicated no clear buckling modes that similar to the clinical modes [10]. After this investigation, the linear buckling modes using another commercial program were reanalyzed, and no buckling phenomena was identified as well. This led us to wonder whether the buckling phenomenon actually existed or not. Thus, we used three types of simple plate model having different properties to confirm the existence of the buckling phenomenon and we then clarified the range in which the buckling phenomena occur. The reason why we use the simple plate models is to show that the buckling mechanism induced by the growth of vertebral bodies could be confirmed clearly even using different softwares.



(a) Changes in height with aging



(b) Changes in height increase rate with aging

Figure 2.2: Changes in height with aging for adolescents [6]

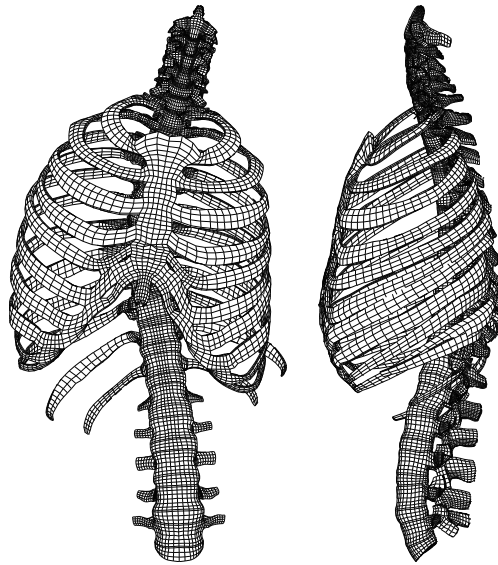


Figure 2.3: Fourth buckling mode from previous research [7]

2.2 Buckling

2.2.1 Basics of buckling theory

Buckling is a treacherous instability phenomenon in nature and structural engineering. It can be described as a mathematical instability, leading to a failure mode. Buckling is caused by a bifurcation in the solution to the equations of static equilibrium.

Linear buckling is also called as eigenvalue buckling. The linear buckling analysis can predict the theoretical buckling strength of an ideal elastic structure. The goal of the linear buckling analysis could be used to determine the buckling load factor and the estimate the critical (bifurcation) load of the structure. Linear buckling analysis can not provide exact results and only used when designing or examining is needed.

There is another more accurate type of buckling analysis named nonlinear buckling analysis which is often used to predict instability for structural engineering. For more details about nonlinear buckling analysis, will be discussed in Chapter 3.

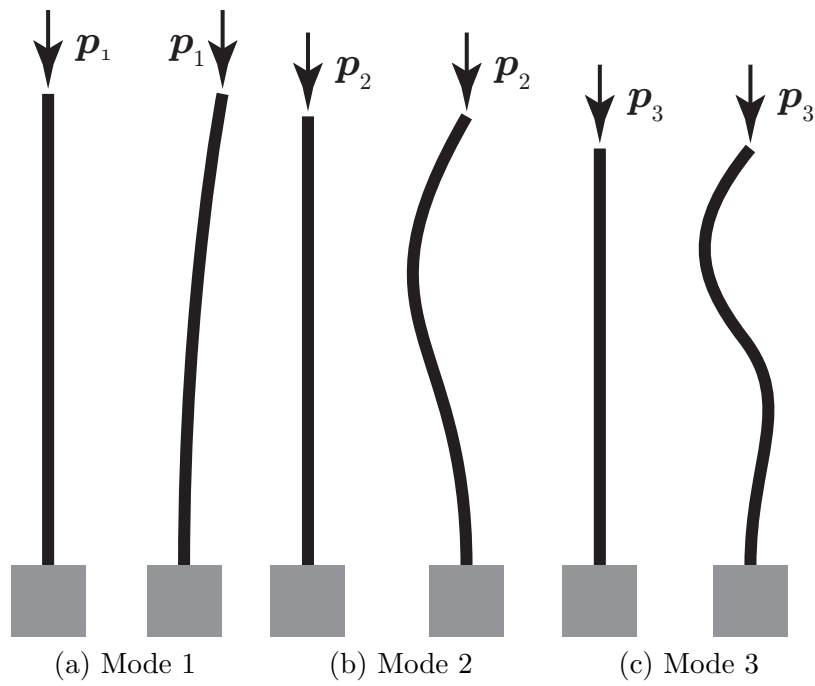


Figure 2.4: Euler buckling

2.2.2 Buckling analysis through FEM

In this chapter, two kinds of finite element software packages, Abaqus 6.12 Edition (Abaqus, Inc.) and RADIOSS 11.0 (Altair Engineering, Inc.) are used to examine the buckling hypothesis.

Abaqus 6.12 Edition (Abaqus, Inc.) offers two eigenvalue extraction methods for linear buckling analysis [65]. They are the Lanczos method and the Subspace iteration method. The Lanczos method can be finished faster than Subspace method when a large number of eigenmodes are inquired. However, the Subspace method might be faster when less than 20 eigenmodes are required. Because only a few of the lowest eigenvalues are required for buckling analysis of clinical idiopathic scoliosis, Lanczos method is used in this study.

For the RADIOSS 11.0 (Altair Engineering, Inc.) , there is only Lanczos method can be used for linear buckling analysis [66]. The difference of the results from the two softwares is shown in Section 2.8.

2.3 Growth deformation problem

Firstly, a review for the theory of buckling induced by the generation of non-elastic bulk strain is present as following. In the present research, the symbol \mathbb{R} is used as the set of real numbers [10]. We denote a three dimensional vector as $\mathbf{x} = (x_i)_i \in \mathbb{R}^3$, and a tensor as $\mathbf{E} = (\epsilon_{ij})_{ij} \in \mathbb{R}^{3 \times 3}$. A function f having value of \mathbb{R} defined on \mathbb{R}^3 is denoted as $f : \mathbb{R}^3 \rightarrow \mathbb{R}$, and $f(\mathbf{x}) : \mathbb{R}^3 \ni \mathbf{x} \mapsto f \in \mathbb{R}$.

Let Ω be a three-dimensional domain of a spine, from the sacrum to the second cervical vertebra. We assume that the spine is an elastic body fixed on a boundary Γ_D , which corresponds to the boundary of the sacrum. Moreover, let $(0, t_T)$ be a time domain with some terminal time t_T . The non-elastic bulk strain is defined as follows. Let $p : \Omega \rightarrow \mathbb{R}$ be a function for the growth pattern, and let $\lambda : (0, t_T) \rightarrow \mathbb{R}$ be a function for the magnitude of the growth over time. In previous studies [64] [10], the function p took the value of 1 at the epiphyseal growth plates and 0 elsewhere. Using $p(\mathbf{x})$ and $\lambda(t)$, we assume that

the non-elastic bulk strain denoting the growth is given by

$$\mathbf{E}_G(t, \mathbf{x}) = \lambda(t) p(\mathbf{x}) \mathbf{I}, \quad (2.3.1)$$

where \mathbf{I} is the identity matrix of the third order. Moreover, we assume that $\lambda(t)$ is a monotonically increasing function of t , and we denote $\mathbf{E}_G(t, \mathbf{x})$ by $\mathbf{E}_G(\lambda)$.

The buckling theory is obtained from the large-deformation theory. Let us briefly review the large-deformation theory. Consider a point $\mathbf{x} = (x_i)_i \in \Omega$ that moves to $\mathbf{y}(t, \mathbf{x}) = (\mathbf{i} + \mathbf{u})(t, \mathbf{x}) = \mathbf{x} + \mathbf{u}(t, \mathbf{x}) : (0, t_T) \times \Omega \ni (t, \mathbf{x}) \mapsto \mathbf{y} \in \mathbb{R}^3$, where \mathbf{i} denotes the identity mapping. We define the deformation gradient tensor as

$$\mathbf{F}(\mathbf{u}) = \left(\frac{\partial y_i}{\partial x_j} \right)_{ij} = \mathbf{I} + \left(\frac{\partial u_i}{\partial x_j} \right)_{ij}. \quad (2.3.2)$$

Using $\mathbf{F}(\mathbf{u})$, the Green-Lagrange strain is defined as

$$\begin{aligned} \mathbf{E}(\mathbf{u}) &= (\epsilon_{ij}(\mathbf{u}))_{ij} \\ &= \frac{1}{2} (\mathbf{F}(\mathbf{u}) \mathbf{F}^T(\mathbf{u}) - \mathbf{I}) = \mathbf{E}_L(\mathbf{u}) + \frac{1}{2} \mathbf{E}_B(\mathbf{u}, \mathbf{u}), \end{aligned} \quad (2.3.3)$$

where

$$\mathbf{E}_L(\mathbf{u}) = \frac{1}{2} \left(\frac{\partial u_i}{\partial x_j} + \frac{\partial u_j}{\partial x_i} \right)_{ij}, \quad (2.3.4)$$

$$\mathbf{E}_B(\mathbf{u}, \mathbf{v}) = \frac{1}{2} \left(\sum_{k \in \{1,2,3\}} \frac{\partial u_k}{\partial x_i} \frac{\partial v_k}{\partial x_j} \right)_{ij} \quad (2.3.5)$$

denote the linear stain and the bilinear part of the Green-Lagrange strain, respectively. Moreover, denoting the stiffness by $\mathbf{C} : \Omega \rightarrow \mathbb{R}^{3 \times 3 \times 3 \times 3}$, the second Piola-Kirchhoff stress and the linear stress are defined, respectively, as

$$\begin{aligned} \mathbf{S}(\mathbf{u}, \lambda) &= (\sigma_{ij}(\mathbf{u}, \lambda))_{ij} = \mathbf{C}(\mathbf{E}(\mathbf{u}) - \mathbf{E}_G(\lambda)) \\ &= \left(\sum_{(k,l) \in \{1,2,3\}^2} c_{ijkl} \epsilon_{kl}(\mathbf{u}) \right)_{ij}, \end{aligned} \quad (2.3.6)$$

$$\mathbf{S}_L(\mathbf{u}, \lambda) = \mathbf{C}(\mathbf{E}_L(\mathbf{u}) - \mathbf{E}_G(\lambda)). \quad (2.3.7)$$

Using $\mathbf{E}(\mathbf{u})$ and $\mathbf{S}(\mathbf{u}, \lambda)$, the potential energy induced by $\mathbf{E}_G(\lambda)$ without any external force is defined by

$$\pi(\mathbf{u}) = \frac{1}{2}a(\mathbf{S}(\mathbf{u}, \lambda), \mathbf{E}(\mathbf{u}) - \mathbf{E}_G(\lambda)) \quad (2.3.8)$$

for $\mathbf{u} \in U$, where $a(\mathbf{S}, \mathbf{E})$ is a bilinear form with respect to \mathbf{S} and \mathbf{E} defined as

$$a(\mathbf{S}, \mathbf{E}) = \int_{\Omega} \mathbf{S} \cdot \mathbf{E} \, dx = \int_{\Omega} \sum_{(i,j) \in \{1,2,3\}^2} \sigma_{ij} \epsilon_{ij} \, dx, \quad (2.3.9)$$

and U is the set of displacements satisfying $\mathbf{u} = \mathbf{0}_{\mathbb{R}^3}$ on Γ_D . Although we are discussing a nonlinear problem, the bilinearity of $a(\mathbf{S}, \mathbf{E})$ with respect to \mathbf{S} and \mathbf{E} is maintained. From the principle of the minimum potential energy, the displacement $\mathbf{u} \in U$ with respect to the growth strain $\mathbf{E}_G(\lambda)$ is determined by

$$\pi'(\mathbf{u})[\mathbf{v}] = a(\mathbf{C}(\mathbf{E}(\mathbf{u}) - \mathbf{E}_G(\lambda)), \mathbf{E}'(\mathbf{u})[\mathbf{v}]) = 0 \quad (2.3.10)$$

for all $\mathbf{v} \in U$, where $\pi'(\mathbf{u})[\mathbf{v}]$ denotes the derivative of $\pi(\mathbf{u})$ with respect to an arbitrary variation \mathbf{v} of \mathbf{u} , and

$$\begin{aligned} \mathbf{E}'(\mathbf{u})[\mathbf{v}] &= \frac{1}{2} \left\{ (\mathbf{F}'(\mathbf{u})[\mathbf{v}])^T \mathbf{F}(\mathbf{u}) + (\mathbf{F}(\mathbf{u}))^T \mathbf{F}'(\mathbf{u})[\mathbf{v}] \right\} \\ &= \mathbf{E}_L(\mathbf{v}) + \mathbf{E}_B(\mathbf{u}, \mathbf{v}), \end{aligned} \quad (2.3.11)$$

$$\mathbf{F}'(\mathbf{u})[\mathbf{v}] = \left(\frac{\partial v_i}{\partial x_j} \right)_{ij}. \quad (2.3.12)$$

Moreover, if the terms of \mathbf{E}_B can be neglected by assuming that \mathbf{u} and \mathbf{v} are small, we have the weak form of the linear deformation problem as

$$a(\mathbf{C}\mathbf{E}_L(\mathbf{u}), \mathbf{E}_L(\mathbf{v})) = a(\mathbf{C}\mathbf{E}_G(\lambda), \mathbf{E}_L(\mathbf{v})) \quad (2.3.13)$$

for all $\mathbf{v} \in U$.

2.4 Buckling problem

Buckling is known as a bifurcation phenomenon in the solution to the equations of static equilibrium [67] [68]. Under the equilibrium condition of $\pi'(\mathbf{u})[\mathbf{v}] = 0$ for all $\mathbf{v} \in U$, a buckling phenomenon occurs when there exists $\mathbf{v}_2 \in U$ such that

$$\begin{aligned} \pi''(\mathbf{u})[\mathbf{v}_1, \mathbf{v}_2] &= a(\mathbf{S}'(\mathbf{u}, \lambda)[\mathbf{v}_2], \mathbf{E}'(\mathbf{u})[\mathbf{v}_1]) + a(\mathbf{S}(\mathbf{u}, \lambda), \mathbf{E}''(\mathbf{u})[\mathbf{v}_1, \mathbf{v}_2]) \\ &= 0 \end{aligned} \quad (2.4.1)$$

for all $\mathbf{v}_1 \in U$, where

$$\mathbf{S}'(\mathbf{u}, \lambda)[\mathbf{v}_2] = \mathbf{C}\mathbf{E}'(\mathbf{u})[\mathbf{v}_2], \quad (2.4.2)$$

$$\mathbf{E}'(\mathbf{u})[\mathbf{v}_1] = \mathbf{E}_L(\mathbf{v}_1) + \mathbf{E}_B(\mathbf{v}_1, \mathbf{u}), \quad (2.4.3)$$

$$\mathbf{E}''(\mathbf{u})[\mathbf{v}_1, \mathbf{v}_2] = \mathbf{E}_B(\mathbf{v}_1, \mathbf{v}_2). \quad (2.4.4)$$

In Eq. (2.4.1), \mathbf{u} and \mathbf{v}_2 are called, respectively, the critical displacement and the eigenmode of the buckling phenomenon. Substituting in Eq. (2.4.2), Eq. (2.4.3), and Eq. (2.4.4), Eq. (2.4.1) can be rewritten as

$$\begin{aligned} \pi''(\mathbf{u})[\mathbf{v}_1, \mathbf{v}_2] &= a(\mathbf{C}(\mathbf{E}_L(\mathbf{v}_2) + \mathbf{E}_B(\mathbf{v}_2, \mathbf{u})), \mathbf{E}_L(\mathbf{v}_1) + \mathbf{E}_B(\mathbf{u}, \mathbf{v}_1)) \\ &\quad + a(\mathbf{S}(\mathbf{u}, \lambda), \mathbf{E}_B(\mathbf{v}_1, \mathbf{v}_2)) \\ &= 0. \end{aligned} \quad (2.4.5)$$

Here, let \mathbf{u}_0 , a solution of the equilibrium condition of $\pi'(\mathbf{u}_0)[\mathbf{v}] = 0$ for all $\mathbf{v} \in U$ at a given $\lambda_0 = \lambda(t_0)$, be the initial growth rate, and let $\mathbf{u} = \zeta\mathbf{u}_0$ and \mathbf{v}_2 be the solution of Eq. (2.4.5) for all $\mathbf{v}_1 \in U$. In this case, \mathbf{u}_0 and ζ are called, respectively, the initial displacement and the buckling coefficient. Using the above definitions, Eq. (2.4.5) can be rewritten in the neighborhood of $\zeta = 1$ as

$$\begin{aligned} a(\mathbf{C}\mathbf{E}_L(\mathbf{v}_2), \mathbf{E}_L(\mathbf{v}_1)) &= -\zeta \{ a(\mathbf{S}(\mathbf{u}_0, \lambda_0), \mathbf{E}_B(\mathbf{v}_2, \mathbf{v}_1)) + a(\mathbf{C}\mathbf{E}_L(\mathbf{v}_2), \mathbf{E}_B(\mathbf{u}_0, \mathbf{v}_1)) \\ &\quad + a(\mathbf{C}\mathbf{E}_B(\mathbf{v}_2, \mathbf{u}_0), \mathbf{E}_L(\mathbf{v}_1)) \}. \end{aligned} \quad (2.4.6)$$

Equation (2.4.6) for all $\mathbf{v}_1 \in U$ is called the weak form of the nonlinear buckling problem.

Moreover, if we can neglect the terms of \mathbf{E}_B without $\mathbf{E}_B(\mathbf{v}_2, \mathbf{v}_1)$ on the right-hand side of Eq. (2.4.6), we have the weak form of the linear buckling problem as

$$a(\mathbf{C}\mathbf{E}_L(\mathbf{v}_2), \mathbf{E}_L(\mathbf{v}_1)) = -\zeta a(\mathbf{S}_L(\mathbf{u}_0, \lambda_0), \mathbf{E}_B(\mathbf{v}_2, \mathbf{v}_1)) \quad (2.4.7)$$

for all $\mathbf{v}_1 \in U$. In this weak form, we can use an arbitrary value for λ_0 because the linearity of

$$a(\mathbf{S}_L(\mathbf{u}, \lambda), \mathbf{E}_B(\mathbf{v}_2, \mathbf{v}_1)) = \zeta a(\mathbf{S}_L(\mathbf{u}_0, \lambda_0), \mathbf{E}_B(\mathbf{v}_2, \mathbf{v}_1)) \quad (2.4.8)$$

holds for Eq. (2.4.7).

2.5 Finite element analysis

Using the weak form of the linear buckling problem, an eigenvalue problem for the buckling phenomenon can be obtained by using FEM. Following the standard procedure, we define approximate functions for \mathbf{u}_0 , \mathbf{v}_1 , and \mathbf{v}_2 as

$$\begin{aligned} \mathbf{u}_{0h}(\bar{\mathbf{u}}) &= \sum_{i \in \mathcal{N}_D} \begin{pmatrix} \bar{u}_{0i1} \phi_i \\ \bar{u}_{0i2} \phi_i \\ \bar{u}_{0i3} \phi_i \end{pmatrix} + \sum_{i \in \mathcal{N}_N} \begin{pmatrix} \bar{u}_{0i1} \phi_i \\ \bar{u}_{0i2} \phi_i \\ \bar{u}_{0i3} \phi_i \end{pmatrix} \\ &= \begin{pmatrix} \bar{\mathbf{u}}_{0D} \\ \bar{\mathbf{u}}_{0N} \end{pmatrix}^T \begin{pmatrix} \phi_D \\ \phi_N \end{pmatrix} = \bar{\mathbf{u}}_0^T \phi, \end{aligned} \quad (2.5.1)$$

$$\mathbf{v}_{1h}(\bar{\mathbf{v}}_1) = \bar{\mathbf{v}}_1^T \phi, \quad (2.5.2)$$

$$\mathbf{v}_{2h}(\bar{\mathbf{v}}_2) = \bar{\mathbf{v}}_2^T \phi, \quad (2.5.3)$$

respectively, where \mathcal{N} denotes the set of all node numbers, $\mathcal{N}_D \subset \mathcal{N}$ denotes the set of node numbers on Γ_D , and \mathcal{N}_N denotes $\mathcal{N} \setminus \mathcal{N}_D$. Here, we call $\bar{\mathbf{u}}_0$, $\bar{\mathbf{v}}_1$, and $\bar{\mathbf{v}}_2$ the node vectors, and ϕ the basis functions.

The finite element equation of the growth deformation problem for λ_0 can be obtained as follows. Using Eq. (2.5.1) and Eq. (2.5.2) for \mathbf{u} and \mathbf{v} , respectively, Eq. (2.3.13) can be rewritten as

$$\bar{\mathbf{v}}_1^T (\bar{\mathbf{K}} \bar{\mathbf{u}}_0) = \bar{\mathbf{v}}_1^T \bar{\mathbf{b}}_0, \quad (2.5.4)$$

where $\bar{\mathbf{K}} = (\bar{k}_{ij})_{(i,j) \in \mathcal{N}^2}$ and $\bar{\mathbf{b}}_0 = (\bar{b}_{0i})_{i \in \mathcal{N}}$ consist of

$$\bar{k}_{ij} = a(\mathbf{S}_L(\bar{\phi}_i), \mathbf{E}_L(\bar{\phi}_j)), \quad (2.5.5)$$

$$\bar{b}_{0i} = a(\mathbf{C}\mathbf{E}_G(\lambda_0), \mathbf{E}_L(\bar{\phi}_i)), \quad (2.5.6)$$

where $\bar{\phi}_i$ is the three-dimensional function consisting of the basis vectors for node $i \in \mathcal{N}$. Substituting the Dirichlet condition on Γ_D , the approximate weak form of the linear growth deformation can be written as

$$\begin{pmatrix} \mathbf{0} \\ \bar{\mathbf{v}}_{1N} \end{pmatrix}^T \begin{pmatrix} \bar{\mathbf{K}}_{DD} & \bar{\mathbf{K}}_{DN} \\ \bar{\mathbf{K}}_{ND} & \bar{\mathbf{K}}_{NN} \end{pmatrix} \begin{pmatrix} \mathbf{0} \\ \bar{\mathbf{u}}_{0N} \end{pmatrix} = \begin{pmatrix} \bar{\mathbf{b}}_{0D} \\ \bar{\mathbf{b}}_{0N} \end{pmatrix} \quad (2.5.7)$$

for all $\bar{\mathbf{v}}_{1N}$. Rearranging Eq. (2.5.7), we have

$$\bar{\mathbf{K}}_{NN} \bar{\mathbf{u}}_{0N} = \bar{\mathbf{b}}_{0N}. \quad (2.5.8)$$

Since $\bar{\mathbf{K}}_{NN}$ is a real symmetric and positive-definite matrix, $\bar{\mathbf{u}}_{0N}$ can be computed.

For the linear buckling problem, using Eq. (2.5.1), Eq. (2.5.2), and Eq. (2.5.3) for \mathbf{u}_0 , \mathbf{v}_1 , and \mathbf{v}_2 , respectively, Eq. (2.4.7) can be rewritten as

$$\bar{\mathbf{v}}_1^T \bar{\mathbf{K}} \bar{\mathbf{v}}_2 = -\zeta \bar{\mathbf{v}}_1^T \bar{\mathbf{G}} \bar{\mathbf{u}}_0, \quad (2.5.9)$$

where $\bar{\mathbf{K}} = (\bar{k}_{ij})_{(i,j) \in \mathcal{N}^2}$ and $\bar{\mathbf{G}} = (\bar{g}_{ij})_{(i,j) \in \mathcal{N}^2}$ consist of Eq. (2.5.5) and

$$\bar{g}_{ij}(\mathbf{u}_{0h}) = a(\mathbf{S}_L(\mathbf{u}_{0h}), \mathbf{E}_B(\bar{\phi}_i, \bar{\phi}_j)), \quad (2.5.10)$$

respectively. Substituting the Dirichlet condition on Γ_D , the approximate weak form of the linear buckling problem can be written as

$$\begin{pmatrix} \mathbf{0} \\ \bar{\mathbf{v}}_{1N} \end{pmatrix}^T \left(\begin{pmatrix} \bar{\mathbf{K}}_{DD} & \bar{\mathbf{K}}_{DN} \\ \bar{\mathbf{K}}_{ND} & \bar{\mathbf{K}}_{NN} \end{pmatrix} + \zeta \begin{pmatrix} \bar{\mathbf{G}}_{DD} & \bar{\mathbf{G}}_{DN} \\ \bar{\mathbf{G}}_{ND} & \bar{\mathbf{G}}_{NN} \end{pmatrix} \right) \begin{pmatrix} \mathbf{0} \\ \bar{\mathbf{v}}_{2N} \end{pmatrix} = \mathbf{0} \quad (2.5.11)$$

for all $\bar{\mathbf{v}}_{1N}$. Rearranging Eq. (2.5.11), we have

$$\bar{\mathbf{K}}_{NN} \bar{\mathbf{v}}_{2N} = -\zeta \bar{\mathbf{G}}_{NN} \bar{\mathbf{v}}_{2N}. \quad (2.5.12)$$

Since $\bar{\mathbf{K}}_{NN}$ and $\bar{\mathbf{G}}_{NN}$ are real symmetric matrices, Eq. (2.5.12) becomes a real eigenvalue problem for the eigenvalue $-\zeta$ and eigenvector $\bar{\mathbf{v}}_{2N}$.

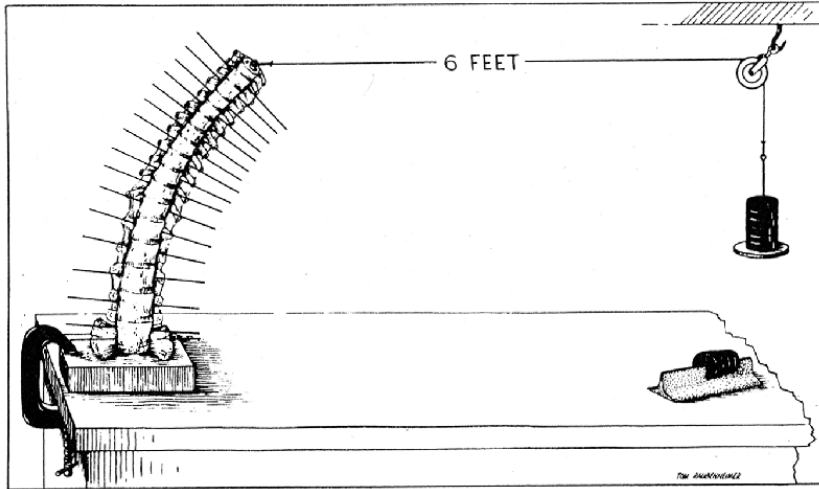


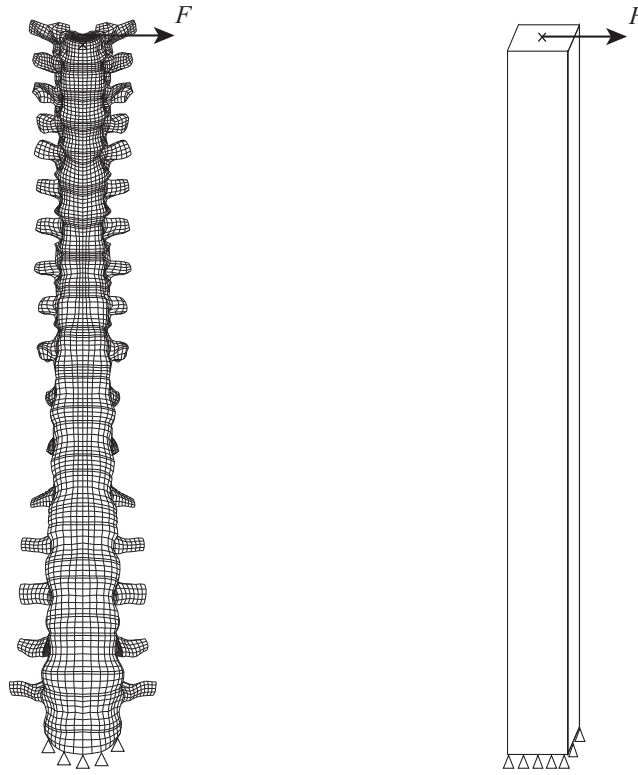
Figure 2.5: Lucas's horizontal lateral loading test method [5]

2.6 Finite element Models

Based on the formulations of the buckling problem and numerical solutions, we analyzed the linear buckling phenomena using the results of growth deformations predicted by simple spine models. The details of each model are described as below.

2.6.1 Young's modulus

Firstly, in order to obtain the average Young's modulus of the spine, we repeated the Lucas's horizontal lateral loading test though FEM [5]. The schematic drawing of Lucas's horizontal lateral loading test is shown in Figure 2.5. The simple plate model we used to repeat the Lucas's test is shown in Figure 2.6 (b), which has the same boundary condition as Figure 2.6 (a). The bottom of the simple plate model was fixed, and a horizontal lateral loading was put at the top of the plate model. With the data from the Lucas's horizontal lateral loading test, the Young's modulus can be calculated by the Euler's buckling Load formula. As result after calculation, the Young's modulus for all the



(a)Boundary condition of Lucas's test (b)Boundary condition of plate

Figure 2.6: The plate model in order to repeat Lucas's loading test [5]

simple plate models is assumed to be 8 [MPa].

2.6.2 Model 1

Model 1 is just a straight square column, has the height $h = 500$ mm and depth $d = 50$ mm, which are appropriate geometrical dimensions for an actual human spine, as shown in Figure 2.7. The front width w_F , back width w_B , and depth of the growth domain g were chosen as the variables. After calculation in Section 2.6.1, the Young's modulus was assumed to be 8 [MPa], and Poisson's ratio was assumed to be 0.3. About 6,500 second-order tetrahedral elements were used for this model.

In the living human being subject, the top of the spine is free and the sacrum of the spine is fixed. For the boundary conditions of the simple plate models, we also assigned a fixed boundary Γ_D at the bottom of all the models, which was at the base of the deformation. The growth pattern p was assumed to take the value of 1 in the areas shown in red in Figure 2.7, and the value 0 elsewhere. The value of 0.1 was used for the initial growth rate λ_0 . With changing the design variables, front width w_F and back width w_B , we investigated the difficulty levels of getting buckling phenomenon for Model 1 according to different front width w_F and back width w_B . Figure 2.8 shows the results of the numbers of the buckling modes in each w_F - w_B space for Model 1, when growth domain $g = 10$ mm.

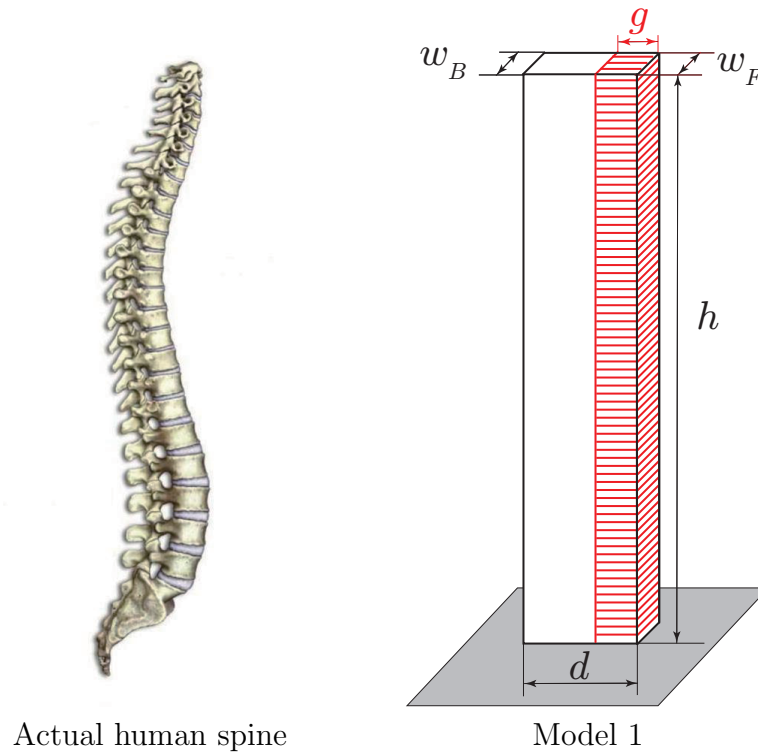
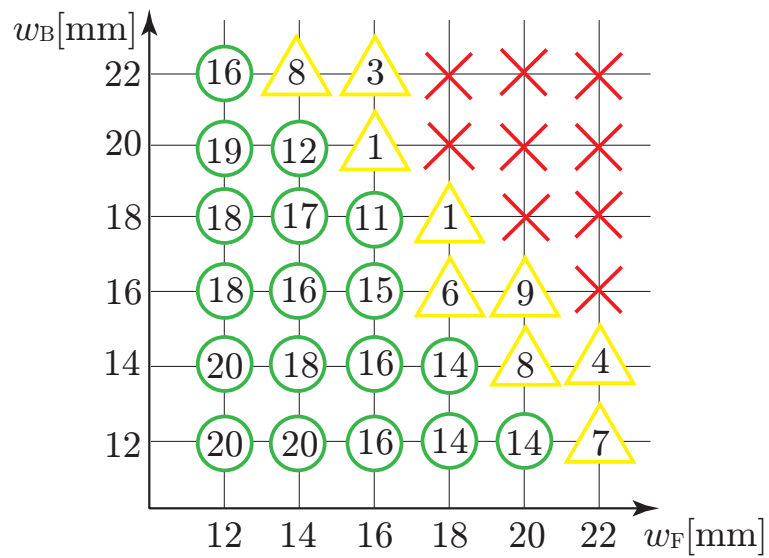


Figure 2.7: Model 1

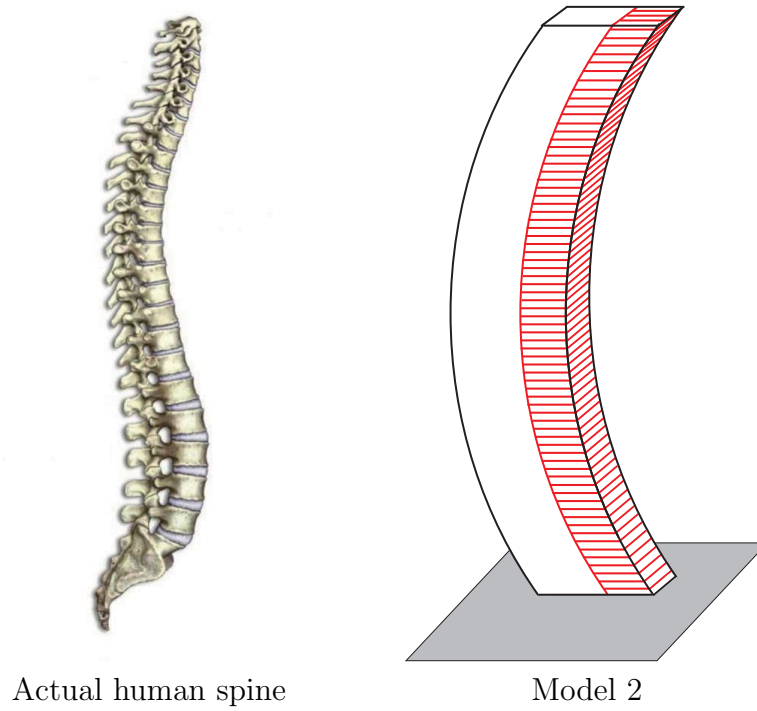
Figure 2.8: Maps of the existence of buckling modes when $g = 10$ mm for Model 1

2.6.3 Model 2

Model 2 has a physiological curvature of 45° as the actual human spine, as shown in Figure 2.9. The height h is 500 mm, and the depth d is 50 mm, as same as Model 1. The front width w_F , back width w_B , and depth of the growth domain g were chosen as the variables. The front width w_F and back width w_B are the variables in order to judge the difficulty degree for Model 2 to get buckling phenomenon with different front width w_F and back width w_B . Figure 2.10 shows the results of the numbers of the buckling modes in each w_F - w_B space for Model 2, when growth domain $g = 10$ mm.

2.6.4 Model 3

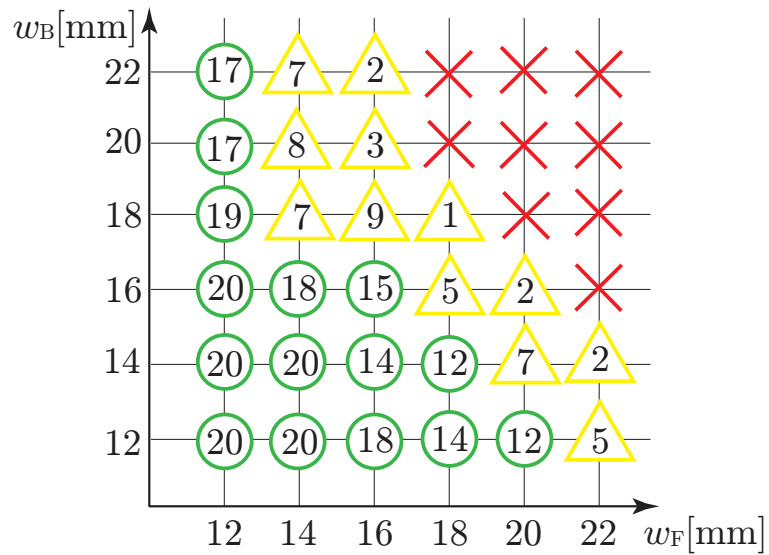
Model 3 has small square holes ($20\text{mm} \times 20\text{mm}$) in the rear part which is similar as the foramina of the actual human spine, with height $h = 500$ mm and depth $d = 50$ mm, as shown in Figure 2.11. The front width w_F , back width w_B , and depth of the growth domain g were chosen as the variables. We also changed the front width w_F and back width w_B in order to investigate the difficulty levels for Model 3 to get buckling phenomenon at different front width w_F and back width w_B . Figure 2.12 shows the results of the numbers of the buckling modes in each w_F - w_B space for Model 3, when growth domain $g = 10$ mm.



Actual human spine

Model 2

Figure 2.9: Model 2

Figure 2.10: Maps of the existence of buckling modes when $g = 10$ mm for Model 2

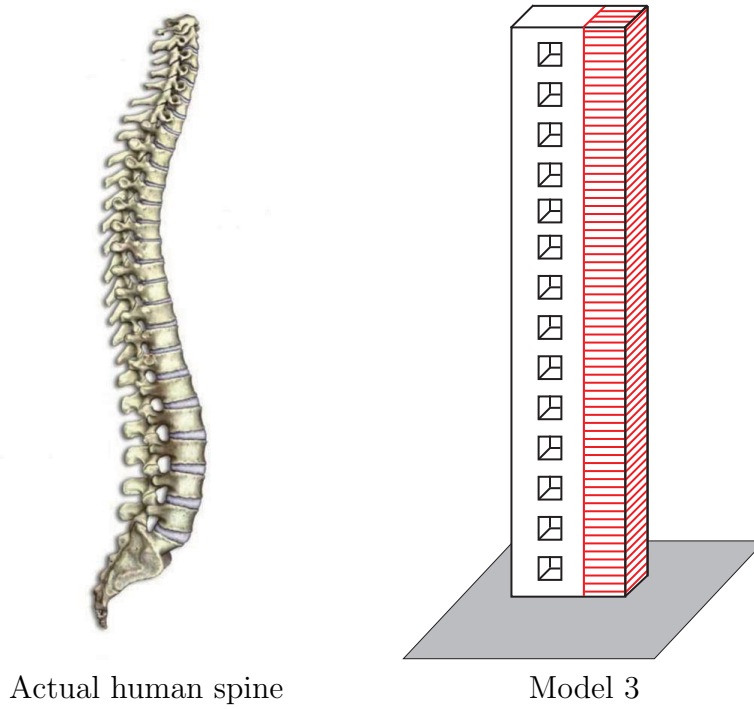


Figure 2.11: Model 3

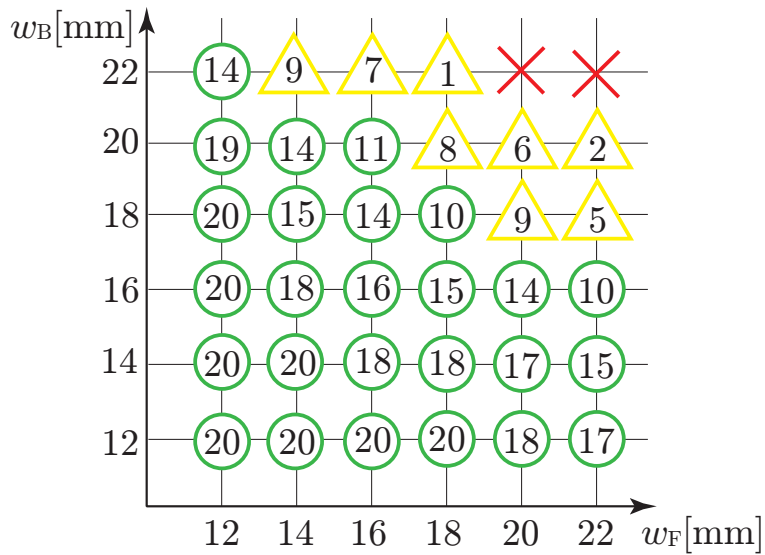


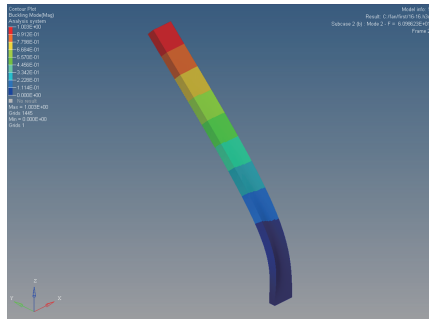
Figure 2.12: Maps of the existence of buckling modes when $g = 10$ mm for Model 3

2.7 Results

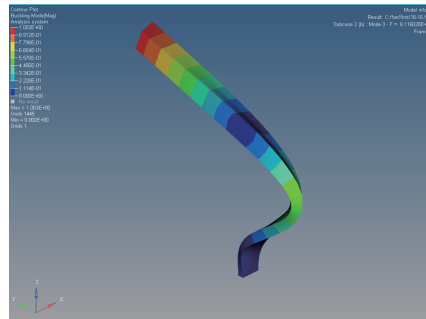
Figure 2.8, Figure 2.10, and Figure 2.12 show the results of the numbers of the buckling modes in w_F - w_B space for Model 1, Model 2, Model 3, respectively, when $g = 10$ mm. The number of buckling modes is used as an index of the reliability of existence of the buckling phenomena. If the buckling phenomena exist stably, based on the similarity with the Euler buckling theory, many buckling modes could occur through FEM. In order to distinguish the boundaries, the numbers of buckling modes are shown different marks with different colors in Figure 2.8, Figure 2.10, and Figure 2.12. The green circles indicate more than ten buckling modes were obtained in the domain with this w_F - w_B space. The yellow triangles indicate less than ten buckling modes occurred in the domain with this w_F - w_B space. Besides, the red crosses mean that there are no buckling phenomenon for this combination of (w_F, w_B) .

From the results of existence maps, we can see that the buckling modes are stable when $(w_F, w_B) = (16 \text{ mm}, 16 \text{ mm})$. Figure 2.13 shows the shape of the buckling modes for Model 1 at $(w_F, w_B) = (16 \text{ mm}, 16 \text{ mm})$ by using RADIOSS 11.0 (Altair Engineering, Inc.). The results obtained by the Abaqus 6.12 Edition (Abaqus, Inc.) are shown in the Figure 2.14. From these figures, the results obtained from these two commercial software packages were almost the same.

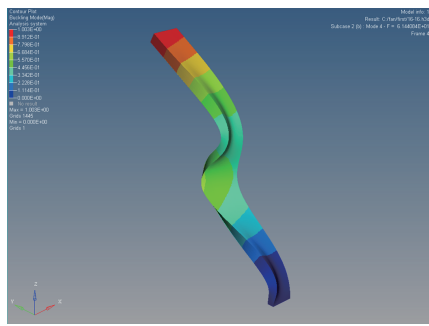
We also investigated how buckling phenomenon occurs with changing the variable, growth depth g . The buckling coefficient ζ is used to describe difficulty levels for the models to get buckled according to different growth depth g . The Figure 2.15 shows the dependency of the growth depth g on the buckling coefficient ζ for Models 1 and 2 at $(w_F, w_B) = (16 \text{ mm}, 16 \text{ mm})$ when $g = 10$ mm.



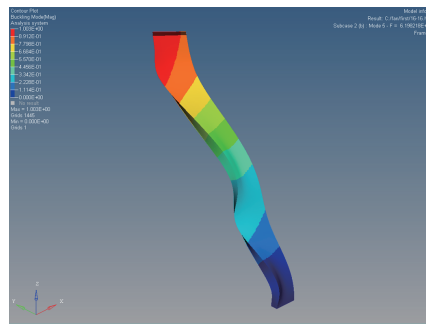
(a) 1st mode



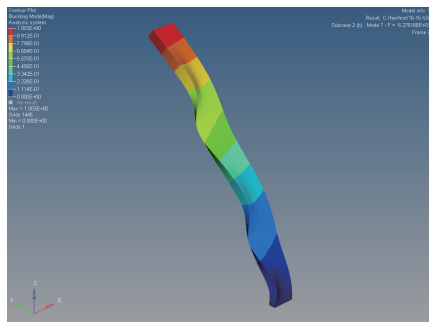
(b) 2nd mode



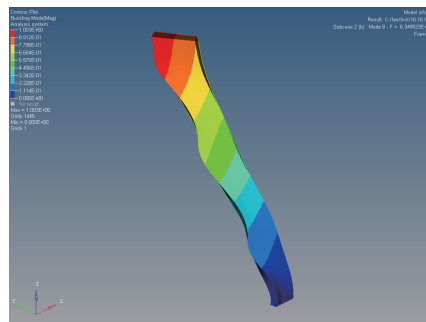
(a) 3rd mode



(b) 4th mode



(a) 5th mode



(b) 6th mode

Figure 2.13: Shapes of the buckling modes for Model 1 at $(w_F, w_B) = (16 \text{ mm}, 16 \text{ mm})$ when $g = 10 \text{ mm}$ via RADIOSS 11.0 (Altair Engineering, Inc.)

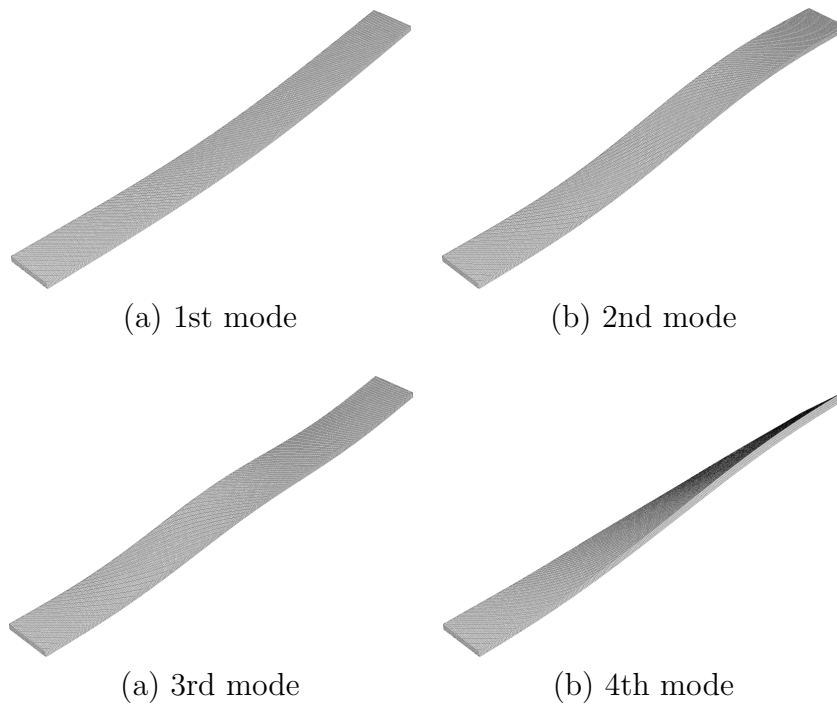


Figure 2.14: Shapes of the buckling modes for Model 1 at $(w_F, w_B) = (16 \text{ mm}, 16 \text{ mm})$ when $g = 10 \text{ mm}$ via Abaqus 6.12 Edition (Abaqus, Inc.)

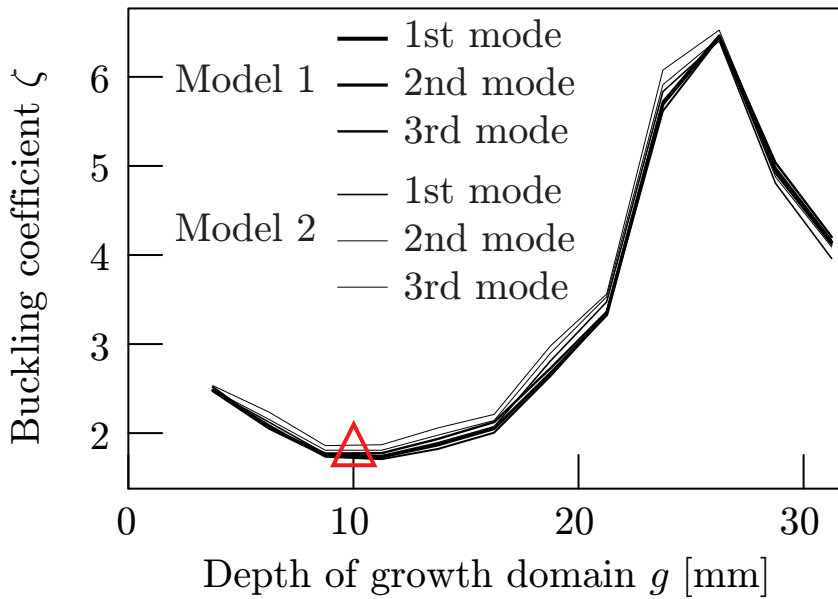


Figure 2.15: Dependency of depth g of growth domain on the buckling coefficient ζ for Model 1 and Model 2 at $(w_F, w_B) = (16 \text{ mm}, 16 \text{ mm})$

2.8 Discussion

From the results of existence maps for buckling modes of Model 1, Model 2 and Model 3, we can confirm that there are boundaries between the domain in which buckling occurs and the domain in which it does not. Moreover, the area in which buckling occurs for Model 1 is larger than Model 2, and this result supports Dickson's buckling hypothesis, namely, that flattening of spine increases the possibility for buckling to occur. The area in which buckling occurs for Model 3 is larger than Model 1, investigated that when the structure of a spine has holes in the rear part, buckling can be taken place easier.

From the results shown in Figure 2.15, for all the models, buckling is most likely to occur when the growth depth g is around 10 mm. When the growth depth is small, the total amount of growth will be also small in the initial growth deformation. Increasing of growth depth from 0 mm to some amount brings the increase of the total amount of growth. Then, it is considered that the buckling coefficient decreases in the range of small growth depth. On the other hand,

in the range of large growth depth, since the growth deformation becomes dominant, it is considered that the likelihood of the buckling phenomena decreases. From these considerations, the minimum value of the growth depth exists when buckling is at the best state to occur. In the case of the three models we used in this study, the minimum value of the growth depth was around 10 mm. This result supports the previous work [69], in which we showed that the growth of the frontal parts of the vertebral bodies generates the best state for buckling phenomena to occur.

2.9 Conclusion

In this Chapter, we used linear buckling theory to investigate the buckling induced by the growth of vertebral bodies; to do so, we used two commercial software packages via three simplified spine models.

From the results, we confirmed the existence of the buckling phenomena, and we clarified the range of geometrical parameters in which the buckling occurs. By the comparison of the range between the three models, we can conclude the following results.

(1) The growth of the frontal parts of spine in depth around 10 mm from the frontal plain causes the best state for buckling phenomena to occur.

(2) The model with physiological curvature enlarges the buckling area than the straight model.

(3) The structure having holes in the rear part also enlarges the buckling area.

These results support the buckling hypothesis of Dickson that a flattening or reversal of normal thoracic kyphosis at the apex of the curvature of the spine causes the buckling phenomenon. Analyses using spine models to consider geometrical nonlinearity will be described in next chapter.

Chapter 3

Nonlinear post-buckling analysis for plate model

In this chapter, we investigated the nonlinear post-buckling analysis by the simple plate model. Firstly, the basic of nonlinear post-buckling analysis is introduced in Section 3.1. In this study, the Arc-length Method is used to complete nonlinear post-buckling analysis, which is then compared with the classical Newton-Raphson method in Section 3.2. Section 3.3 states the effect of geometric imperfection of the finite element model which is necessary for post-buckling analysis. The procedure of nonlinear post-buckling analysis through Abaqus/Standard is introduced in Section 3.4. Section 3.5 reviews the non-elastic strain and nonlinear buckling analysis by FEM. The detail of the simple plate model is described in Section 3.6. The result for nonlinear post-buckling analysis for the simple plate model is presented in the Section 3.7. Lastly, the discussion and conclusion of the nonlinear post-buckling analysis is summarized in Section 3.8 and Section 3.9.

3.1 Nonlinear buckling analysis

Linear buckling analysis can not provide exact simulation of buckling phenomenon, and can only be used when designing and examining process is needed. Especially, it is generally used to estimate the critical buckling loads of the structure.

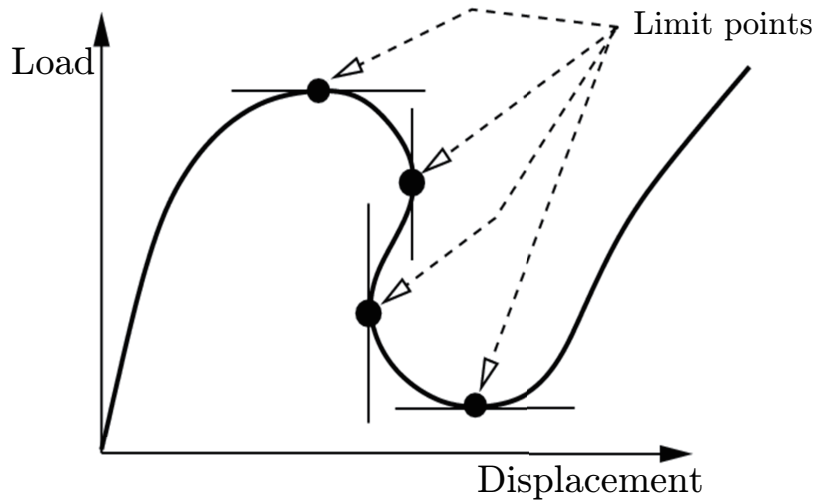


Figure 3.1: Typical unstable static problem

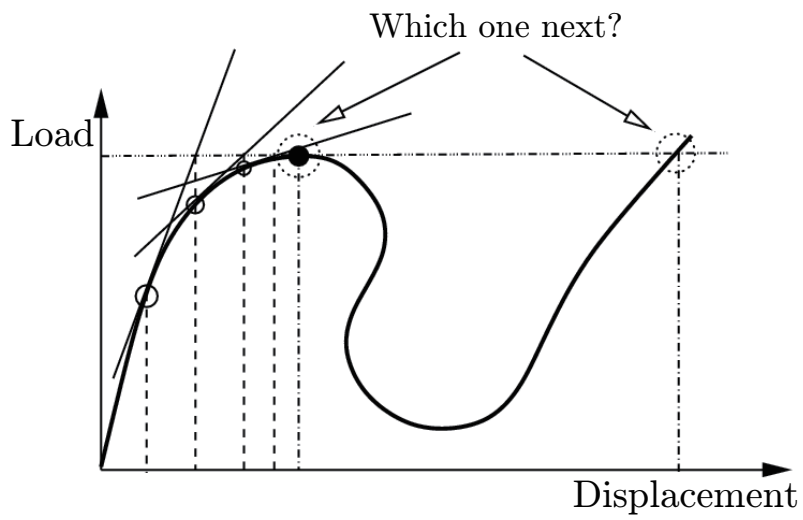


Figure 3.2: The shortcomings of classical Newton-Raphson Method

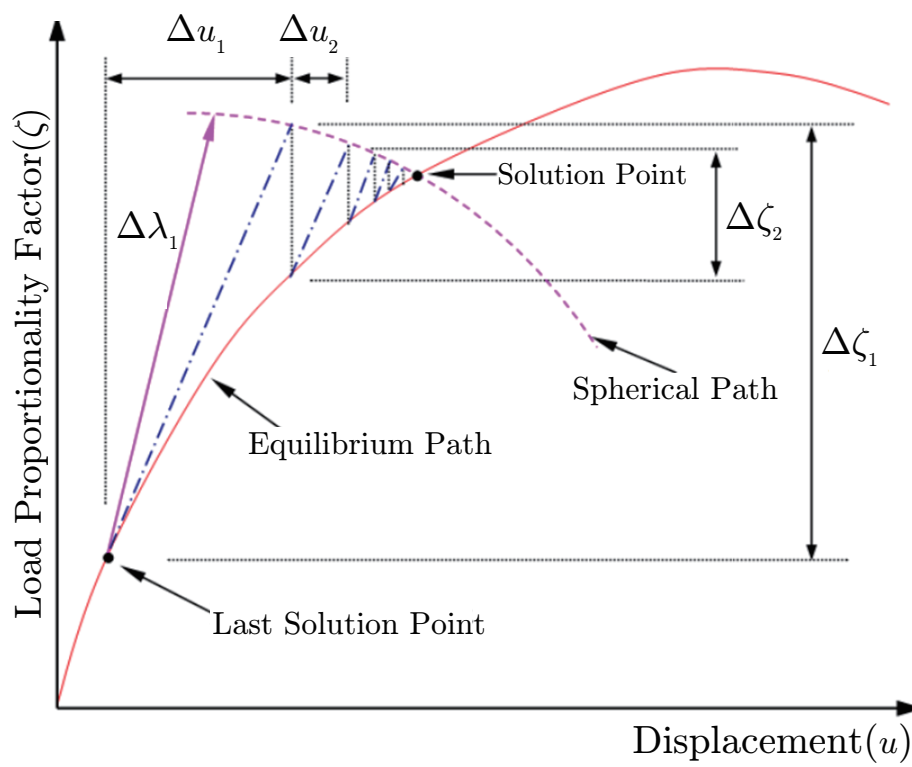


Figure 3.3: The Arc-length Method

Concerning about the material nonlinearity, geometric nonlinearity, or unstable post-buckling behaviour, nonlinear analysis should be considered to perform the buckling simulation. In order to obtain more accurate results, nonlinear buckling analysis which includes post-buckling behavior becomes necessary.

Nonlinear buckling simulation can be divided into 3 steps, pre-buckling, buckling point, and post-buckling. Among them, focus should be given to the post-buckling behavior since this step can influence the stability of the overall structure.

There are several numerical methods that have been created to simulate nonlinear buckling analysis, such as Arc-length Method, artificial damping method, explicit dynamic analysis, and so on. However, among them, the Arc-length Method is the most widely used for post-buckling analysis due to the greater efficiency in tracing the equilibrium trajectory with nonlinear behavior. The explanation of Arc-length Method will be introduced in Section 3.2.

3.2 Arc-length Method

Incremental-iterative methods are able to perform nonlinear analysis for structural problems. These approaches can trace the equilibrium path by predictor and corrector steps. Most of the iterative techniques follow the classical Newton-Raphson procedure with some modification.

For unstable problems such as nonlinear post-buckling analysis, the equilibrium solution paths is difficult to be exhibited. A typical sample of unstable static problem is shown in Figure 3.1. Moreover, the classical Newton's method can not solve these problems where equilibrium solution paths need to be traced beyond limit points (Figure 3.2).

Therefore, Arc-length Method is created to overcome these problems in Newton-Raphson Method. The Arc-length Method is also named as Modified Riks Method, originally created by Riks and Wempner. In 1979, Riks [70] introduced the constant Arc-length which could pass the limit and turning point.

The Arc-length Method is a solution strategy in which the path

through a converged solution, at any step, follows a direction orthogonal to the tangent of the solution curve. It is widely used for the analysis of unstable structures which needs to be traced beyond limit points.

Abaqus/Standard uses the incremental Arc-length, $\Delta\lambda$, trace along the static equilibrium path in load-displacement space. A schematic principle for Arc-length Method is shown in Figure 3.3. The \mathbf{u} means the displacement, and the ζ is the load proportionality factor in the figure. The load proportionality factor can be defined as the limiting value of each iteration where the loads during a scenario are modified step by step until the convergence is reached. The load proportionality factor can be used to calculate for the current magnitude of load of the whole model at each increment. The data of load proportionality factor at each increment is stored in history output of Abaqus/Standard where the users can download it immediately.

3.3 The effect of geometric imperfection

In fact, there are various kinds of imperfections inside the actual structures, such as the load applied or the geometry of the structure. To obtain a correct post-buckling behavior, it is necessary to consider the imperfections of the shape or the loading in the real structure. The simulation of bifurcation for buckling phenomenon can turn to be a problem with continuous response with the help of initial imperfections, as shown in Figure 3.4. When the analysis comes to the bifurcation, the path is turned to be a smooth primary path instead of the secondary path. Imperfections are usually introduced by perturbations in the geometry. The Arc-length Method of Abaqus/Standard can introduce a geometric imperfection pattern for the original model, and then some response in the buckling mode occurs before the exact load is reached.

To complete a post-buckling analysis, an initial deformed shape should be created by using the deformed shape from a linear eigenvalue buckling analysis. Thus an eigenvalue buckling analysis will produce critical buckling loads and buckled shapes on the “perfect” structure at first. A factored deformed shape from this linear buckling analysis

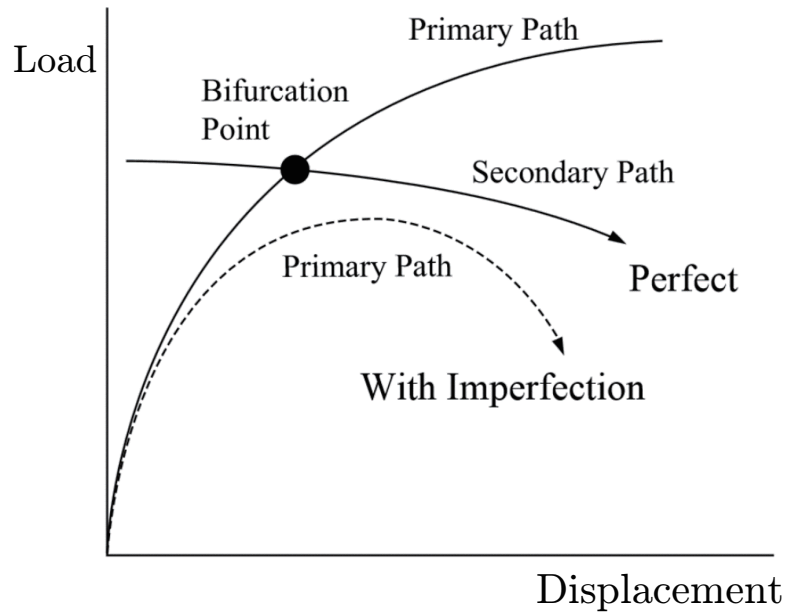


Figure 3.4: A schematic principle for Imperfection [8]

can then be used as the initial mesh for a further nonlinear buckling analysis to develop post-buckling behavior. The critical imperfections are added to the lowest buckling modes to create the perturbed mesh in Abaqus/Standard.

3.4 Nonlinear buckling analysis by FEM

3.4.1 Elastic deformation problem by means of non-elastic strain

In this study, growth of vertebrae in the growth period can be considered as increasing mass in the epiphyseal growth plates. To simulate growth phenomena, an elastic deformation problem is formulated by means of generation of a non-elastic strain by taking into account large deformation theory [10].

Let $\Omega^0 \subset \mathbf{R}^3$ and Γ^0 ($\bar{\Omega}^0 = \Omega^0 \cup \Gamma^0$) be a three-dimensional domain and its boundary of an elastic body of initial position at time $t = 0$,

and $\mathbf{X} = (X_i)_i \in \Omega^0$ be a position of a material point defined in Ω^0 . Let the elastic body deform by generation of a non-elastic strain in accordance with time $t \in (0, T)$ and a material point at $\mathbf{X} \in \Omega^0$ move to $\mathbf{x}(\mathbf{X}, t) = (x_i(\mathbf{X}, t))_i \in \Omega^t$ while restricting displacement on $\Gamma_0^0 \times (0, T)$ for a sub-boundary $\Gamma_0^0 \subset \Gamma^0$ (measure of Γ_0^0 is not zero). Using the Lagrangian description, let displacement $\mathbf{u}(\mathbf{X}, t) = (u_i(\mathbf{X}, t))_i$ and its admissible set U be defined as

$$\mathbf{u} = \mathbf{x}(\mathbf{X}, t) - \mathbf{X}, \quad (3.4.1)$$

$$U = \left\{ \mathbf{u} \in (H^1(\Omega^0 \times (0, T)))^3 \mid \mathbf{u} = \mathbf{0} \text{ on } \Gamma_0^0 \right\}. \quad (3.4.2)$$

Let the non-elastic strain be given with the definition of the Green-Lagrange strain $\bar{\mathbf{E}}(\mathbf{X}, t) = (\bar{E}_{ij}(\mathbf{X}, t))_{ij} \in (L^\infty(\Omega^0 \times (0, T)))^{3 \times 3}$ and the bone be the Saint-Venant material defined in terms of the Hooke's law relationship between second Piola-Kirchhoff stress tensor $S_{ij}(\mathbf{u})$ and the elastic part of the Green-Lagrange strain tensor $E_{ij}(\mathbf{u})$ by

$$S_{ij}(\mathbf{u}) = C_{ijkl} (E_{kl}(\mathbf{u}) - \bar{E}_{kl}), \quad (3.4.3)$$

$$E_{ij}(\mathbf{u}) = \frac{1}{2} (F_{ki}(\mathbf{u})F_{kj}(\mathbf{u}) - \delta_{ij}) = E_{ij}^L(\mathbf{u}) + \frac{1}{2} E_{ij}^{BL}(\mathbf{u}, \mathbf{u}), \quad (3.4.4)$$

where $C_{ijkl}(\mathbf{X}) \in L^\infty(\Omega^0)$ is the stiffness tensor, δ_{ij} denotes Kronecker's delta, and the deformation gradient tensor $F_{ij}(\mathbf{u})$ and the tensors of linear form $E_{ij}^L(\mathbf{u})$ and the bilinear form $E_{ij}^{BL}(\mathbf{u}, \mathbf{v})$ are defined by

$$F_{ij}(\mathbf{u}) = \frac{\partial x_i}{\partial X_j}, \quad (3.4.5)$$

$$E_{ij}^L(\mathbf{u}) = \frac{1}{2} \left(\frac{\partial u_i}{\partial X_j} + \frac{\partial u_j}{\partial X_i} \right), \quad (3.4.6)$$

$$E_{ij}^{BL}(\mathbf{u}, \mathbf{v}) = \frac{1}{2} \left(\frac{\partial v_k}{\partial X_i} \frac{\partial u_k}{\partial X_j} + \frac{\partial u_k}{\partial X_i} \frac{\partial v_k}{\partial X_j} \right). \quad (3.4.7)$$

In this study, the summation convention for indices is used.

The equilibrium equation given by the velocity of the Cauchy stress can be converted to the weak forms in the total Lagrange description using the second Piola-Kirchhoff stress and the Green-Lagrange strain

by multiplying the equilibrium equation with a variational displacement $\mathbf{v} \in U$ and integrating over Ω^0 and $(0, T)$ as

$$\int_0^T \int_{\Omega^0} S_{ij}(\mathbf{u}) \delta E_{ij}(\mathbf{u}, \mathbf{v}) \, dX dt = 0 \quad \forall \mathbf{v} \in U, \quad (3.4.8)$$

$$\int_0^T \int_{\Omega^0} \left(\dot{S}_{ij}(\mathbf{u}) \delta E_{ij}(\mathbf{u}, \mathbf{v}) + S_{ij}(\mathbf{u}) \delta \dot{E}_{ij}(\mathbf{u}, \mathbf{v}) \right) \, dX dt = 0 \\ \forall \mathbf{v} \in U, \quad (3.4.9)$$

where the variational terms $\delta(\cdot)$ and derivatives with respect to time $(\dot{\cdot}) = \partial(\cdot)/\partial t$ are defined by

$$\delta F_{ij}(\mathbf{v}) = \frac{\partial v_i}{\partial X_j}, \quad (3.4.10)$$

$$\delta E_{ij}(\mathbf{u}, \mathbf{v}) = \frac{1}{2} (\delta F_{ki}(\mathbf{v}) F_{kj}(\mathbf{u}) + F_{ki}(\mathbf{u}) \delta F_{kj}(\mathbf{v})) \\ = E_{ij}^L(\mathbf{v}) + E_{ij}^{BL}(\mathbf{u}, \mathbf{v}), \quad (3.4.11)$$

$$\delta \dot{E}_{ij}(\mathbf{u}, \mathbf{v}) = E_{ij}^L(\dot{\mathbf{v}}) + E_{ij}^{BL}(\dot{\mathbf{u}}, \mathbf{v}) + E_{ij}^{BL}(\mathbf{u}, \dot{\mathbf{v}}) \\ = E_{ij}^{BL}(\dot{\mathbf{u}}, \mathbf{v}), \quad (3.4.12)$$

$$\dot{S}_{ij}(\mathbf{u}) = C_{ijkl} \left(\dot{E}_{kl}(\mathbf{u}) - \dot{\bar{E}}_{kl} \right), \quad (3.4.13)$$

$$\dot{E}_{ij}(\mathbf{u}) = E_{ij}^L(\dot{\mathbf{u}}) + E_{ij}^{BL}(\dot{\mathbf{u}}, \mathbf{u}). \quad (3.4.14)$$

As $\mathbf{v} \in U$ is arbitrary, we set $\dot{\mathbf{v}} = \mathbf{0}$.

By substituting Eqs. from (3.4.11) to (3.4.14) into Eqs. (3.4.8) and (3.4.9), we can obtain the weak form for FEM as

$$\int_0^T a^{\text{NL}}(\mathbf{u}, \mathbf{v}) \, dt = \int_0^T b(\bar{\mathbf{E}}, \mathbf{u}, \mathbf{v}) \, dt, \quad (3.4.15)$$

$$\int_0^T \left(a^L(\dot{\mathbf{u}}, \mathbf{v}) + a^{\text{NL1}}(\mathbf{u}, \dot{\mathbf{u}}, \mathbf{v}) + a^{\text{NL2}}(\mathbf{u}, \dot{\mathbf{u}}, \mathbf{v}) \right) \, dt \\ = \int_0^T b(\dot{\bar{\mathbf{E}}}, \mathbf{u}, \mathbf{v}) \, dt, \quad (3.4.16)$$

by using definitions as

$$\begin{aligned}
& a^{\text{NL}}(\mathbf{u}, \mathbf{v}) \\
&= \int_{\Omega^0} C_{ijkl} \left(E_{kl}^{\text{L}}(\mathbf{u}) + \frac{1}{2} E_{kl}^{\text{BL}}(\mathbf{u}, \mathbf{u}) \right) \left(E_{ij}^{\text{L}}(\mathbf{v}) + \frac{1}{2} E_{ij}^{\text{BL}}(\mathbf{v}, \mathbf{v}) \right), \tag{3.4.17}
\end{aligned}$$

$$a^{\text{L}}(\dot{\mathbf{u}}, \mathbf{v}) = \int_{\Omega^0} C_{ijkl} E_{kl}^{\text{L}}(\dot{\mathbf{u}}) E_{ij}^{\text{L}}(\mathbf{v}) \, dX, \tag{3.4.18}$$

$$\begin{aligned}
a^{\text{NL1}}(\mathbf{u}, \dot{\mathbf{u}}, \mathbf{v}) &= \int_{\Omega^0} C_{ijkl} (E_{kl}^{\text{BL}}(\dot{\mathbf{u}}, \mathbf{u}) E_{ij}^{\text{L}}(\mathbf{v}) \\
&\quad + E_{klj}^{\text{L}}(\dot{\mathbf{u}}) E_{ij}^{\text{BL}}(\mathbf{u}, \mathbf{v}) + E_{kl}^{\text{BL}}(\dot{\mathbf{u}}, \mathbf{u}) E_{ij}^{\text{BL}}(\mathbf{u}, \mathbf{v})) \, dX, \tag{3.4.19}
\end{aligned}$$

$$a^{\text{NL2}}(\mathbf{u}, \dot{\mathbf{u}}, \mathbf{v}) = \int_{\Omega^0} S_{ij}(\mathbf{u}) E_{ij}^{\text{BL}}(\dot{\mathbf{u}}, \mathbf{v}) \, dX, \tag{3.4.20}$$

$$b(\bar{\mathbf{E}}, \mathbf{u}, \mathbf{v}) = \int_{\Omega^0} C_{ijkl} \bar{E}_{kl} (E_{ij}^{\text{L}}(\mathbf{v}) + E_{ij}^{\text{BL}}(\mathbf{u}, \mathbf{v})) \, dX. \tag{3.4.21}$$

3.4.2 Nonlinear buckling analysis

Equation (3.4.16) can be solved by FEM. Let $\Omega_h^0 = \bigcup_{e \in \mathcal{I}} \Omega^e$, \mathcal{I} , \mathcal{N} and \mathcal{N}_0 be sets of numbers for finite elements, nodes and nodes on Γ_0^0 respectively, \mathcal{N}^e be a set of node numbers for element e , and $|\mathcal{N}|$ be the number of nodes. Let $P_k(\Omega^e)$ denote a set of polynomials defined on Ω^e used as the interpolation function $N_\alpha^e(\mathbf{X})$ ($\alpha \in \mathcal{N}^e$, $\mathbf{X} \in \Omega^e$) in which the k -th order polynomial space is included. Let us define an approximation space U_h and nodal vector \mathbf{u} using nodal displacement $\mathbf{u}_\alpha = (u_{i\alpha})_i \in (C((0, T)))^3$ as

$$\begin{aligned}
U_h &= \left\{ \mathbf{u}_h \in (C(\bar{\Omega}^0 \times (0, T)))^3 \mid \right. \\
&\quad \left. \mathbf{u}_h|_{\Omega^e} = \sum_{\alpha \in \mathcal{N}^e} N_\alpha^e \mathbf{u}_\alpha \in P_k(\Omega^e) \, \forall e \in \mathcal{I}, \mathbf{u}_h|_{\Gamma_{0h}} = \mathbf{0} \right\}, \tag{3.4.22}
\end{aligned}$$

$$\mathbf{u} = (\mathbf{u}_\alpha)_{\alpha \in \mathcal{N} \setminus \mathcal{N}_0} \in (C((0, T)))^{|\mathcal{N} \setminus \mathcal{N}_0|}, \tag{3.4.23}$$

and discretize \mathbf{u} in time into $\mathbf{u}^0 = \mathbf{0}$ and $\mathbf{u}^{k+1} = \mathbf{u}^k + \Delta \mathbf{u}^k$ ($k = 1, 2, 3, \dots$) using notations $(\cdot)(t^k) = (\cdot)^k$ for $t^0 = 0$ and $t^{k+1} =$

$t^k + \Delta t^k$. Introducing $\mathbf{u}_h, \mathbf{v}_h \in U_h \subset U$, Eqs. (3.4.15) and (3.4.16) can be converted into

$$\mathbf{Q}^{k+1} = \mathbf{F}^{k+1}, \quad (3.4.24)$$

$$\mathbf{K}^{k+1} \Delta \mathbf{u}^k = (\mathbf{K}^L + \mathbf{K}^{\text{NL1},k+1} + \mathbf{K}^{\text{NL2},k+1}) \Delta \mathbf{u}^k = \Delta \mathbf{F}^k, \quad (3.4.25)$$

where $\mathbf{Q}^k, \mathbf{F}^k, \mathbf{K}^L, \mathbf{K}^{\text{NL1},k}, \mathbf{K}^{\text{NL2},k}$ and $\Delta \mathbf{F}^k$ are defined as

$$\begin{aligned} \mathbf{Q}^k &= \mathbf{Q}(\mathbf{u}_h^k) = (\mathbf{Q}_\alpha)_{\alpha \in \mathcal{N}^e}, \\ \mathbf{Q}_\alpha &= \sum_{e \in \mathcal{I}} a^{\text{NL}}(\mathbf{u}_h^k, \mathbf{N}_\alpha^e), \end{aligned} \quad (3.4.26)$$

$$\begin{aligned} \mathbf{F}^k &= \mathbf{F}(\bar{\mathbf{E}}^k, \mathbf{u}_h^k) = (\mathbf{F}_\alpha)_{\alpha \in \mathcal{N}^e}, \\ \mathbf{F}_\alpha &= \sum_{e \in \mathcal{I}} b(\bar{\mathbf{E}}^k, \mathbf{u}_h^k, \mathbf{N}_\alpha^e), \end{aligned} \quad (3.4.27)$$

$$\begin{aligned} \mathbf{K}^L &= (\mathbf{K}_{\alpha\beta}^L)_{\alpha, \beta \in \mathcal{N}^e}, \\ \mathbf{K}_{\alpha\beta}^L &= \sum_{e \in \mathcal{I}} a^L(\mathbf{N}_\alpha^e, \mathbf{N}_\beta^e), \end{aligned} \quad (3.4.28)$$

$$\begin{aligned} \mathbf{K}^{\text{NL1},k} &= \mathbf{K}^{\text{NL1}}(\mathbf{u}_h^k) = (\mathbf{K}_{\alpha\beta}^{\text{NL1}})_{\alpha, \beta \in \mathcal{N}^e}, \\ \mathbf{K}_{\alpha\beta}^{\text{NL1}} &= \sum_{e \in \mathcal{I}} a^{\text{NL1}}(\mathbf{u}_h^k, \mathbf{N}_\alpha^e, \mathbf{N}_\beta^e), \end{aligned} \quad (3.4.29)$$

$$\begin{aligned} \mathbf{K}^{\text{NL2},k} &= \mathbf{K}^{\text{NL2}}(\mathbf{u}_h^k) = (\mathbf{K}_{\alpha\beta}^{\text{NL2}})_{\alpha, \beta \in \mathcal{N}^e}, \\ \mathbf{K}_{\alpha\beta}^{\text{NL2}} &= \sum_{e \in \mathcal{I}} a^{\text{NL2}}(\mathbf{u}_h^k, \mathbf{N}_\alpha^e, \mathbf{N}_\beta^e), \end{aligned} \quad (3.4.30)$$

$$\begin{aligned} \Delta \mathbf{F}^k &= \Delta \mathbf{F}^k(\Delta \bar{\mathbf{E}}^k, \mathbf{u}_h^k) = (\dot{\mathbf{F}}_\alpha)_{\alpha \in \mathcal{N}^e}, \\ \dot{\mathbf{F}}_\alpha &= \sum_{e \in \mathcal{I}} b(\Delta \bar{\mathbf{E}}^k, \mathbf{u}_h^k, \mathbf{N}_\alpha^e). \end{aligned} \quad (3.4.31)$$

In this study, the non-elastic strain $\bar{\mathbf{E}}(\mathbf{X}, t)$ can be written in the form of separation of variables by

$$\bar{\mathbf{E}}(\mathbf{X}, t) = \zeta(t) \bar{\mathbf{E}}_0(\mathbf{X}), \quad (3.4.32)$$

where $\bar{\mathbf{E}}_0(\mathbf{X}) \in (L^\infty(\Omega^0))^{3 \times 3}$ and $\zeta(t) \in C((0, T))$ are growth strain mode to yield a basic growth pattern and growth rate to give the magnitude increasing in accordance with time, respectively. Introducing the relationship, Eqs. (3.4.24) and (3.4.25) can be converted by

$$\mathbf{Q}^{k+1} = \zeta^{k+1} \bar{\mathbf{F}}_0^{k+1}, \quad (3.4.33)$$

$$\mathbf{K}^{k+1} \Delta \mathbf{u}^k = \Delta \zeta^k \bar{\mathbf{F}}_0, \quad (3.4.34)$$

where $\bar{\mathbf{F}}_0^k$ is defined by

$$\bar{\mathbf{F}}_0^k = \bar{\mathbf{F}}_0(\bar{\mathbf{E}}_0, \mathbf{u}_h^k) = (\bar{\mathbf{F}}_{0\alpha})_\alpha, \quad \bar{\mathbf{F}}_{0\alpha} = \sum_{e \in \mathcal{I}} b(\bar{\mathbf{E}}_0, \mathbf{u}_h^k, \mathbf{N}_\alpha^e). \quad (3.4.35)$$

In this study, to compute deformation path including unstable phenomena, we employed the Arc-length Method, in which $\Delta \mathbf{u}^k$ and $\Delta \zeta^k$ are determined by

$$\int_{\Omega^0} (\mathbf{u}_h \cdot \mathbf{u}_h + \Delta \zeta^2 \mathbf{f}_h \cdot \mathbf{f}_h) dx = (\Delta \lambda)^2, \quad (3.4.36)$$

where $\mathbf{u}_h \Big|_{\Omega^0} = \sum_{\alpha \in N^e} N_\alpha^e \mathbf{u}_\alpha$, $\mathbf{f}_h \Big|_{\Omega^0} = \sum_{\alpha \in N^e} N_\alpha^e \mathbf{F}_\alpha$, and $\Delta \lambda$ is a given constant called the incremental Arc-length. The nonlinear problem given by Eqs. (3.4.33), (3.4.34) and (3.4.36) was solved by Newton-Raphson iteration.

The buckling point can be defined by the condition that \mathbf{K}^{k+1} becomes a singular matrix:

$$\det(\mathbf{K}^{k+1}) = 0. \quad (3.4.37)$$

At this point, the minimum eigenvalue $\omega_1 = 0$ and eigenmode ϕ_1 , which is called buckling mode, can be defined by

$$\mathbf{K}^{k+1} \phi_1 = \omega_1 \phi_1. \quad (3.4.38)$$

By taking the inner product between both parts of Eq. (3.4.33) and ϕ_1 , the following relationships hold at the buckling point.

$$\phi_1 \cdot (\mathbf{K}^{k+1} \Delta \mathbf{u}^k) = \omega_1 \phi_1 \cdot \Delta \mathbf{u}^k = \Delta \zeta^k \phi_1 \cdot \bar{\mathbf{F}}_0 = 0. \quad (3.4.39)$$

When Eq. (3.4.39) is satisfied by $\phi_1 \cdot \bar{\mathbf{F}}_0 \neq 0$, $\Delta\zeta^k = 0$, this point is called the limit point. At this point, we can compute the deformation path by the Arc-length Method. Conversely, when Eq. (3.4.39) is satisfied by $\phi_1 \cdot \bar{\mathbf{F}}_0 = 0$, this point is called the bifurcation point. In addition, when both conditions of $\phi_1 \cdot \bar{\mathbf{F}}_0 = 0$ and $\Delta\zeta = 0$ are satisfied, this point is called the symmetric bifurcation point. At these bifurcation points, we have to analyze the eigenmodes ϕ_1 by appropriate methods.

To judge buckling points, we employed a method using decomposition of the tangent stiffness matrix $\mathbf{K} = \mathbf{L}\mathbf{D}\mathbf{L}^T$, in which \mathbf{L} and \mathbf{D} denote the lower triangular and diagonal matrices [71, 72]. Using this method, we monitor the number of negative elements in \mathbf{D} and identify passing the buckling points when the number changes. For the analysis of ϕ_1 , we employed both the scaled corrector method and the block Lanczos method, and confirmation was achieved in accordance with these results by interactive operation.

3.5 Post-buckling analysis in Abaqus

In this research, all the nonlinear post-buckling analyses were conducted by the finite element software package, Abaqus 6.12 Edition (Abaqus, Inc.). The flowchart for post-buckling analysis in Abaqus is shown in Figure 3.5. Before the Arc-length Method can be performed, the linear eigenvalue buckling analysis for the same model should be firstly completed. After the linear eigenvalue buckling analysis, the .fil file is obtained and the eigenmode from the Abaqus/Standard can be chosen. And then, users can introduce the imperfections into the .inp file through that .fil file. The keywords *STATIC, RIKS and *IMPERFECTION are used when post-buckling analysis in .inp file is performed.

3.6 Model

After comparing the numbers of buckling mode for each model in Chapter 2, Model 1, which buckled easily, was used for the nonlinear post-buckling analysis in this chapter. The height and depth of this

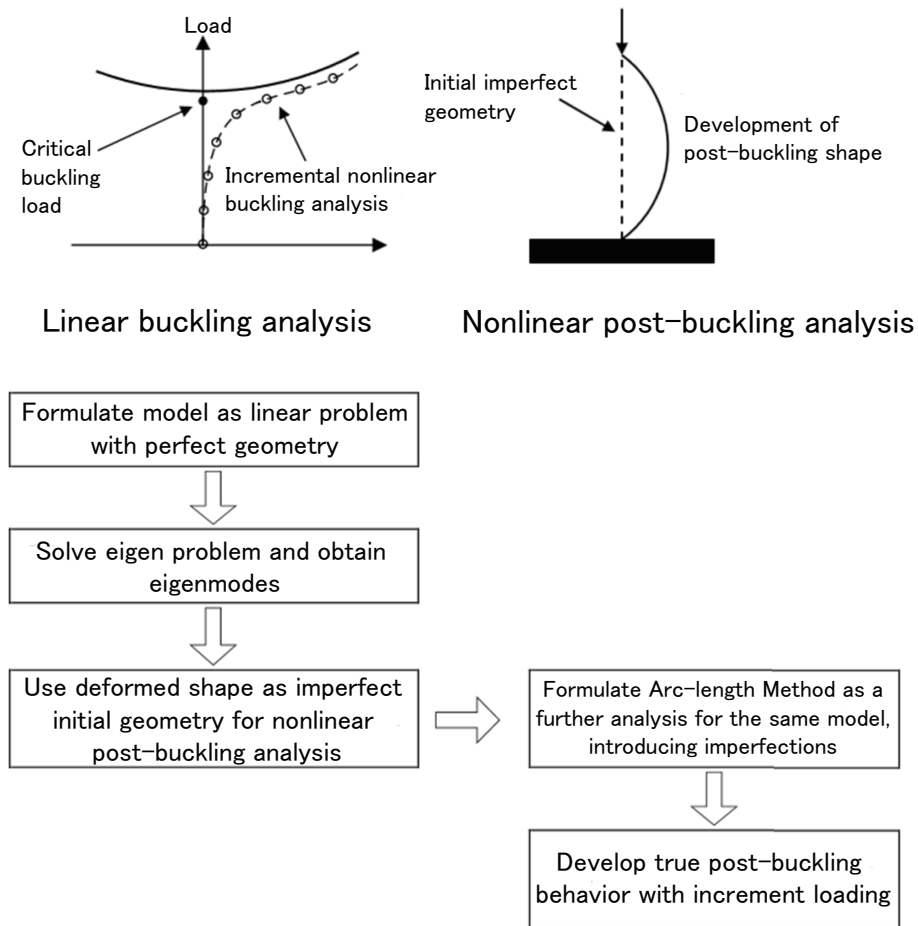


Figure 3.5: Flowchart of post-buckling analysis procedure in Abaqus

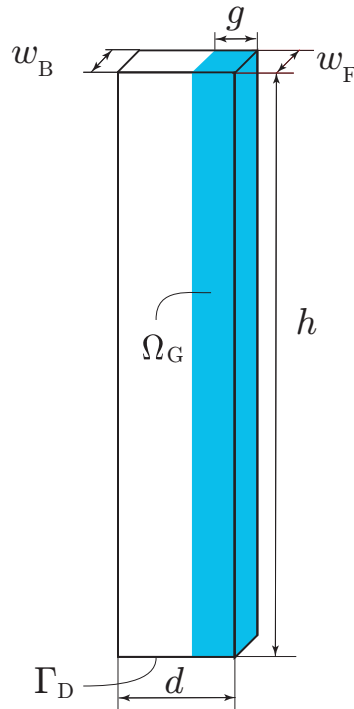


Figure 3.6: The plate model

plate model is set to be $h = 500$ mm and $d = 50$ mm, respectively, as same as the models in Chapter 2. In this chapter, the width of the model is set as $w_F = w_B = 6$ mm, which is expected to cause more buckling models to the model. Young's modulus and Poisson's ratio is still assumed to be 8 [MPa] and 0.3, respectively. This plate model consists of 403,781 nodes and 265,812 elements. All elements are second-order tetrahedron (C3D10 in Abaqus/Standard).

For the boundary conditions, we still assigned a fixed boundary Γ_D at the bottom of the model. The growth pattern g was assumed to take the value of 1 in the areas shown in red in Figure 3.6, and the value 0 elsewhere. The value of 0.1 was used for the initial growth rate.

3.7 Result

Firstly, the linear buckling analysis was completed by using the simple model, and the 1st Mode, 2nd Mode, 3rd Mode, 4th Mode of the linear buckling were obtained. Then the geometric imperfection patterns were introduced to the modes respectively before the nonlinear post-buckling analysis. The imperfect initial geometry for each Mode is $\alpha w_1 = 5.0$ mm, $\alpha w_2 = 6.0$ mm, $\alpha w_3 = 5.9$ mm, and $\alpha w_4 = 5.0$ mm.

After the nonlinear post-buckling analysis, the 1st Mode, 2nd Mode, 3rd Mode, 4th Mode are shown in Figure 3.7, Figure 3.9, Figure 3.11, and Figure 3.13, respectively.

From these results, we can see, the deformation for the 2nd Mode and 3rd Mode are identified similar to the clinical scoliotic curves.

The relationship between the current load proportionality factor and Arc-length for the 1st Mode, the 2nd Mode, the 3rd Mode, the 4th Mode are shown in Figure 3.8, Figure 3.10, Figure 3.12, and Figure 3.14, respectively.

3.8 Discussion

From the results of the history of the load proportionality factor and the Arc-length for all types of modes, the result for the 3rd Mode is appear to be different from the others.

For the 3rd Mode, the model is inverted to the right and left with large deformation during the analysis, which is shown in Figure 3.15. And the load proportionality factor turns to negative value from the latter part of the analysis. From these results, the existence of the unstable nonlinear post-buckling phenomena can be observed in the case of 3rd Mode.

For the other three modes, the analysis finished with small Arc-length. When the increment decreases gradually, the equilibrium solution paths could not be found, and the deformation of the model was large enough, which made the simulation come to completion at the end of the equilibrium path.

From the results of Mode1, Mode 2, and Mode 3, when the load proportionality factor is around 10, the changing of path occurred,

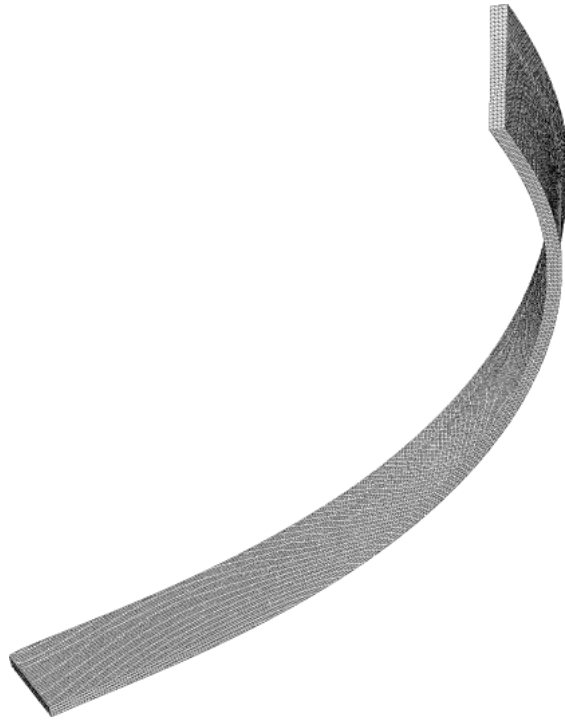


Figure 3.7: The 1st Mode from nonlinear growth deformations of plate model with initial imperfections ($\lambda = 12.16$)

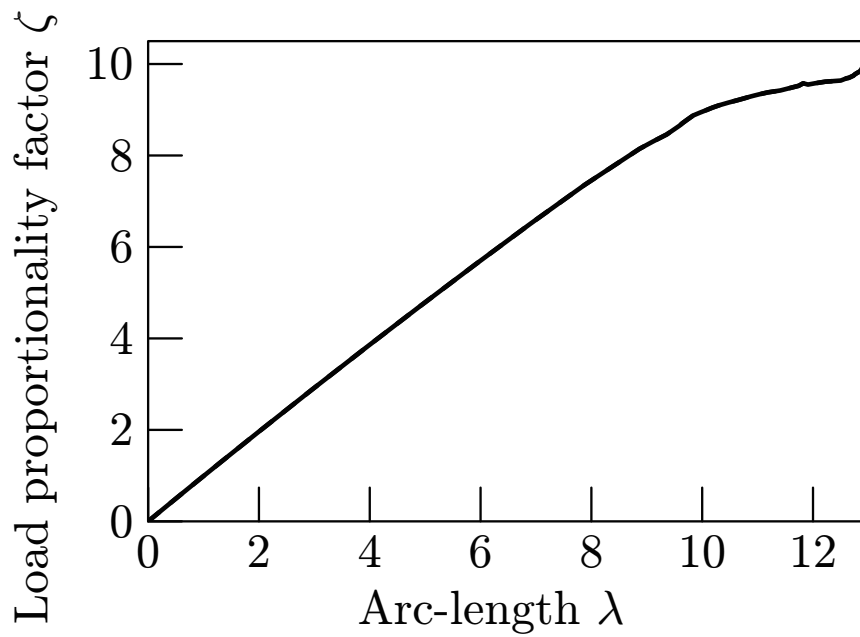


Figure 3.8: History of load proportionality factor for the 1st Mode



Figure 3.9: The 2nd Mode from nonlinear growth deformations of plate model with initial imperfections ($\lambda = 45.59$)

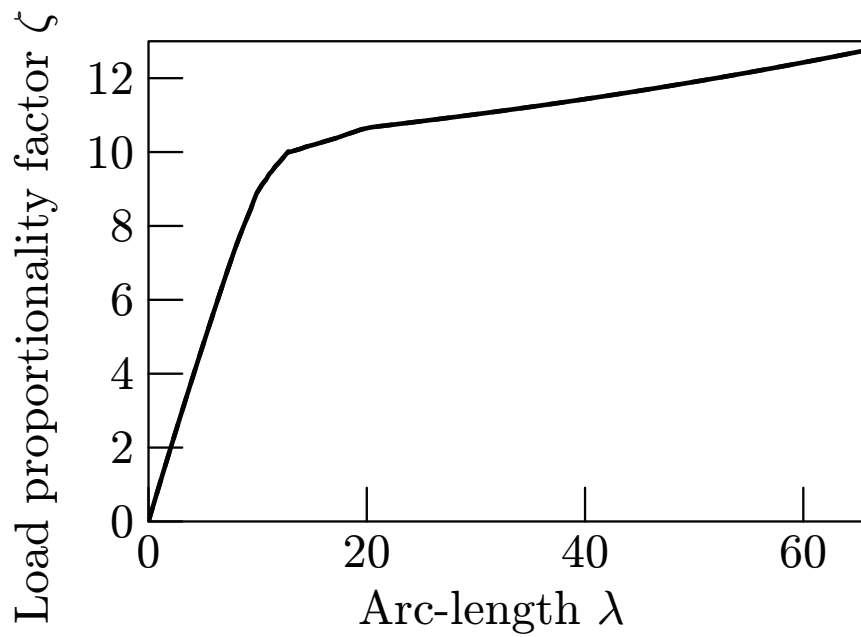


Figure 3.10: History of load proportionality factor for the 2nd Mode

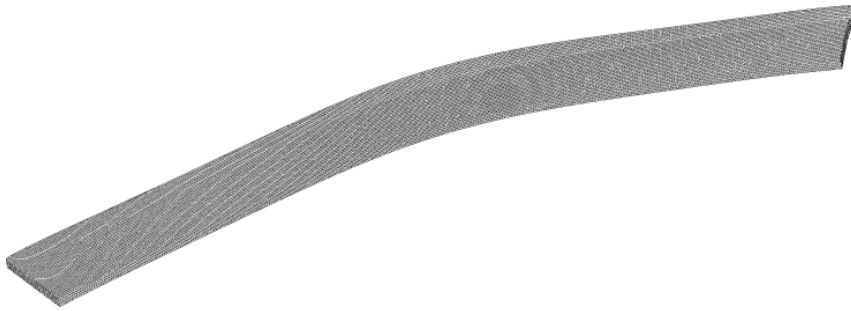


Figure 3.11: The 3rd Mode from nonlinear growth deformations of plate model with initial imperfections ($\lambda = 50.54$)

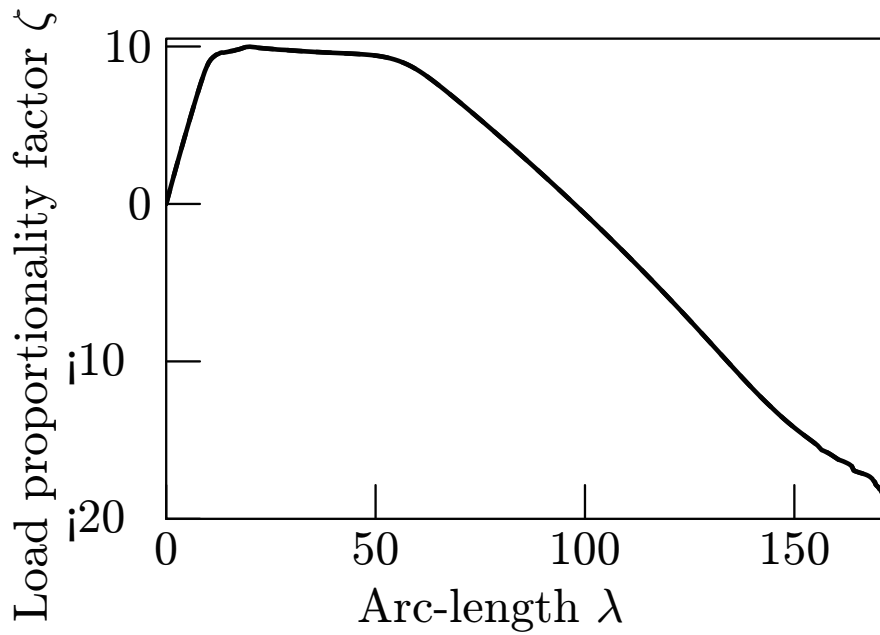


Figure 3.12: History of load proportionality factor for the 3rd Mode



Figure 3.13: The 4th Mode from nonlinear growth deformations of plate model with initial imperfections ($\lambda = 9.359$)

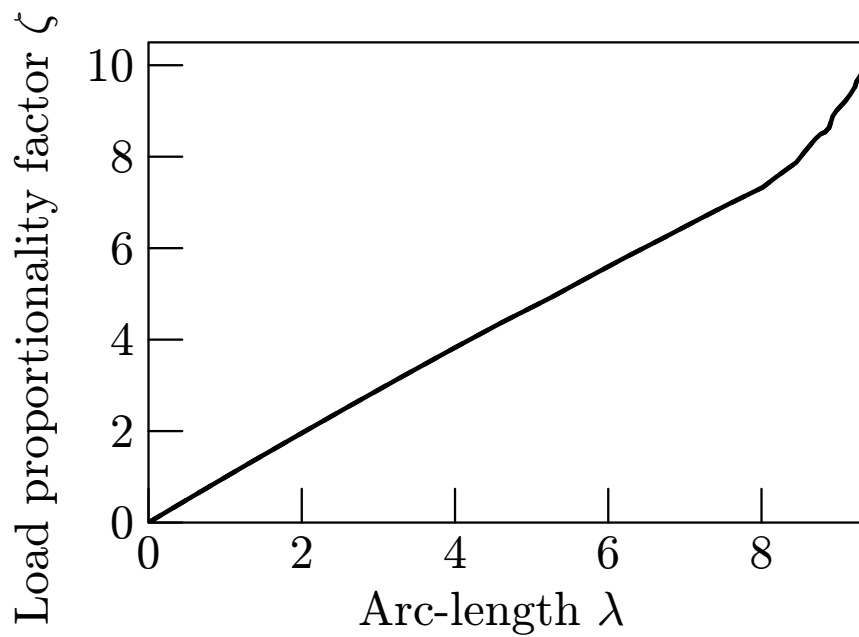


Figure 3.14: History of load proportionality factor for the 4th Mode

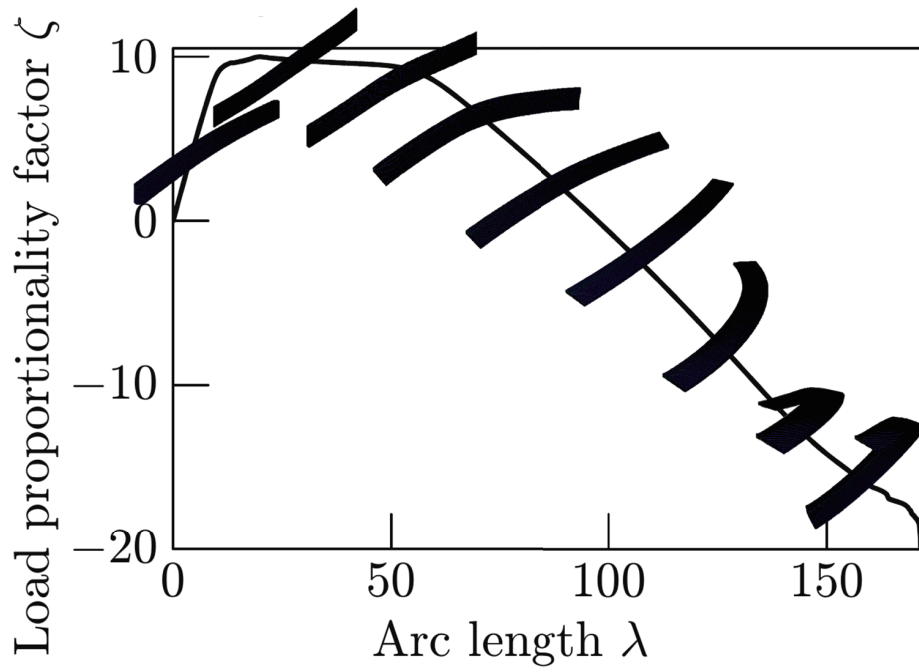


Figure 3.15: History of load proportionality factor for the 3rd mode

which indicated that the nonlinear post-buckling began to occur. Then for Mode 1 (Figure 3.8) and Mode 2 (Figure 3.10), the load proportionality factor increased gradually following the increase of the Arc-length. On the other hand, For the Mode 3, the load proportionality factor decreased after the turning point, which means the unstable large deformation occurred.

From these results, the stable post-buckling deformations were obtained in almost modes of the simple plate model. Especially, an unstable post-buckling deformation was confirmed in the case of the 3rd buckling mode.

3.9 Conclusion

In order to verify the buckling hypothesis, linear buckling analysis was performed in Chapter 2. However, this analysis is only valid for infinitesimal deformation and is not applicable to estimate the stability for post-buckling behavior. In this chapter, we conducted post-buckling simulations caused by the growth of vertebral bodies considering the geometrical nonlinearity using the simple plate model. After introducing initial imperfection to the buckling modes, stable deformations are obtained for almost modes of the simple plate model. Especially, for the 3rd Mode, an unstable post-buckling deformation of the model during the analysis were obtained. Therefore, the existence of the nonlinear buckling phenomena in the simple plate model can be confirmed via the nonlinear growth deformation analysis.

Chapter 4

Linear buckling analysis for spine model

This chapter introduces details of the finite element model of spine used in this research. Section 4.1 summarizes the structure of spine's vertebrae. Section 4.2 reviews the previous works of our research group related to buckling hypothesis. Then, the history and manufacture of the spine model is introduced in Section 4.3. The elements, the material, the boundary conditions and other properties of the spine model are presented in Section 4.4. Next, the results of linear buckling analysis of this spine model is stated in Section 4.5. The required time for a patient to develop to a state of a scoliotic shape as in the 4th Mode of the linear buckling analysis is calculated in the discussion part of Section 4.6. In the end, the conclusion of linear buckling phenomenon for the spine model is summarized in Section 4.7.

4.1 The structure of the spine

4.1.1 Classification of bone

The bone can be classified into two types, cortical bone and cancellous bone. Compact bone is dense bone tissue laied on the facial part of the bone. Inside the cortical bone, there are the trabeculae which is full of holes conecting to each other by rods and plates. Bone marrow contains immature cells inside the interior of the bones. Callcellous

bone also contains lots of bone marrow which fills the space inside trabeculae.

In order to supply nutrition to the cortical bone, small canals runs parallel to the long axis of the bone. These canals, named as Haversian canals, are connected to one another by the Volkmann's canals. The concentric layers, or lamellae, that surrounding the Haversian canals, consists an osteon system.

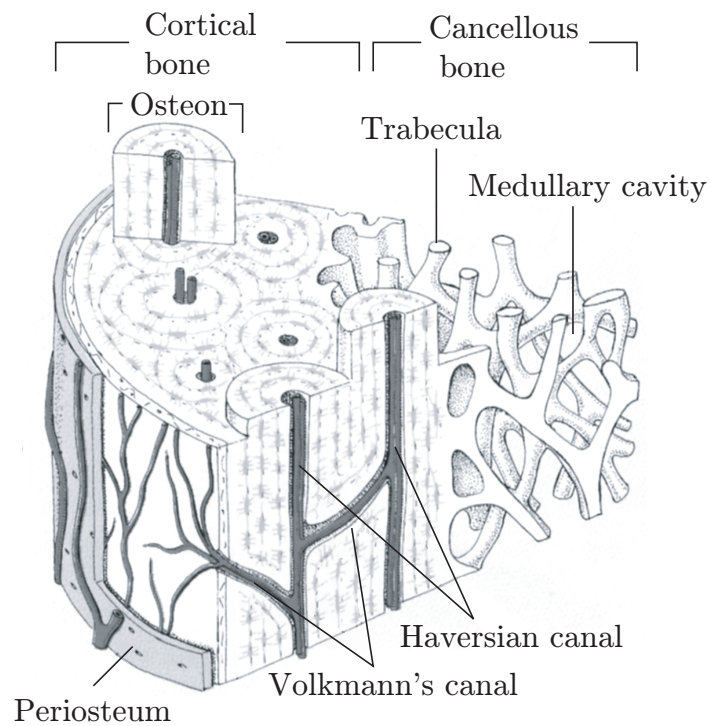


Figure 4.1: The structure of the bone [73]

4.1.2 The structure of the spine

The human vertebral column is also named as the backbone or spine. There are a total of 33 vertebrae in the human vertebral column.

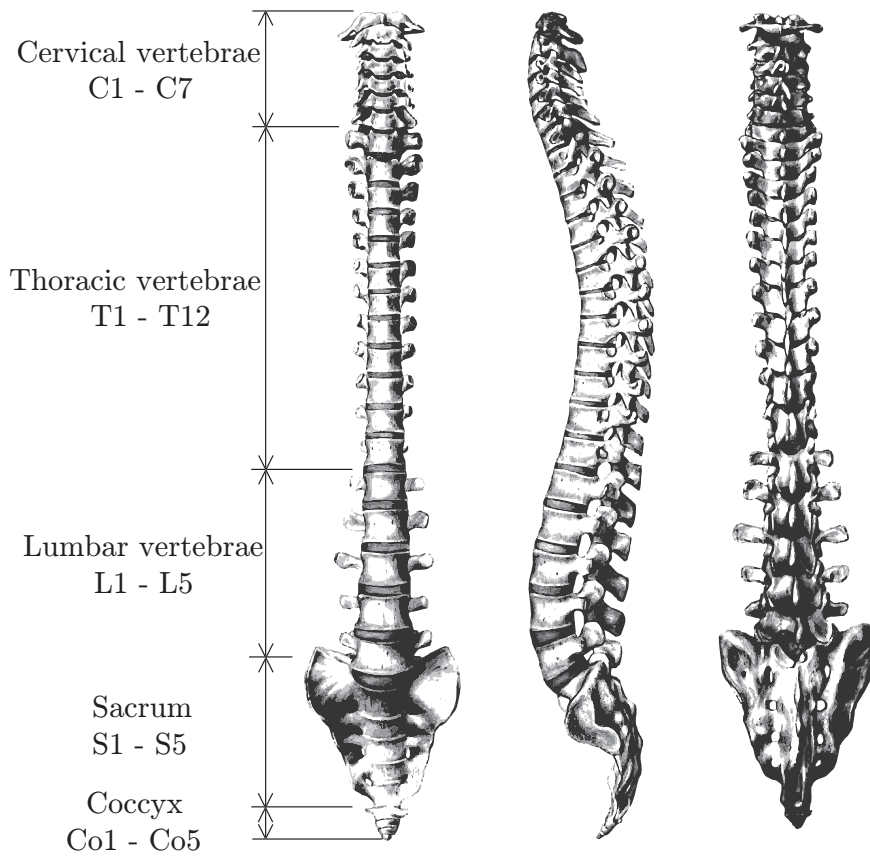


Figure 4.2: Spine [1]

These vertebrae are divided into five regions, the cervical spine, thoracic spine, lumbar spine, sacrum and coccyx. There are seven cervical vertebrae, twelve thoracic vertebrae and five lumbar vertebrae, as shown in Figure 4.2.

4.1.3 The joints of vertebrae

There are different kinds of ligaments as the joints of vertebrae, such as intervertebral disc, zygapophysial joint, anterior longitudinal ligament, posterior longitudinal ligament, ligamentum flavum, interspinous ligament, supraspinous ligament, as shown in Figure 4.3 and 4.4.

The intervertebral disc can be described as the shock-absorber between every vertebra. The intervertebral disc consists of the central nucleus pulposus, and surrounding by the anulus fibrosus. The nucleus pulposus is the core of the disc as shown in Figure 4.3. It consists of jelly-like material and loose network of collagen fibers. The anulus fibrosus is the tough exterior of the intervertebral disc surrounding the nucleus pulposus. It can help distribute pressure or force and pass to the intervertebral disc.

The zygapophysial joints are located on the back of the spine on each side to connect adjacent vertebrae. The joints can help prevent the spine from bending or twisting and keep stability of the spine. The zygapophysial joints consists of cartilage surrounding with capsule.

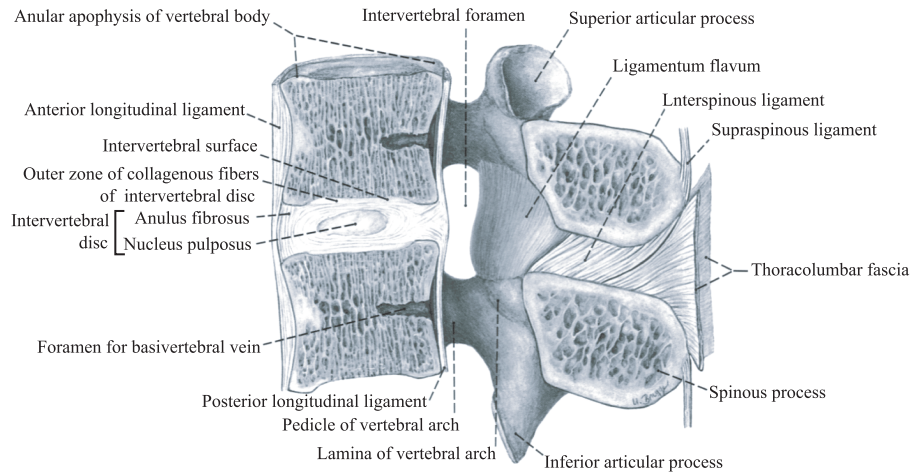


Figure 4.3: Cross sectional view of lumbar vertebrae [1]

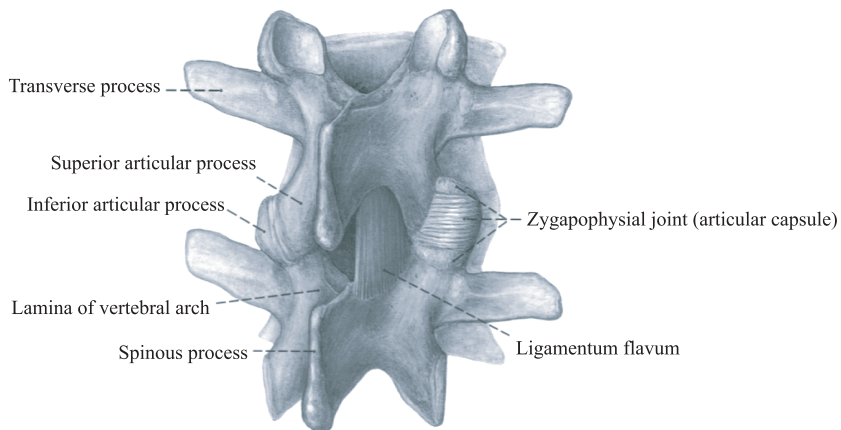


Figure 4.4: Articular capsule of thoracic vertebrae [1]

4.2 Previous researches

Since the function of the spine is to maintain the form of the body, we can consider some mechanical phenomena may cause of the spine to be bent. Various hypothesis on the etiology of idiopathic scoliosis have been proposed for that reason, and one of them is buckling hypothesis. Regarding to the buckling hypothesis, our research group have reviewed the literature and investigated the buckling phenomenon induced by the growth of vertebral bodies.

Starting from 1995, Azegami [74] [75] [76] [63] began to conform the buckling hypothesis with numerical simulation by FEM. The finite element models of spine for early stage, shown in Figure 4.5 were used for the numerical simulations of vertebral growth [77] [78] [79] [80]. From the results of growth analysis, they found the 4th buckling mode was similar to the clinical shape of idiopathic scoliosis. While the 1st buckling mode, 2nd buckling mode and 3rd buckling mode, they can be controlled by posture changes resulting from the muscle system. Moreover, the mechanical spine model was also used to demonstrate the buckling hypothesis on etiology of idiopathic scoliosis [81] [82] [83]. But, no major muscle in the thoracic spine region seems to be the reason why the 4th buckling mode occurs, and be the possible cause of the spinal deformation as etiology of thoracic idiopathic scoliosis [84] [85] [63] [86] [87].

Based on the buckling hypothesis, Takeuchi [7] [88] [89] used the linear buckling theory to analyze the buckling phenomenon induced by the growth of vertebral bodies using FEM. A more exact finite element model of spine with thoracic cage was used for the linear buckling analysis. Heat expansion was applied to the model to allow the growth of vertebrae to occur. Various growth pattern between T1 and L5 were examined. Commercial FEM program MSC. Nastran V70 [90] [91] was used to investigate all valid buckling modes. As a result, they found that the 4th buckling mode were in agreement with clinical shapes for the case of single curve. In some other cases with wide range of growth part, 6th buckling mode was similar to the clinical shapes for the case of double curve. Some of the buckling modes which are in agreement with clinical shapes are shown in Figure 4.7. Critical growth with respect to the 4th buckling mode and 6th buckling mode are shown

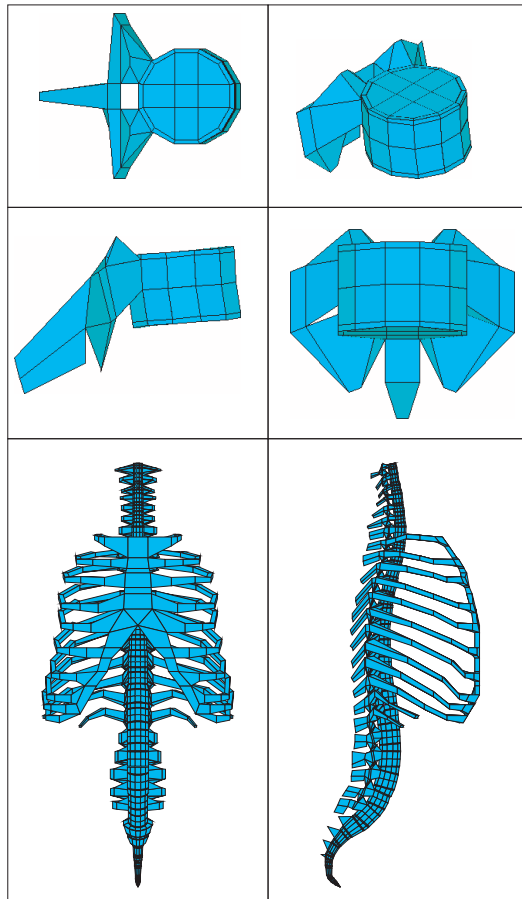


Figure 4.5: Previous spine model (1995)

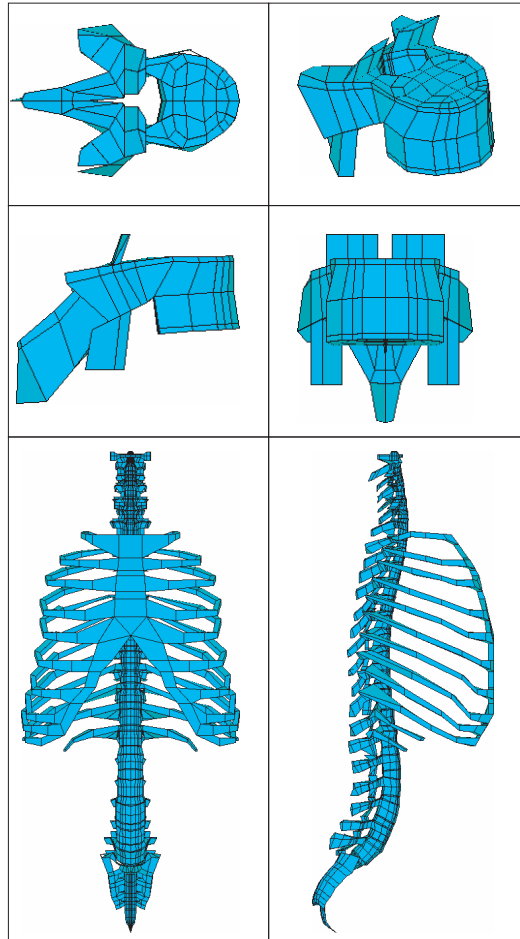
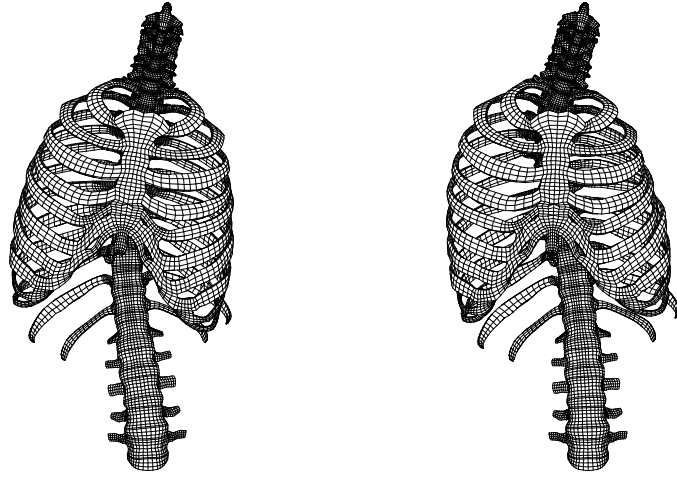


Figure 4.6: Previous spine model (1996)

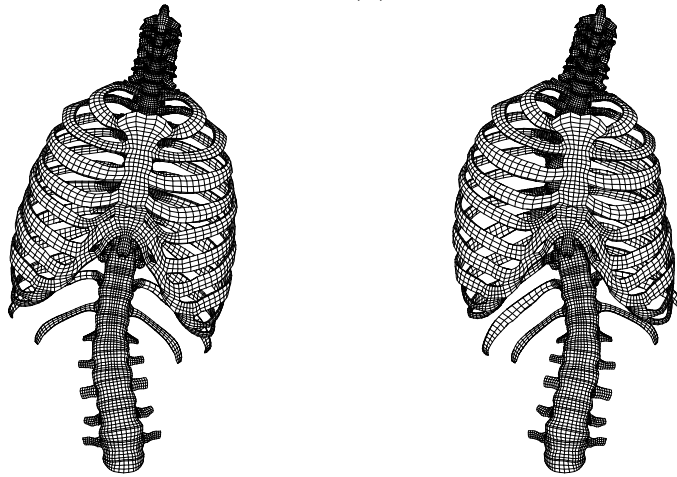
in Figure 4.8(a) and Figure 4.8(b), respectively. From the results in Figure 4.8(a), they found that when the growth pattern near to the central of the thoracic vertebrae around T7 or T8, a 4th buckling mode can occur easily, and these results indicated the etiologies of single and double curves are second and third side bending modes respectively [9] [92] [64]. These numerical results also demonstrated that the sensitivity function is high at the articular capsules of the the costotransverse joints, costovertebral joints, intervertebral joints and the intervertebral disks between T6 and T8 [93] [94] [95] [96].

Sasaoka [97] [82] [98] used mechanical models of spine by experiment to investigate the effect of the buckling hypothesis. With the comparison between the 4th buckling mode and the 2nd side bending natural vibration mode, variation of the frequency of the 2nd side bending mode was measured. His results verified the existence of the buckling phenomenon by the growth of the vertebral bodies. Moreover, two techniques named as morphing and fitting methods were developed to construct finite element models of spine for the individual patients [83] [99]. However, these results valid for infinitesimal deformation and is not applicable for the stability of post-buckling behavior.

Aoyama [100] [101] [10] [102] developed a program to analyze deformation histories caused by the growth of vertebral bodies considering the geometrical nonlinearity and investigated unstable phenomena. He assumed that growth represents generation of non-elastic bulk strain. Constraints at the cervical spine using a distributed spring were considered to exclude modes correctable by posture change. Using the developed program, deformation histories induced by the growth of vertebral bodies were analyzed. Deformation histories including unstable phenomena with side-bending modes similar to clinical curves were obtained. Loading factor vs. displacement at the front-center point on the eighth thoracic vertebra is shown in Figure 4.10 (a) to (c), and displacement of the center points in all vertebrae is shown in Figure 4.10 (d). The results indicated that the displacement in left direction of all vertebrae was less than 0.1mm. The magnitude of deformation was in the sub-millimeter order, which are too small for the etiology of idiopathic scoliosis.

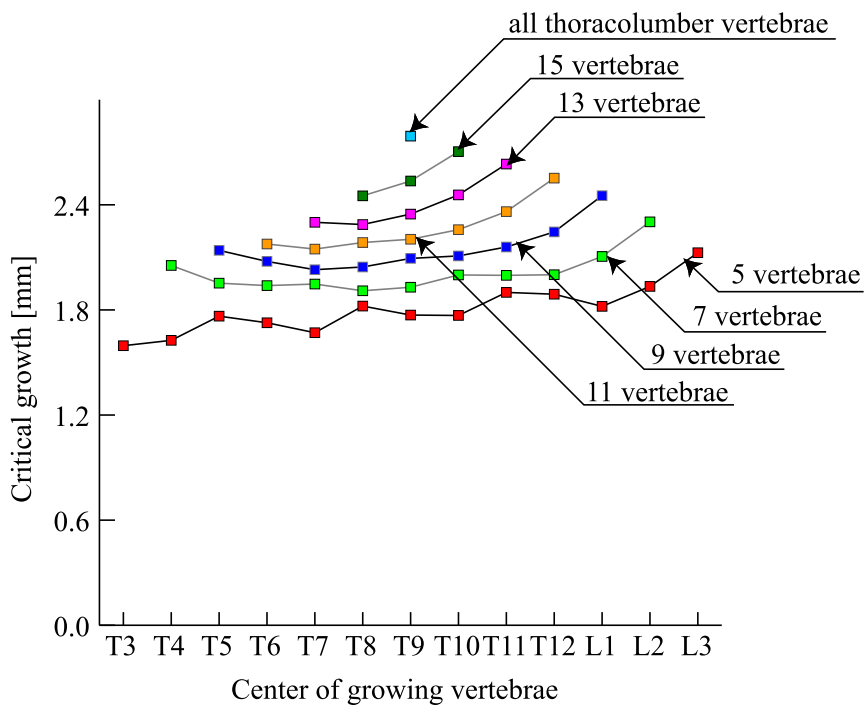


(a) 4th Mode by T1-L5 growth (b) 4th Mode by T1-T7 growth

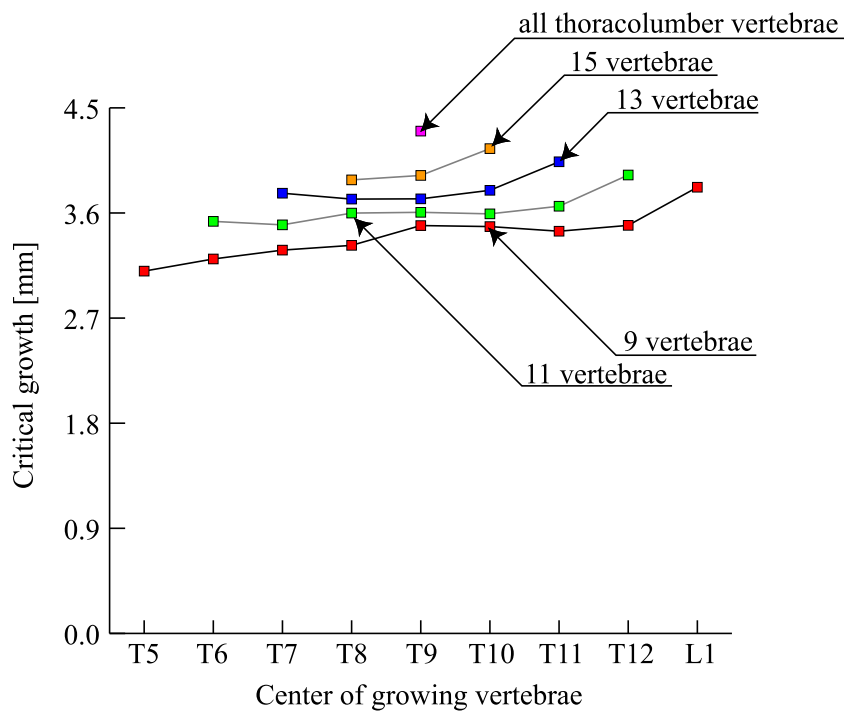


(c) 4th Mode by T11-L5 growth (d) 6th Mode by T1-L5 growth

Figure 4.7: Typical buckling modes [9]



(a) Critical growth with different growth region for 4th Modes [9]



(b) Critical growth with different growth region for 6th Modes [9]

Figure 4.8: Critical growth at generating buckling phenomena

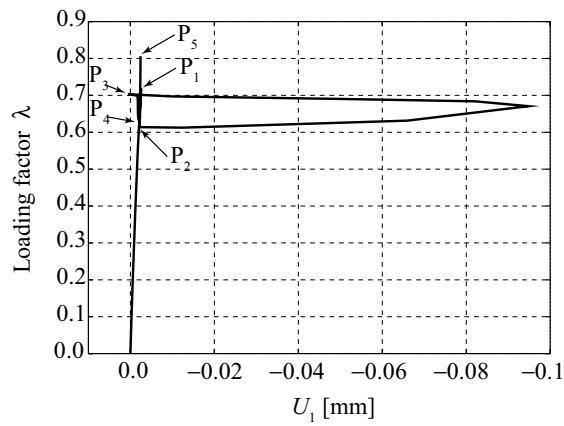
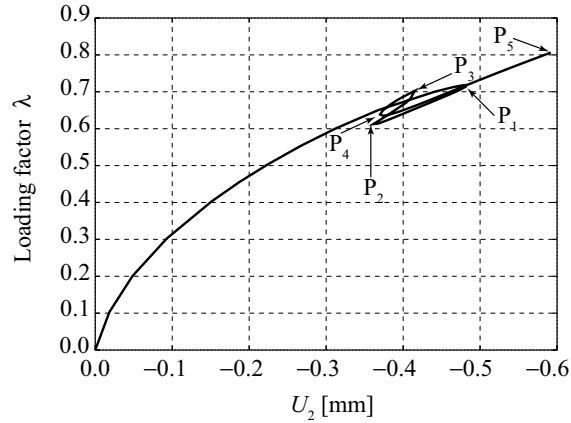
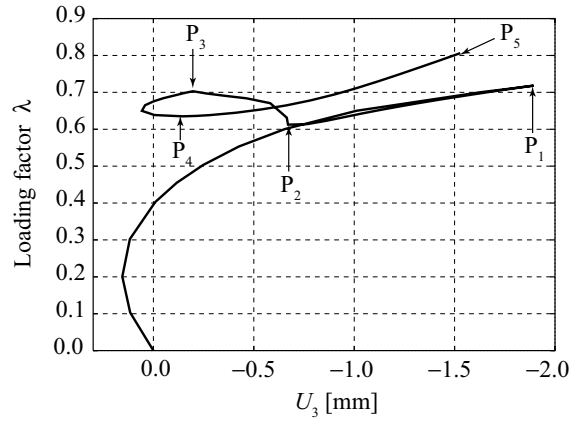
(a) Displacement in left direction U_1 of L8(b) Displacement in up direction U_2 of L8(c) Displacement in front direction U_3 of L8

Figure 4.9: Loading factor vs. displacement at the front-center point on the 8th thoracic vertebra [10].

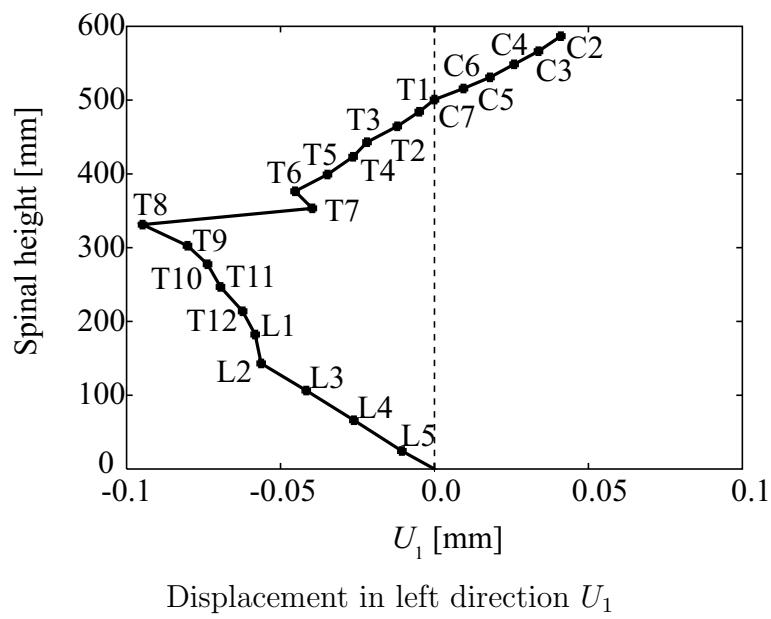


Figure 4.10: Displacement of the center points in all vertebrae [10].

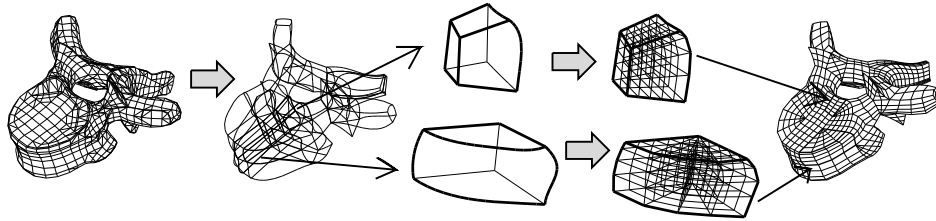
4.3 The manufacture of the spine model

Our research group has produced several finite element models of spine to investigate the mechanical etiology of idiopathic scoliosis based on the buckling hypothesis, as shown in Figure 4.5 and Figure 4.6 [75] [63] [77] [78] [79].

Commercial data of 3-dimensional spine surface from the Viewpoint DataLabs International, Inc. (Viewpoint Premire, catalog numbers of VP2886 and VP3611, Viewpoint Corporation, 498 7th Ave. Suite 1810, New York, NY 10018, USA) was used for the geometrical shapes. Our research group obtained the 3D spine surface data and used pre-post process function to make the finite element model by these data [96]. A solid modeler (I-DEAS Master Series2.1, SDRC, 2000 Eastman Drive, Miford, Ohio 45150-2789, USA) was used to construct the finite element meshes or combination in the respective subdomains. The procedure for devision of element meshes is shown as below. The procedure for manufacture of the 8th thoracic vertebrae is used as a sample in Figure 4.11.

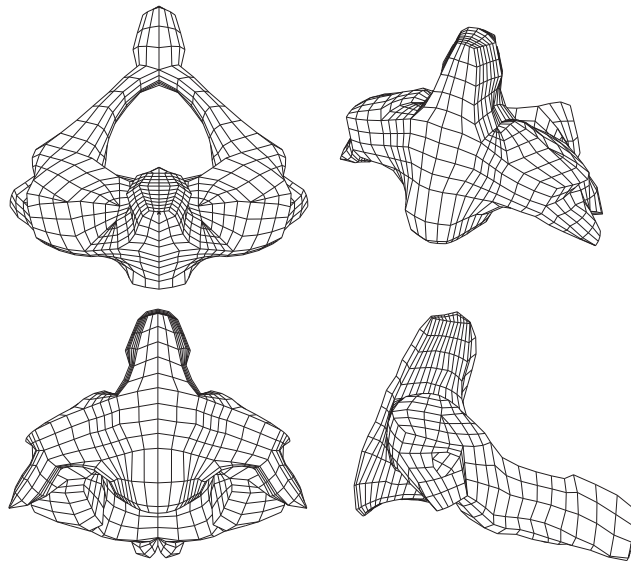
- (1) On the basic of commercially available facial data, the small aggregation region of hexahedrons and pentahedrons are determined at first, which are shown in Figure 4.11a and Figure 4.11b.
- (2) Inside each small aggregation region, the I-DEAS Master series version 2.1 was used to divide the finite element meshes or combination for each hexahedron and pentahedron. (Figure 4.11c).
- (3) The elements of intervertebral joints were added.
- (4) After the quality evaluations for each element were conducted, the elements which can not satisfy the criteria were modified manually.

After meshing process, the construction of the inner vertebrae is shown in the Figure 4.12 to 4.15.



(a) Facial data (b) Small aggregation region (c) Finite elements

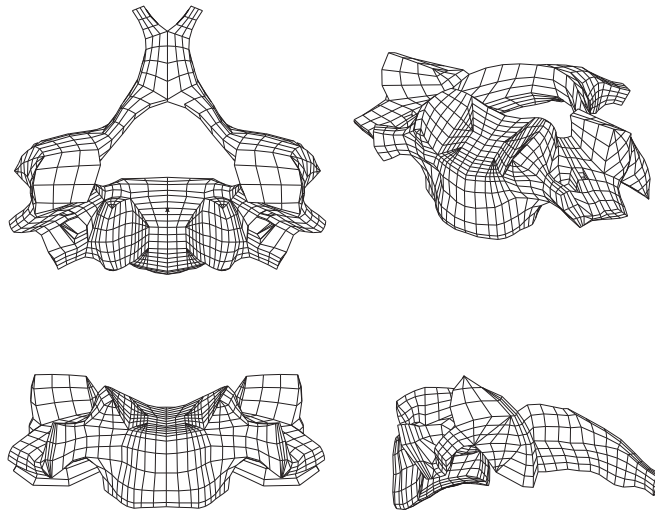
Figure 4.11: Finite element division for T8 thoracic vertebrae



- The number of nodes : 2,220

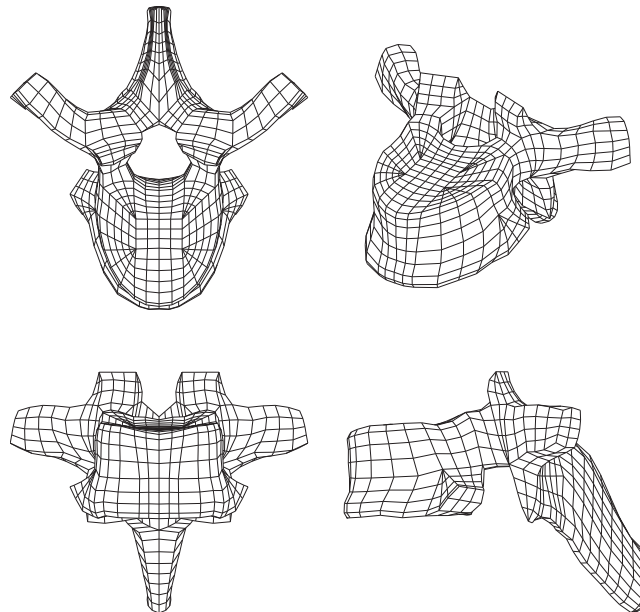
The number of elements : 1,752

Figure 4.12: The finite element model of the 2nd cervical vertebra



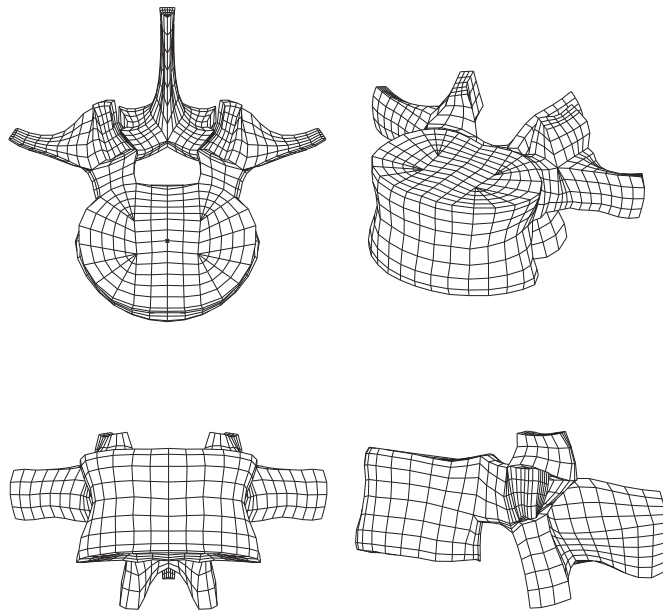
The number of nodes : 2,985
The number of elements : 2,312

Figure 4.13: The finite element model of the 5th cervical vertebra



The number of nodes : 3,084
The number of elements : 2,444

Figure 4.14: The finite element model of the 7th thoracic vertebra



The number of nodes : 2,509
The number of elements : 1,948

Figure 4.15: The finite element model of the 3rd lumbar vertebra

4.4 The finite element model of spine

The height of the finite element model of spine is around 610 [mm]. Since the normal human muscle system can not control the spinal deformity, the muscle system supporting the spinal column is ignored in this model. The aspect of the 9th and 10th thoracic vertebrae (T9 and T10) are shown in Figure 4.16. Each vertebra consists of cancellous bone on the inside of the vertebral body and cortical bone on the surface of the vertebral body, vertebral arch, transverse process, spinal process and articular process. The intervertebral disks consist of nucleus pulposus in the center of the disks (approximately 60% of radius) and annulus fibrosus in the exterior of the disks. Adjacent vertebrae were connected with intervertebral disks and articular capsules of intervertebral joints. Costal bones and vertebrae are connected with costotransverse joint and costovertebral joint. Sternum and the costal bones from first to tenth are combined with costal cartilage.

The spine model with rib cage consists of 84,587 nodes and 68,582 elements. The spine model without rib cage consists of 69,658 nodes and 59,356 elements. For this study, in order to get a better result, we changed part of the first-order elements (especially the principal structural part of vertebrae) to the reduced-integration, second-order elements. Therefore, after revolution of the elements, the new spine model without rib cage consists of 181,675 nodes and 59,356 elements. The spine model with rib cage and spine model without rib cage are shown in Figure 4.17 and Figure 4.18, respectively. Then, Abaqus 6.12 Edition (Abaqus, Inc.) was used to investigate the linear buckling analysis for the spine models.

4.4.1 The element

There are different types of solid elements for users to select in Abaqus. In this study, the C3D4H, C3D6H, C3D15H, C3D8RH, C3D20RH are used for the finite element model. The use rate for each element is shown in the Table 4.1. The description for the function of each type of element is stated as: the capital letter R means reduced integration, and the capital letter H indicates this element is hybrid element. In order to prevent from volumetric locking problems, the reduced inte-

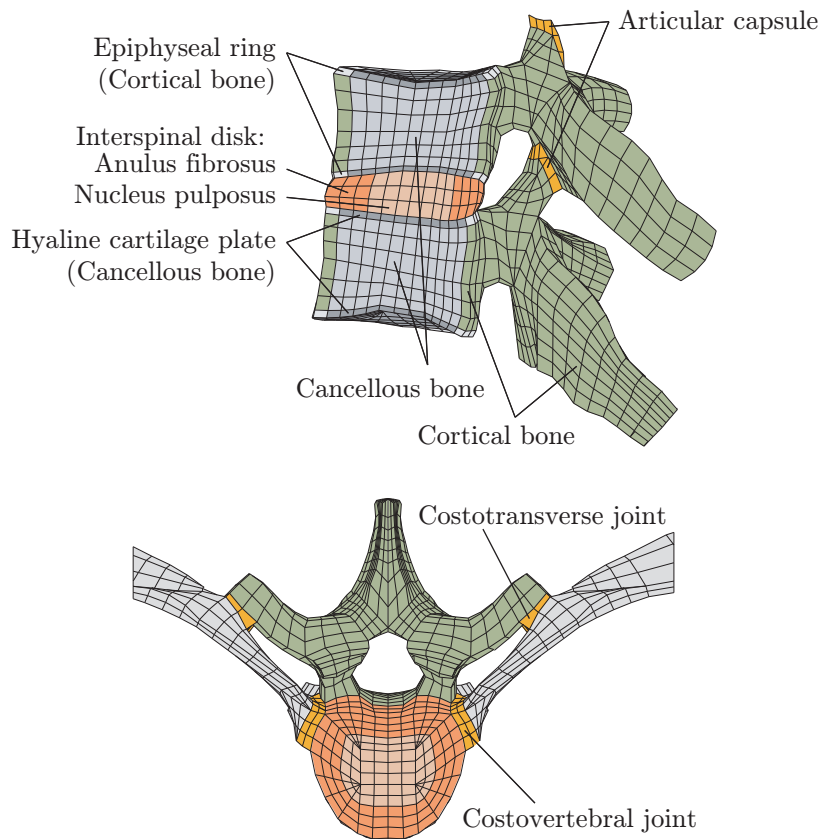
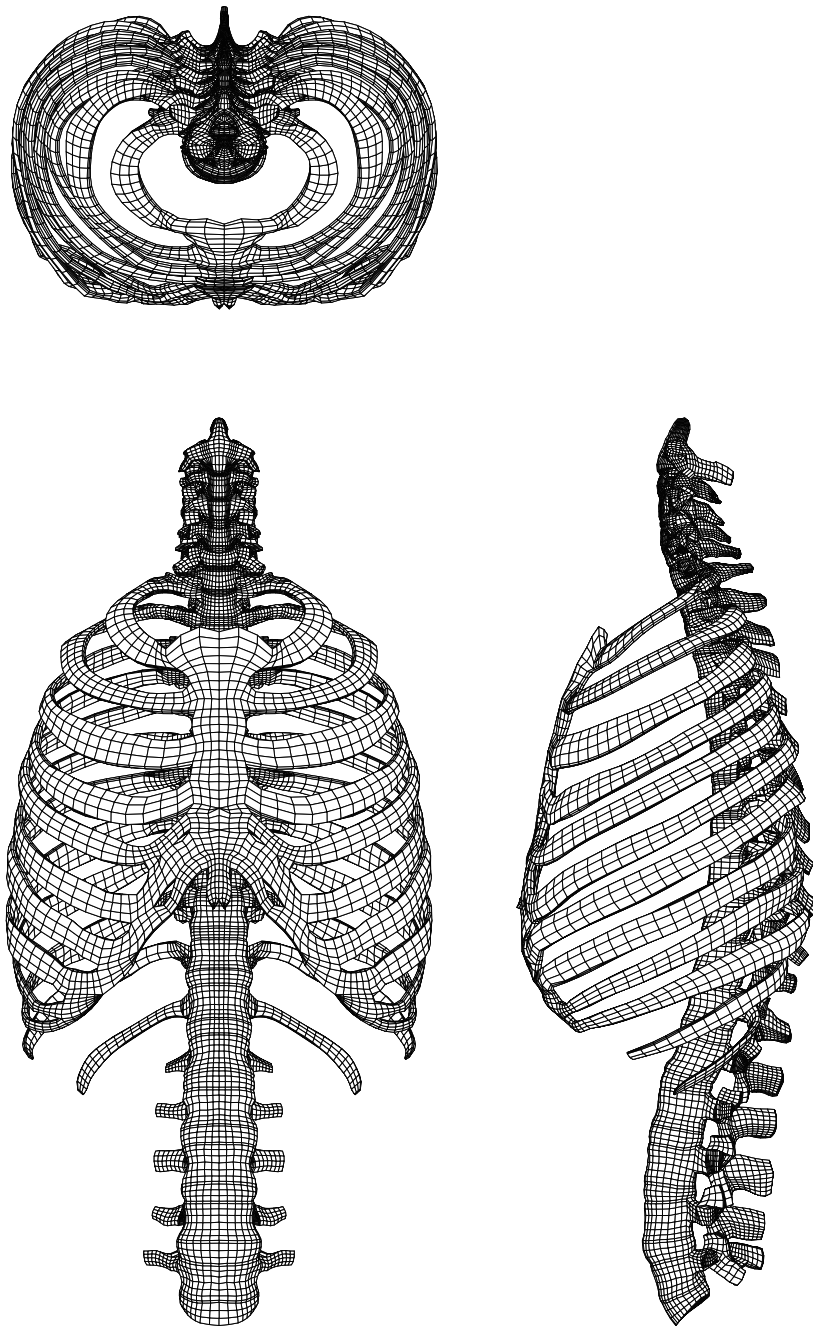


Figure 4.16: Finite element mesh for T9-T10

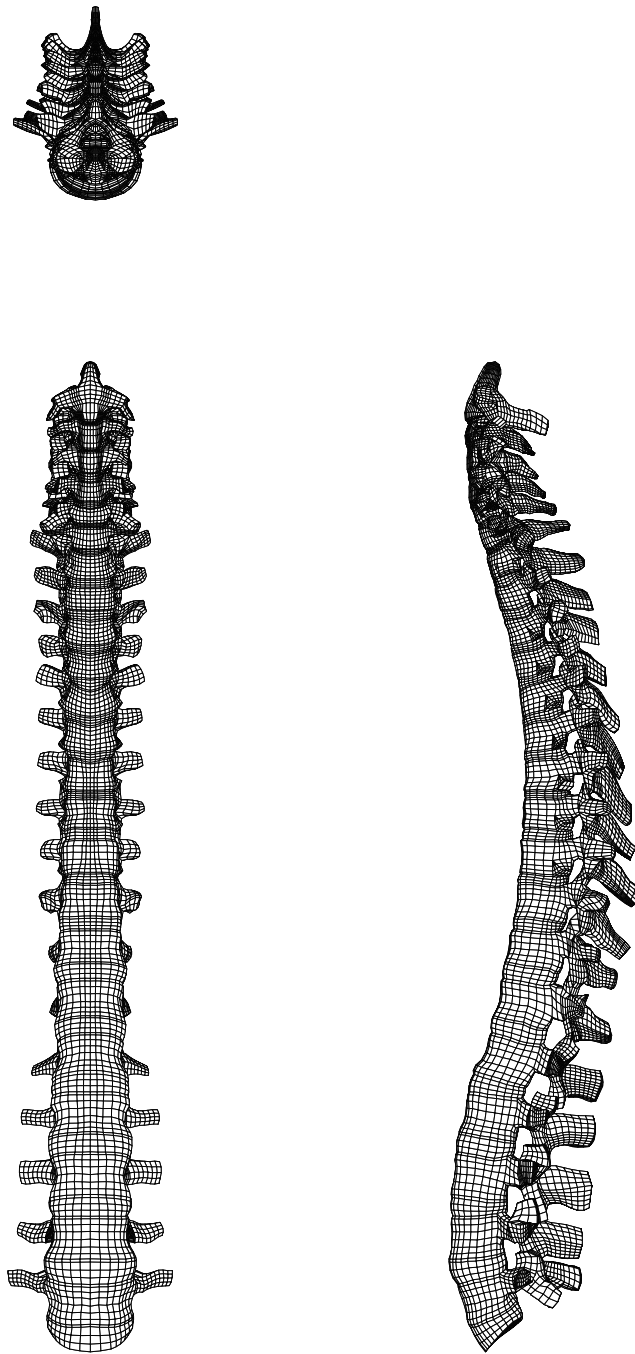
Table 4.1: Using rate for each type of element

Element	Name	Numer	Use rate
second-oder Hexahedron	C3D20RH	33357	56.2%
first-oder Hexahedron	C3D8RH	19083	32.2%
second-order Pentahedron	C3D15H	32	0.05%
first-order Pentahedron	C3D6H	6870	11.6%
first-order Tetrahedron	C3D4H	14	0.02%



The number of nodes : 84,587
The number of elements : 65,582

Figure 4.17: Finite element model of spine with rib cage



The number of nodes : 181,675
The number of elements : 59,356

Figure 4.18: Finite element model of spine without rib cage

gration hybrid elements are mostly used in the model. The qualities of elements are shown in Table 4.2.

In order to obtain the geometrically high precision, the spine model was also modified and adjusted through comparing the mechanical result from clinical spinal experiments. The material properties of cortical bones and cancellous bones in vertebrae, ribs and sternum were assumed using the data by Yamada [103], since their materials are so hard that their material properties are insensitive to the spinal deformations. By using the experimental results of bending ligamentous cadaver spines devoid of musculature by Lucas and Bresler [5], material properties of intervertebral joints were identified. Young's modulus of intervertebral disks was determined by comparing with the reactions of the thoracic and lumbar intervertebral disks to external forces of tension, compression and shearing in two directions and moments of bending in the two directions and torsion by Markolf [104]. By using the data of the deformation properties of costosternal and costovertebral articulations when loading to ribs obtained by Schultz et al [105], Young's modulus of costovertebral articulations and costotransverse articulations were identified. The material properties of the spinal finite element model is shown in Table 4.3.

4.4.2 The boundary conditions and growth region

For the boundary conditions, we still assumed that the sacrum is fixed, as shown in Figure 4.19.

The growth pattern of spine is marked in blue, as shown in the Figure 4.20. According to the previous study, the hyaline cartilage plates and the epiphyseal rings from T4 to T10, which are the easiest part to cause buckling phenomenon, is chosen to be the location of growth pattern [9]. The value of growth proportion α for the hyaline cartilage plates and the epiphyseal rings are shown in Table 4.4.

Table 4.2: Finite element qualities of the spine model

Elements	Warping	Distortion	Stretch
Cortical bone			
Cancellous bone	< 43°	> 0.6	> 0.05
Costal cartilage			
Nucleus pulposus			
Anulus fibrosus			
Articular	< 30°	> 0.65	> 0.1
Costovertebral joint			
Costotransverse joint			

Table 4.3: Material properties of each vertebra

	Young's modulus(MPa)	Shear modulus(MPa)
Cortical bone	17000	6540
Interior cortical bone	1000	385
Epiphyseal ring	1000	385
Cancellous bone	200	76.9
Hyaline cartilage plate	100	38.5
Nucleus pulposus	0.1	0.038
Anulus fibrosus	2.5	5.0
Cervical vertebrae	7.5	2.88
Thoracic vertebrae	7.5	2.88
Lumbar vertebrae	0.6	0.23
Sternum	17000	6540
Costal cartilage	500	19.2
Costovertebral joints	1.1	2.54

Poisson's ratio 0.3

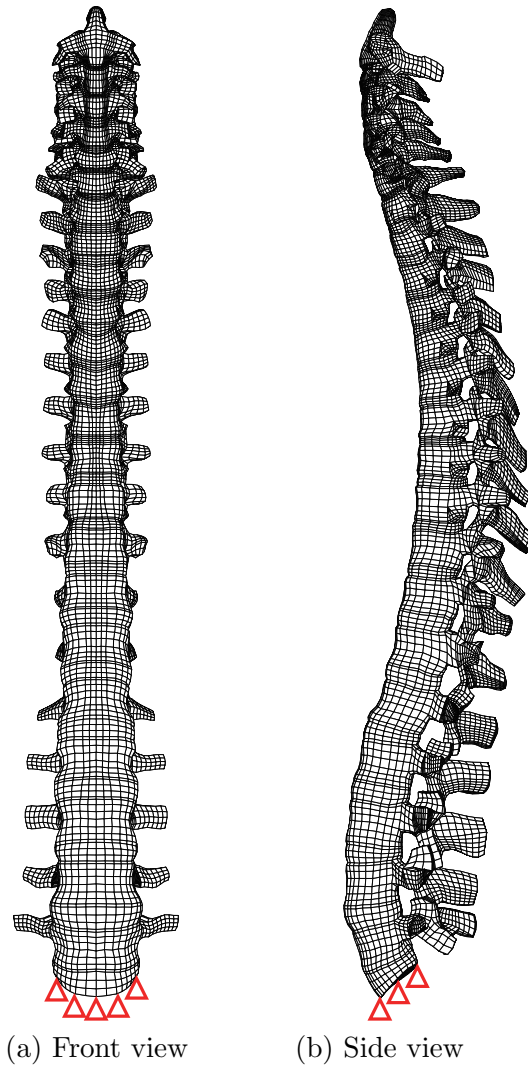


Figure 4.19: The boundary condition for the spine model

Table 4.4: Growth proportion α

Vertebrae	T4	T5	T6	T7	T8	T9	T10
$\alpha[-]$	0.02	0.04	0.06	0.08	0.06	0.04	0.02

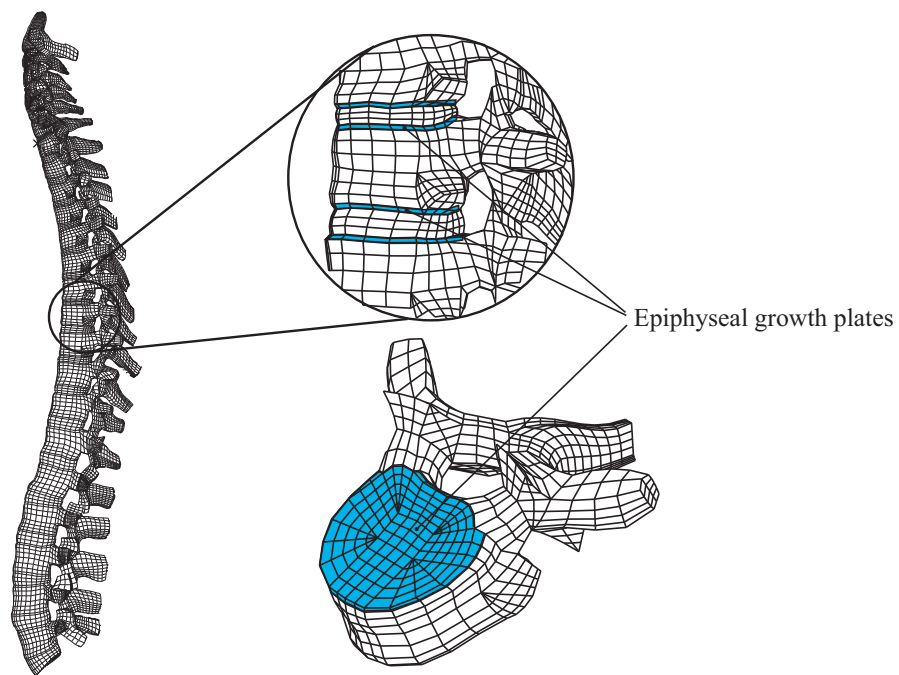


Figure 4.20: Growth region [11]

4.5 Results

After linear buckling analysis, lots of buckling modes were obtained, which are similar to the results from previous research. The shape of the 4th Mode as shown in Figure 4.24, accords with clinical single curve of main thoracic scoliosis. While the shape of the 7th Mode shown in Figure 4.27, resembles the clinical double curve of the thoracic scoliosis.

We also tried to investigate the difficulty for linear buckling analysis to occur with respect to various growth region $\Omega_G = \cup_{i \in \mathcal{V}} \Omega_{Gi}$. 5mm, 10mm, and 15mm of growth depth was added from the front to back of the vertebrae (from T4 to T10). Since the 4th Mode is similar to the clinical scoliotic shape, all the Load Proportionality Factor ζ_4 of the 4th Mode with respect to different growth depth were compared. The comparison results of the Load Proportionality Factor ζ_4 for each growth region is shown in Table 4.6. We found that when the growth depth is around 10mm, the smallest Load Proportionality Factor ζ_4 is recorded, which means the buckling phenomenon occurs most easily. This also accords with the results we obtained with simple plate models in Chapter 3.

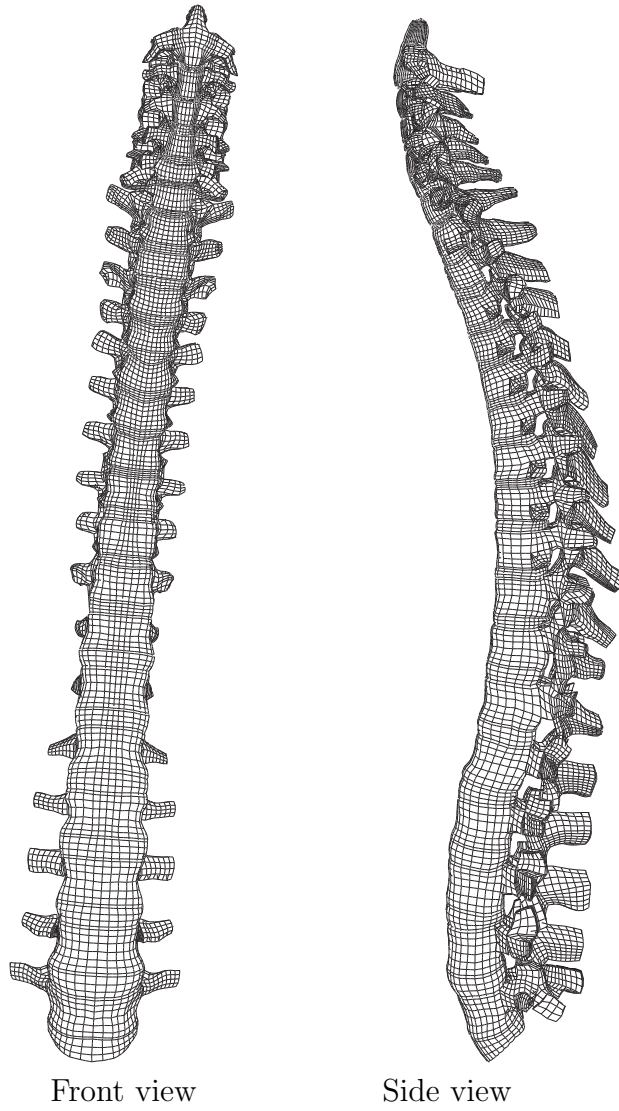


Figure 4.21: The 1st Mode of spine model ($\zeta_1 = 1.046$)

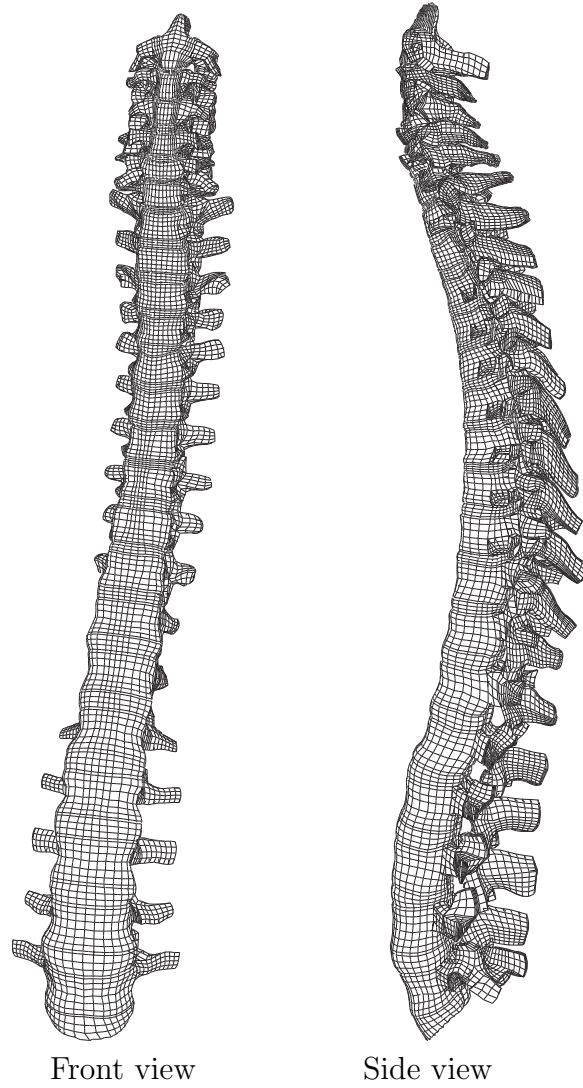


Figure 4.22: The 2nd Mode of spine model ($\zeta_2 = 2.272$)

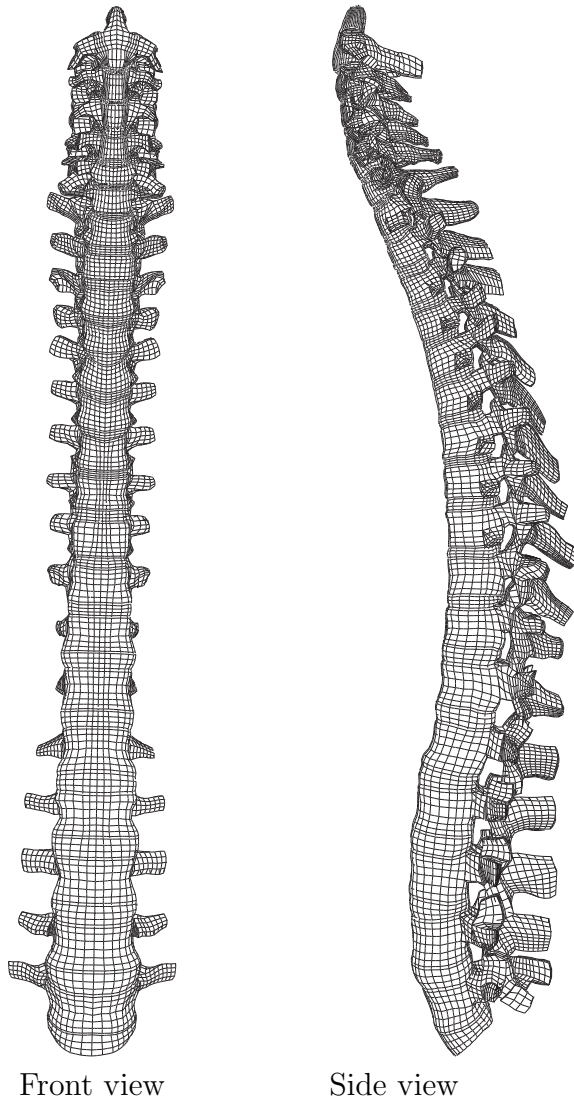


Figure 4.23: The 3rd Mode of spine model ($\zeta_3 = 2.521$)

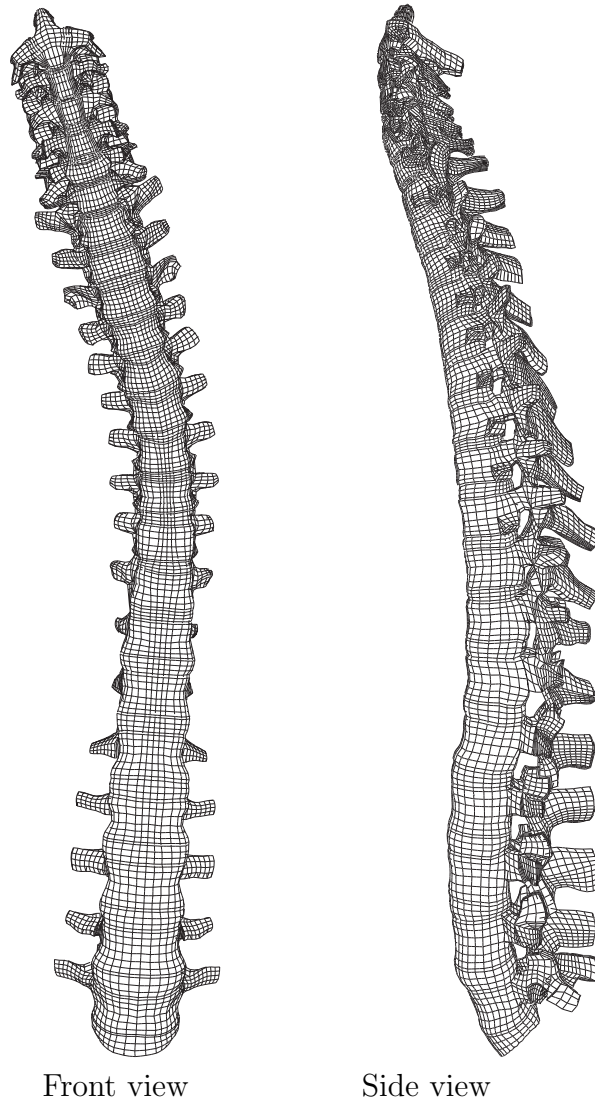


Figure 4.24: The 4th Mode of spine model ($\zeta_4 = 5.203$)

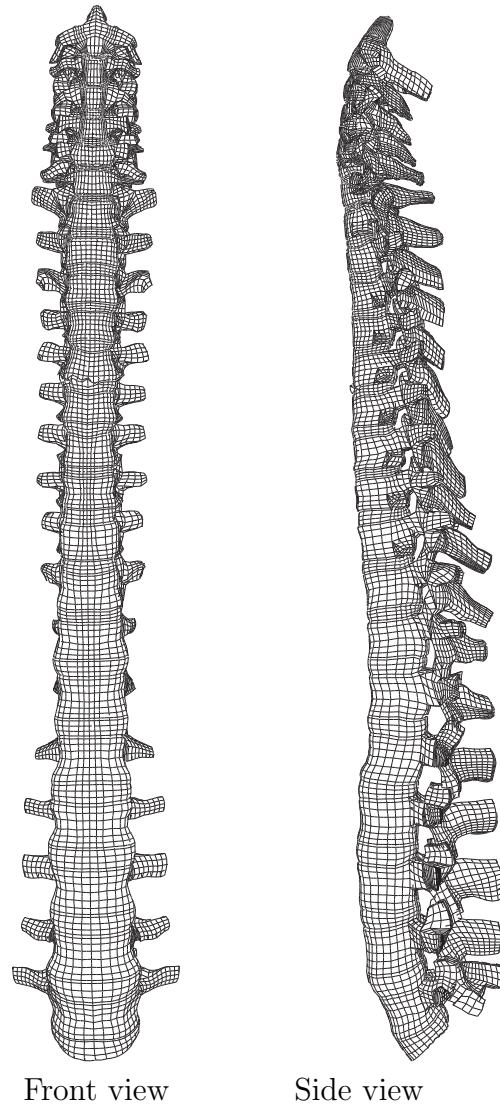


Figure 4.25: The 5th Mode of spine model ($\zeta_5 = 5.936$)

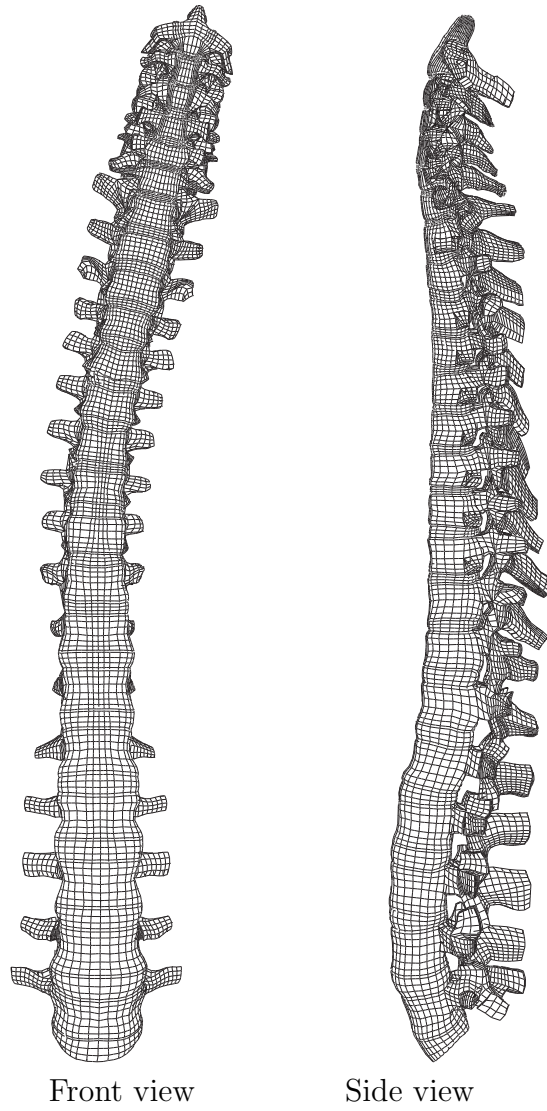


Figure 4.26: The 6th Mode of spine model ($\zeta_6 = 7.242$)

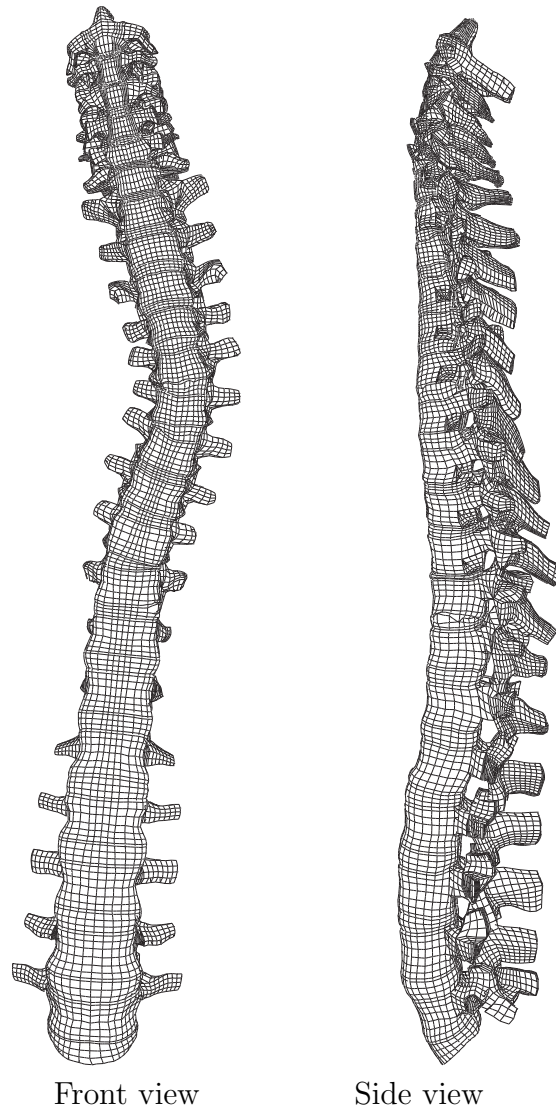


Figure 4.27: The 7th Mode of spine model ($\zeta_7 = 13.564$)

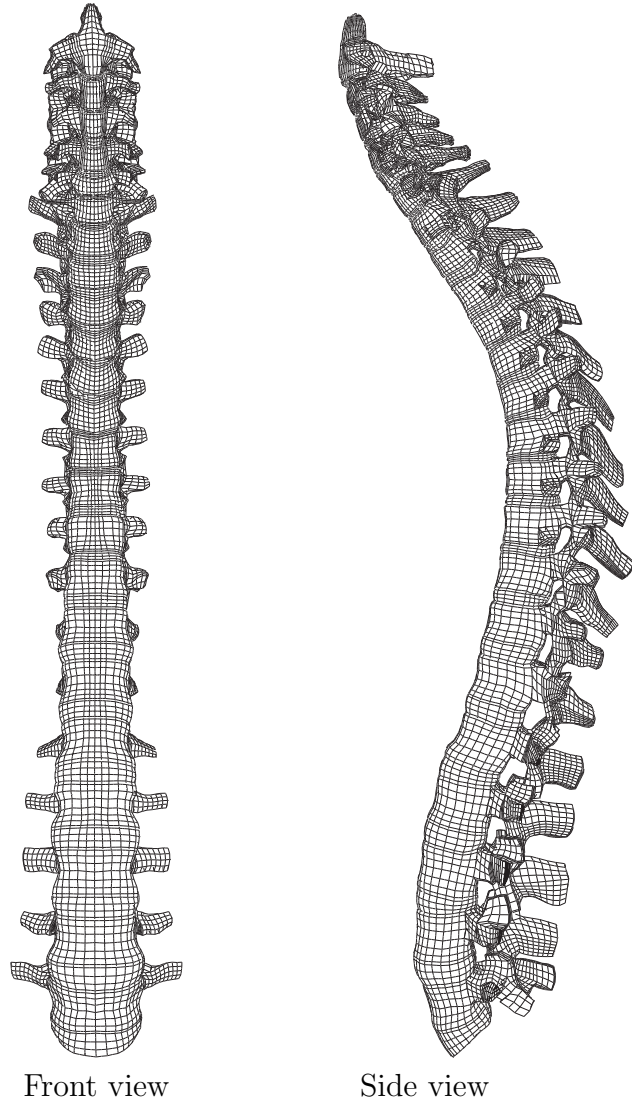


Figure 4.28: The 8th Mode of spine model ($\zeta_8 = 15.094$)

4.6 Discussion

Table 4.5: Growth rate of vertebrae for normal girls

	Period		
	7-8 year olds	8-9 year olds	9-10 year olds
Thoracic vertebrae	5.3%	7.0%	4.5%
Thoracic interspinal disk	3.8%	0.8%	-5.1%
Lumbar vertebrae	3.9%	4.4%	2.6%
Lumbar interspinal disk	9.8%	7.9%	6.8%

Table 4.6: Load Proportionality Factor at the 4th buckling ζ_4 with respect to depth of growth domain Ω_G

Depth of growth domain (mm)	ζ_4
5	4.1408
10	3.555
15	4.0477

In the linear buckling analysis, the value of growth proportion α for the hyaline cartilage plates and the epiphyseal rings is shown in Table 4.4. The average value for the growth proportion α in Table 4.4 is 0.0457. The Load Proportionality Factor at the 4th buckling ζ_4 is 5.203. Therefore, the average value of the growth amount of the hyaline cartilage plates and the epiphyseal rings can be calculated as $0.0457 \times 5.203 \approx 0.2377$. The hyaline cartilage plates and the epiphyseal rings occupy 12% of the thickness of the interspinal disk. Therefore, the average value of growth amount for the vertebrae from T4 to T10 can be calculated as $0.2377 \times 0.12 \approx 0.0285$.

Nehme [106] investigated the growth rate for the spine of the normal girls, and the results of growth rate of each vertebra are shown in Table 4.5. For the thoracic vertebrae of 8-9 year olds normal girls, the growth rate for one year is around 7.0%. Thus the growth rate for one month is $0.070 \div 12 \approx 0.0058$. Thus the growth period can

be estimated as $0.0285 \div 0.0058 \approx 4.9$. This means it takes nearly 4.9 months for the spine to get buckled as the 4th buckling mode in this analysis.

4.7 Conclusion

In this chapter, in order to investigate the buckling hypothesis, the finite element model of spine is used to complete the linear buckling analysis. New finite element model of spine which is more exact than the previous model is introduced. After the linear buckling analysis, the 4th buckling mode which is similar to the clinical scoliotic curves is obtained. Then we tried to investigate the difficulty of the spine model to get buckled with respect to different growth regions. When the growth depth is around 10 mm, the smallest Load Proportionality Factor ζ_4 is recorded, which accords the results of the simple plate models analysis in Chapter 2. After all calculations, we can estimate that 4.9 months are required for the spine to deform as similar shape of 4th buckling mode for the case of patient from 8-9 year olds.

Chapter 5

Nonlinear post-buckling analysis for spine model

In this chapter, we conducted post-buckling simulations caused by the growth of vertebral bodies by considering the geometrical nonlinearity using the spine models with full width and half width. In Section 5.1 and Section 5.2, the 4th buckling mode of the normal spine model and the spine model with half width was chosen to verify the nonlinear post-buckling phenomenon. Then, the existence of the non-linear buckling phenomena and stable deformation during buckling process were examined in the spine model with half width in Section 5.3.

5.1 The normal model

The growth region $\Omega_G = \cup_{i \in \mathcal{V}} \Omega_{Gi}$ is the hyaline cartilage plates and the epiphyseal rings from T4 to T10 for the nonlinear post-buckling analysis, which is still same as the linear buckling analysis discussed in Chapter 4. The sacrum is fixed as the boundary conditions as shown in Figure 5.1.

In order to study the nonlinear post-buckling analysis, the initial imperfection was introduced to the 4th Mode which is result of the linear buckling analysis in Chapter 4, as shown in Figure 5.2. The value of imperfection as 15% was applied to the 4th Mode, and the result of nonlinear post-buckling analysis is shown in Figure 5.3.

After the nonlinear simulation, the result of the relationship between the load proportionality factor and Arc-length is shown in Figure 5.4, which indicates the simulation stopped when the Arc-length is just around 28.9. Comparing with the original model, little deformation can be observed after the simulation as shown in Figure 5.3. From these results, we can claim that no occurrence of the nonlinear post-buckling phenomenon in this simulation. Even though several different value of imperfection were used, similar results were obtained and these results strengthened our claim that no nonlinear post-buckling occur for this model.

5.2 The narrow model

5.2.1 The spine model with half width

The finite element model of spine that we used in the analysis consists of the data of male adults. However, the idiopathic scoliosis are found more frequently in young girls during adolescence. Comparing with male adults, the spine of girls during adolescence is more soft, easier to be bend and narrower in size. Therefore, in order to suit the condition of adolescence girls, we shrank the width of the spine model to half of its original width, while the other conditions and properties are still maintained. The spine model with half width is shown in Figure 5.5. The hyaline cartilage plates and the epiphyseal rings from T4 to T10 is still set to be the growth region $\Omega_G = \cup_{i \in \nu} \Omega_{Gi}$.

The results of linear buckling analysis of the spine model with half width is shown in Figure 5.6. The 4th Mode which is similar to the clinical scoliotic shape is still chose as the buckling mode for nonlinear post-buckling analysis.

After applying the value of imperfection as 15% to the 4th Mode of the linear buckling analysis, the result of nonlinear post-buckling analysis is shown in the Figure 5.7. The relationship between the load proportionality factor and Arc-length is shown in Figure 5.8. From these results, the nonlinear analysis could not continue and finished with small Arc-length. The results indicated that still no nonlinear post-buckling phenomenon occurred for this model.

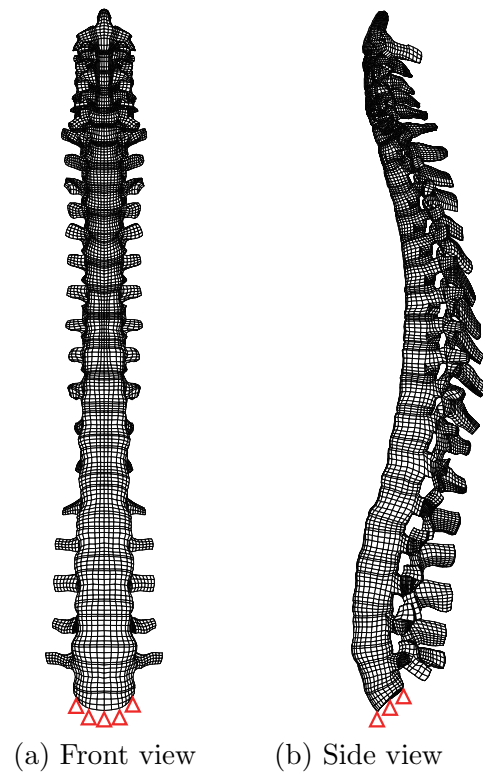


Figure 5.1: The boundary condition for the spine model

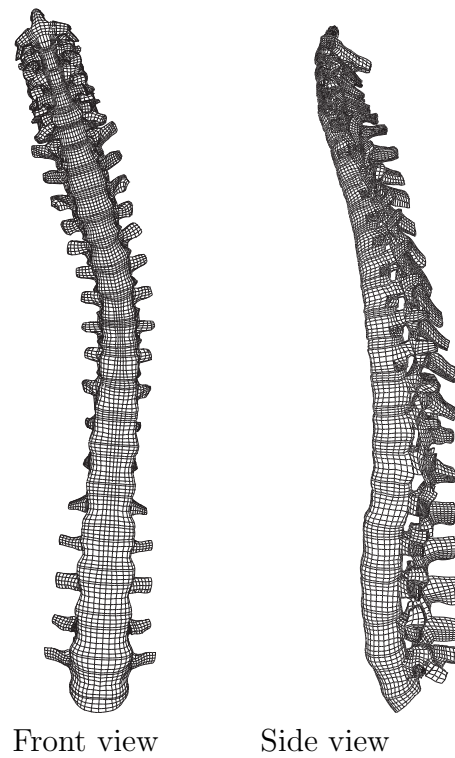


Figure 5.2: The 4th linear mode of spine model ($\zeta_4 = 5.203$)

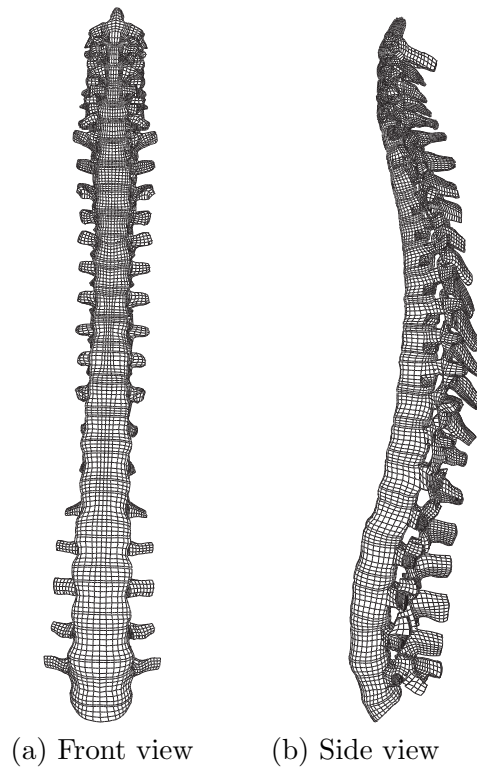


Figure 5.3: The nonlinear post-buckling analysis for the 4th Mode ($\lambda = 28.89$)

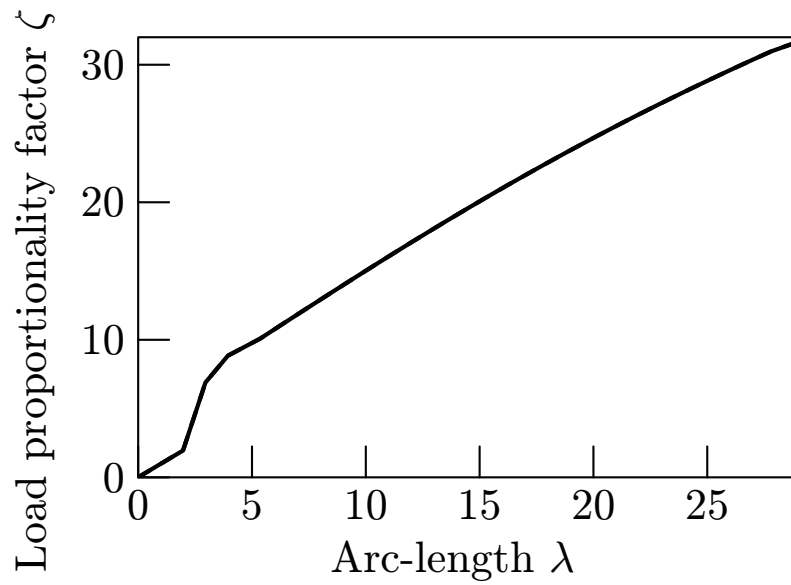


Figure 5.4: History of load proportionality factor for the spine model

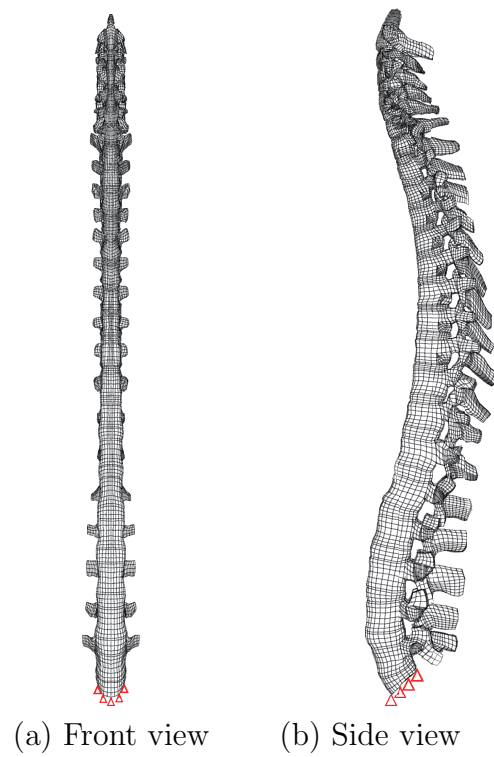


Figure 5.5: The boundary condition for the half width spine model

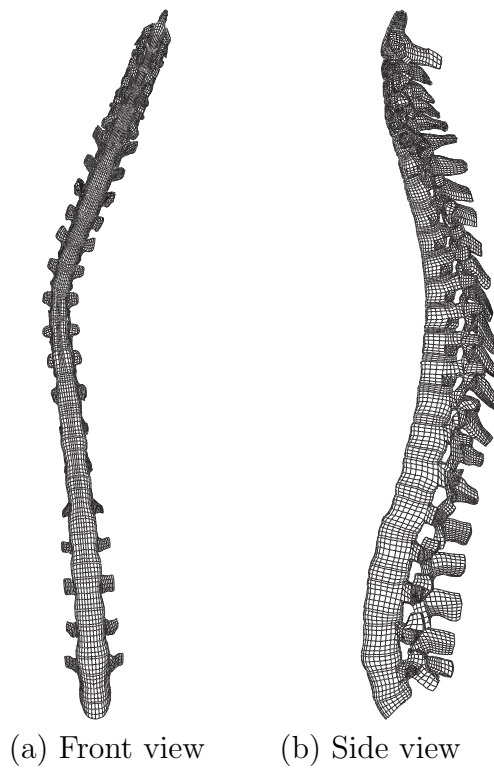


Figure 5.6: The 4th linear buckling mode of half width spine model ($\zeta = 12.701$)

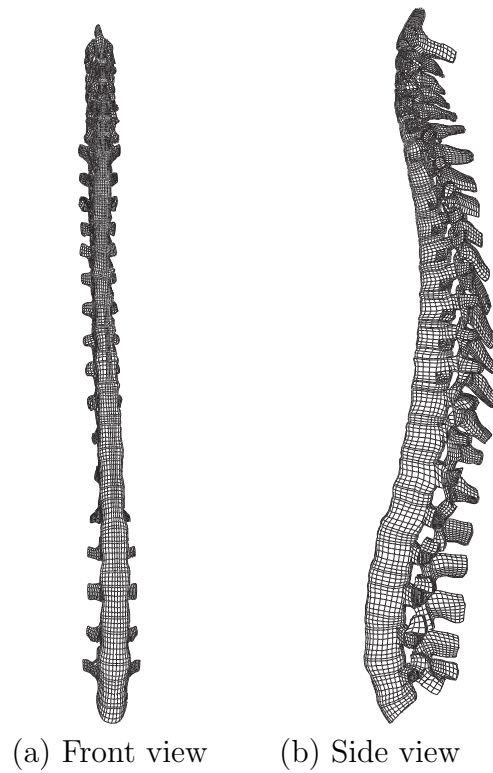


Figure 5.7: Nonlinear growth deformations of half width spine models with initial imperfections of the 4th buckling mode ($\lambda = 72.95$)

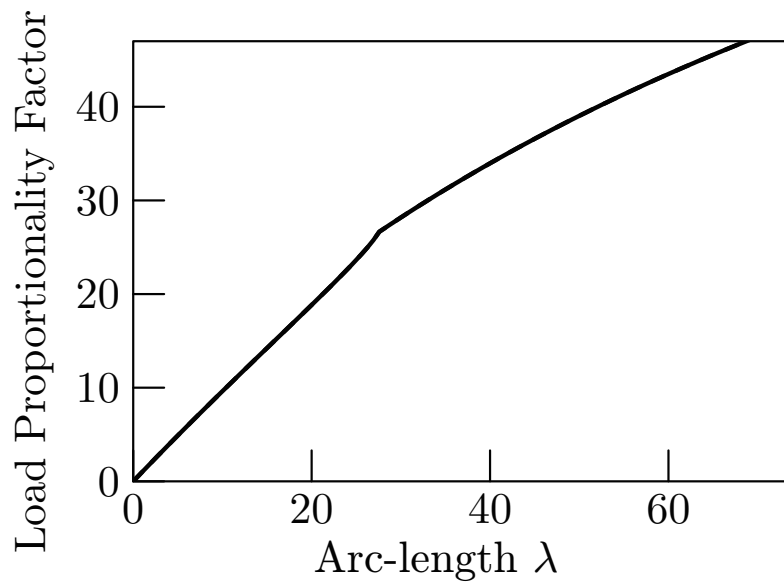


Figure 5.8: History of load proportionality factor for the half width spine model

5.2.2 The new boundary condition

By considering muscles have the function to control the position of spine, we fixed the nodes at the center of front boundary of C7 around the neck. Moreover, the fixed sacrum is still maintained. The new boundary condition of the spine model with half width is shown in Figure 5.9.

After introducing the value of imperfection as 15% to the 4th Mode of the linear buckling analysis, the result of nonlinear post-buckling analysis under the new boundary condition is shown in the Figure 5.10. The relationship between the load proportionality factor and Arc-length is shown in Figure 5.11. From these results, when the Arc-length passed 32, the load proportionality factor decreased after the maximum value, which indicated that, the existence of the non-linear buckling phenomena can be confirmed in the spine model with half width under the new boundary we used. Moreover, when the analysis finished, the load proportionality factor is around 90, the Arc-length is around -30, and the deformation of spine model at this moment is shown in Figure 5.10. However, after measuring, the Cobb angle α is only 7.5° , which is too small comparing with the clinical scoliotic curves.

5.3 Discussion

From the results in Figure 5.11, we can see, the turning point of the load proportionality factor occurred when the Arc-length is around 32, indicated that the unstable nonlinear post-buckling phenomenon occurred in this analysis. At this moment, the load proportionality factor is $\zeta = 25$, which means, when the growth of vertebral bodies was given by occurring in the sub-domain Ω_G , with 25% of the bulk strain ($0.01 \times \zeta = 0.25$), which caused the unstable post-buckling phenomenon occurred in this model. However, when the Arc-length is around 90, the value of the load proportionality factor is nearly -30. This impractical value also indicated the buckling hypothesis can be the onset in the idiopathic scoliosis, but can not be the reason for developing mechanism of idiopathic scoliosis.

From these results, the pathogenesis of the onset in the idiopathic

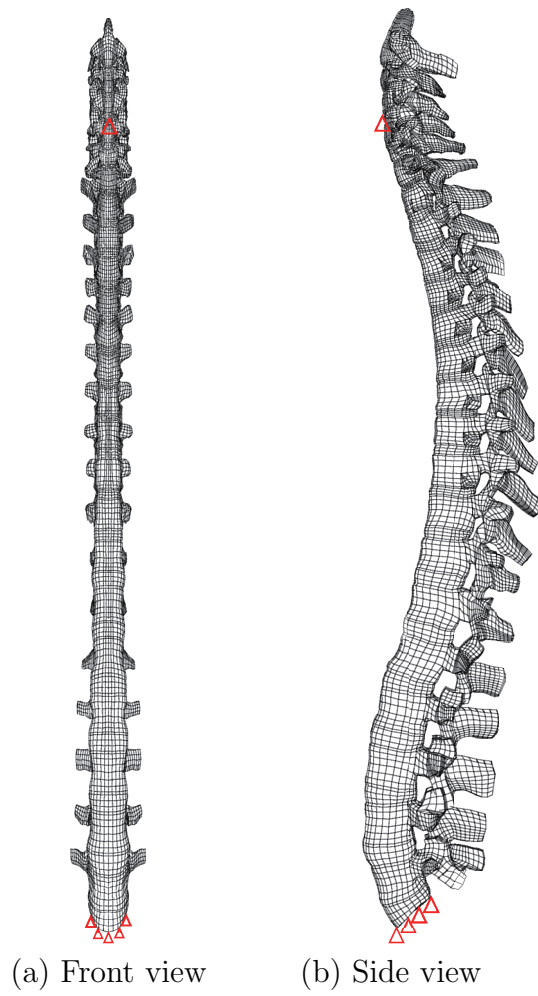


Figure 5.9: The new boundary condition for the half width spine model

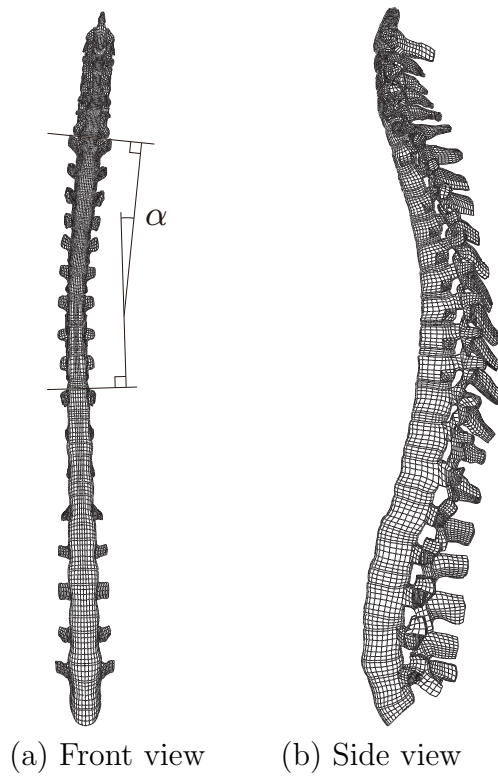


Figure 5.10: Nonlinear growth deformations of half width spine models with initial imperfections of the 4th buckling mode ($\lambda = 90.1$, Cobb angle $\alpha = 7.5^\circ$)

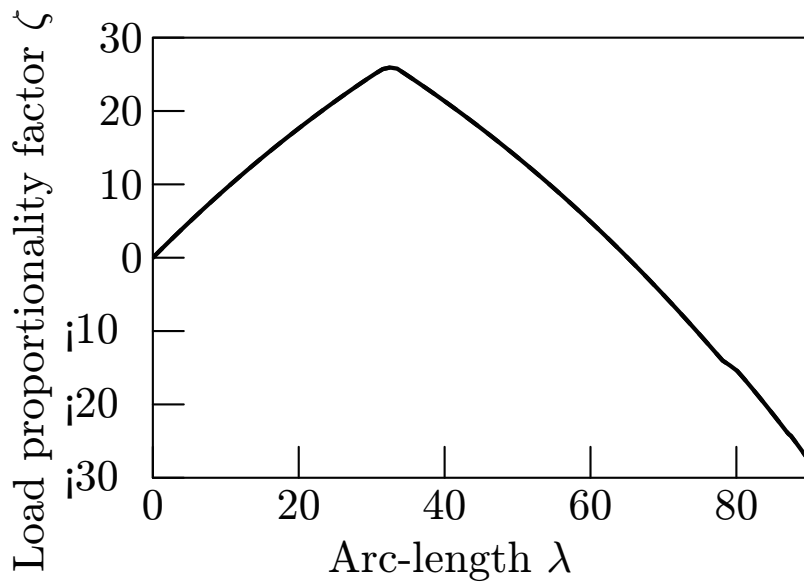


Figure 5.11: History of load proportionality factor for the half width spine model

scoliosis can be explained by the buckling hypothesis. Even though nonlinear post-buckling phenomenon occurred in this analysis, the magnitudes of the post-buckling deformations are too small to explain the pathogenesis of the severe deformity observed in patients of idiopathic scoliosis.

The reasons why the post-buckling analysis ended with small Arc-length is discussed as following. By referring to the error history from Abaqus/Standard, the first-order triangular elements seem to be the problem occurred at the end of the analysis. When the analysis finished, the stature of the elements are shown in the Figure 5.12. As a result, the first-order triangular elements seem too easy to be deformed.

First-order triangular and tetrahedral elements should be avoided as much as possible in stress analysis problems [107]. These elements are too stiff and exhibit slow convergence with mesh refinement. If the use of first-order elements are unavoidable, better mesh with sufficient accuracy should be applied in the spine models.

For the future work, the innovation and improvement of the first-order elements of spine model should be continued.

5.4 Conclusion

Results in this chapter indicate that, the existence of the non-linear buckling phenomena can be observed and measured by using the spine model with half width. Moreover, after the nonlinear post-buckling phenomena, unstable deformations were obtained in the spine model with half width. Therefore, the pathogenesis of the onset in the idiopathic scoliosis can be explained by the buckling hypothesis. However, the magnitudes of the post-buckling deformations are too small to explain the pathogenesis of the severe deformity observed in patients of idiopathic scoliosis.

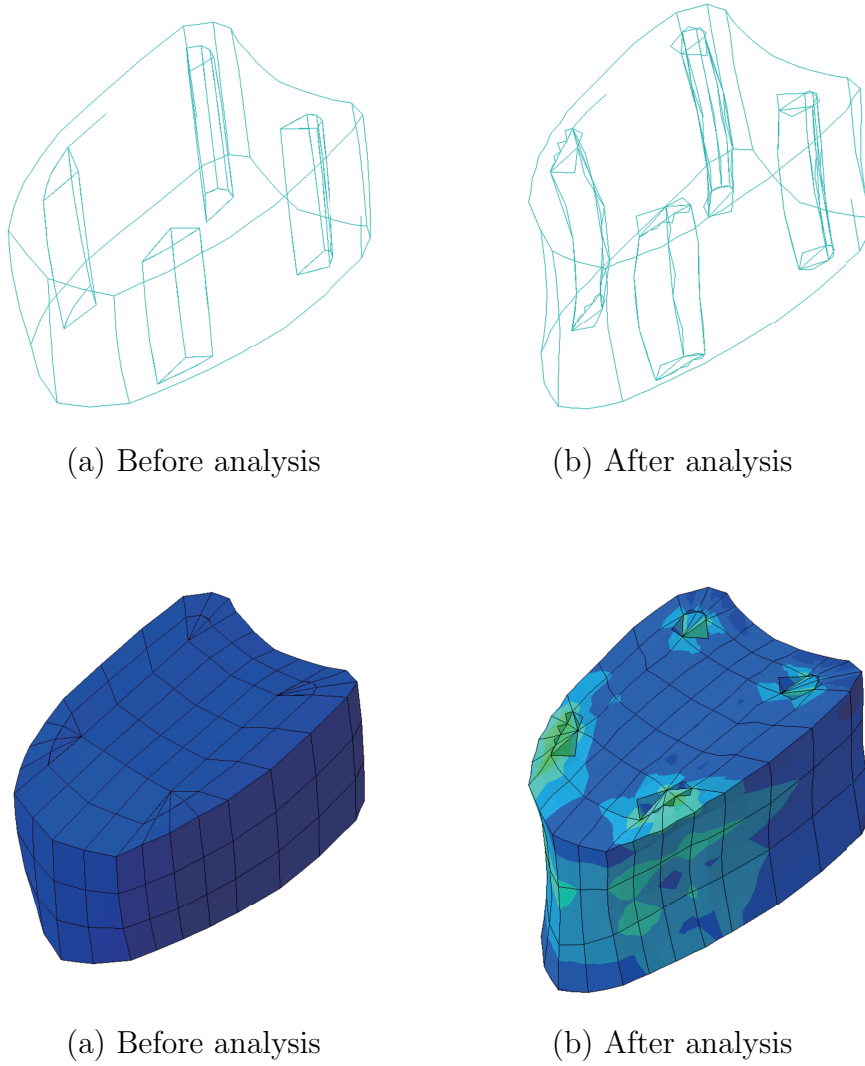


Figure 5.12: The 4th linear buckling mode of half width spine model ($\zeta = 12.701$)

Chapter 6

Bone remodeling

In this chapter, the influence of bone remodeling on the buckling spine is discussed. We used heat deformation analysis by FEM to examine the bone remodeling etiology. Firstly, the Fung's bone remodeling hypothesis is introduced, and the condition for bone remodeling simulation is described. Then, we conducted bone formation analysis and bone resorption analysis to investigate the developing mechanism of the severe deformity observed in patients of idiopathic scoliosis.

6.1 Bone remodeling

After many theoretical and experimental studies, Fung [108] proposed a hypothesis on the growth of bone. He claimed that the remodeling of blood vessel inside bone involving growth or resorption of cells and extracellular materials has obvious relationship with the stress in the vessel. He recognized that active or passive mechanism depends in strain in the cell membranes can transport of matter through cell membranes. The strain decides the granular-to-brous transformation of actin molecules. Chemical reaction rate depends in pressure, stress and strain. Hence, the stress and strain in a manner shown in the Figure 6.1. The meaning of the equilibrium states **a**, **b**, **c** is as described as below. The point **a** means an increase of stress cause growth, a decrease of stress causes resorption. The point **b** or **c** means a decrease of stress causes growth, an increase causes resorption.

Fung pointed out an equation to describe the growth rate as below,

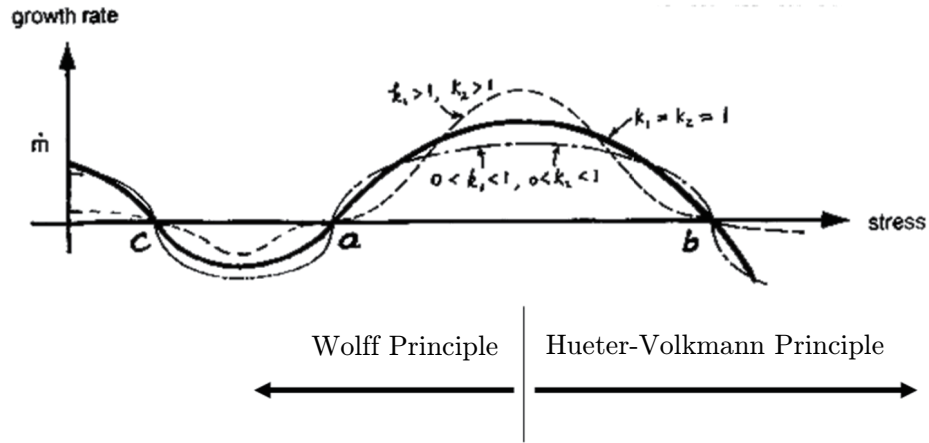


Figure 6.1: Fung Principle

$$m = C(s - a)^{k_1}(b - s)^{k_2}(c - s)^{k_3} \quad (6.1.1)$$

where, the m is the growth rate, s is the stress, C , a , b , c , k_1 , k_2 , k_3 are constants. If the k_1 , k_2 , k_3 is small than 1, the slope of the curve is steep. If the k_1 , k_2 , k_3 is bigger than 1, the slope of the curve is flat. And the point a means homeostatic condition of blood vessel wall at normal blood pressure. Moreover, when the blood pressure increased, the growth rate behaves like the right part of point a . When the s reaches the value between a and b or c and 0, the bone tissue grows. When the s falls between a and s , or exceeds b , the resorption of bone occurs.

At simple level, bone remodeling is under controlled by the Wolff' principle, which is proposed by Dr. Wolff in the 19th century [109]. Enormous stress or force will cause bone to grow, build, adapt, transform, and remodel. The intermittent increased stress will stimulate bone formation, and the reduced intermittent stress will cause bone resorption.

In 1862, Richard von Volkmann restated his own theory about bone growth, and quoted Carl Hueter's work, and then the Hueter-Volkmann principle, an important orthopedic concept concerning bone

growth, was created [110]. The Hueter-Volkmann principle can be summarized as below: for the immature bone growth, increased pressure inhibits growth; decreased pressure accelerates growth.

On the other hand, the Hueter-Volkmann principle is different from that stated by the Wolff' principle. The Wolff' principle relates mainly to the alterations inside the internal construction of the bone. The greater stress results in greater bone density and apposition. However, the increased compression reduces the longitudinal growth, accords to the Hueter-Volkmann principle.

In 1966, Frost proposed the concept of a mechanical feedback system for modeling and remodeling of bone [111] [112] [113]. He invented the BMU, which means the basic multicellular unit of a bone. The activity of these unit of cells accomplish bone remodeling, occurring after skeletal maturity inside the internal structure, caused by the dynamic components of stress. When bone does not have enough strain, the bone resorption occurs. When bone has ideal strain, the bone will keep organized and mineralized [114] [115]. Strain has the function to control the cellular reaction of bone.

The theory of bone remodeling was then developed by other researchers. As a living tissue, low stress conditions results in bone resorption, whereas high stress conditions make the bone growing [116] [117]. Cowin [118] used model bone with a normal adaptive process to demonstrate the strain can control mass deposition or resorption process, which result in bone remodeling. Neuman [119] claimed an osteon ages its hydroxyapatite crystals become dehydrated and lose ability to remain interact with flood plasma. At this time, an old dehydrated osteon will be resorbed to maintain the physiological function of bone chemically.

6.2 Remodeling analysis

We simulated the bone modeling (bone formation and resorption) analysis as heat deformation caused by changes in temperature [120] [121] [122]. Bone modeling increased and decreased the volume of the whole vertebral bodies from T4 to T10. For the boundary conditions, we still assumed the sacrum is fixed. However, by considering

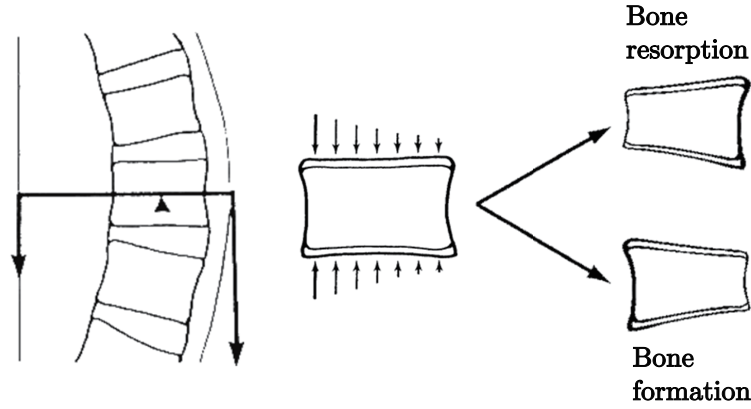


Figure 6.2: Bone remodeling

the function of muscles, we also fixed the nodes at the center of front boundary of C7 around the neck. The boundary condition is as same as the nonlinear post-buckling analysis for the half width spine model in Chapter 5.2.2, as shown in Figure 6.5.

The strain distribution occurring after the nonlinear post-buckling analysis from half width spine model is shown in Figure 6.2. We obtained strain distribution from Abaqus/Standard when the Arc-length is 50, as shown in Figure 6.3.

The strain distribution we used is obtained from Abaqus/Standard immediately, named as the logarithmic strain (LE). The logarithmic strain can be calculated as below in Abaqus/Standard,

$$\epsilon^L = \alpha \ln \mathbf{V} = \alpha \left(\sum_{i=1}^3 \ln \lambda_i \mathbf{n}_i \mathbf{n}_i^T \right) \quad (6.2.1)$$

where \mathbf{V} is the left stretch tensor, λ_i are the principal stretches, and \mathbf{n}_i are the principal stretch directions. α is a negative or positive constant, with regards to the bone formation and resorption, respectively. These nonlinear analysis were still performed with Abaqus 6.12 Edition (Abaqus, Inc.).

After the nonlinear post-buckling analysis from Chapter 5.2, the Max principle logarithmic strain in each element distribution when

Arc-length $\lambda = 50$ could be obtained from Abaqus/Standard. Increasing volume in proportion to the strain simulated bone formation, whereas decreasing volume simulated bone resorption. With the changing between positive or negative of α , the bone formation analysis and bone resorption analysis were produced.

6.3 Results and discussion

The result for bone formation from strain distribution is shown in Figure 6.6, and the result for bone resorption from strain distribution is shown in Figure 6.7. For bone formation, the spine model became straightly because of the thermal expansion. While, the scoliotic curves occurs when the model is in resorption condition, as shown in Figure 6.7. After the bone resorption analysis, the biggest spatial displacement near T7 is around 16.97 mm, as shown at the red triangle in Figure 6.7 (b). Thus, the bone resorption was similar to the clinical scoliotic curves. The results from this study suggest that scoliotic changes in the spinal column are caused by the buckling phenomenon. Moreover, scoliotic changes triggered by the buckling phenomenon are counteracted by bone formation, but worsened by bone resorption for computational investigation.

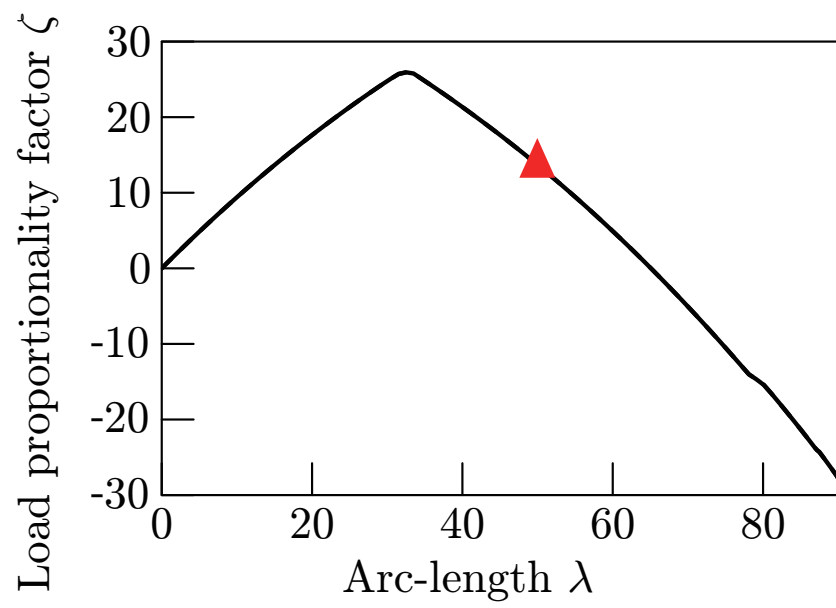


Figure 6.3: The point when Arc-length $\lambda = 50$

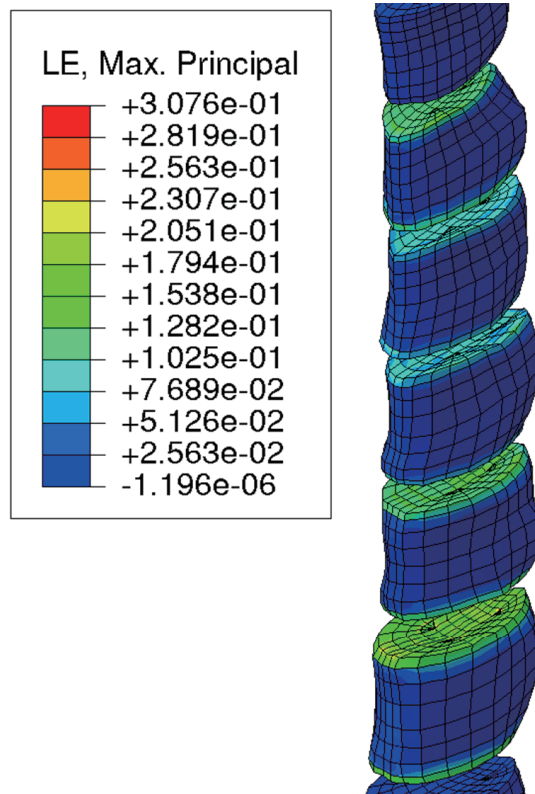


Figure 6.4: The strain distribution during nonlinear post-buckling analysis when Arc-length $\lambda = 50$

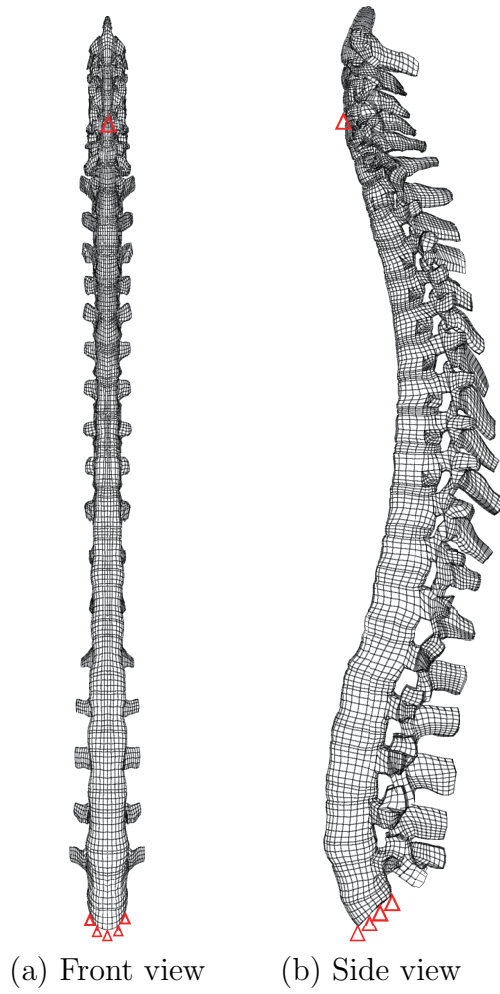


Figure 6.5: The boundary condition for bone remodeling analysis

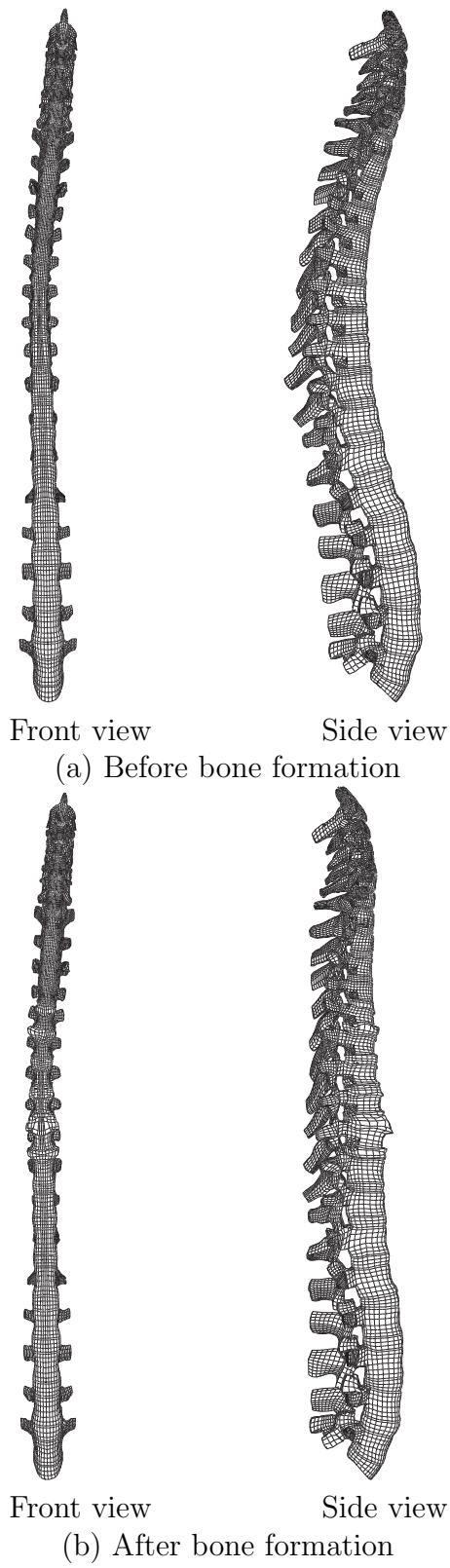


Figure 6.6: Comparison between before bone formation and after bone formation ($\lambda = 50$).

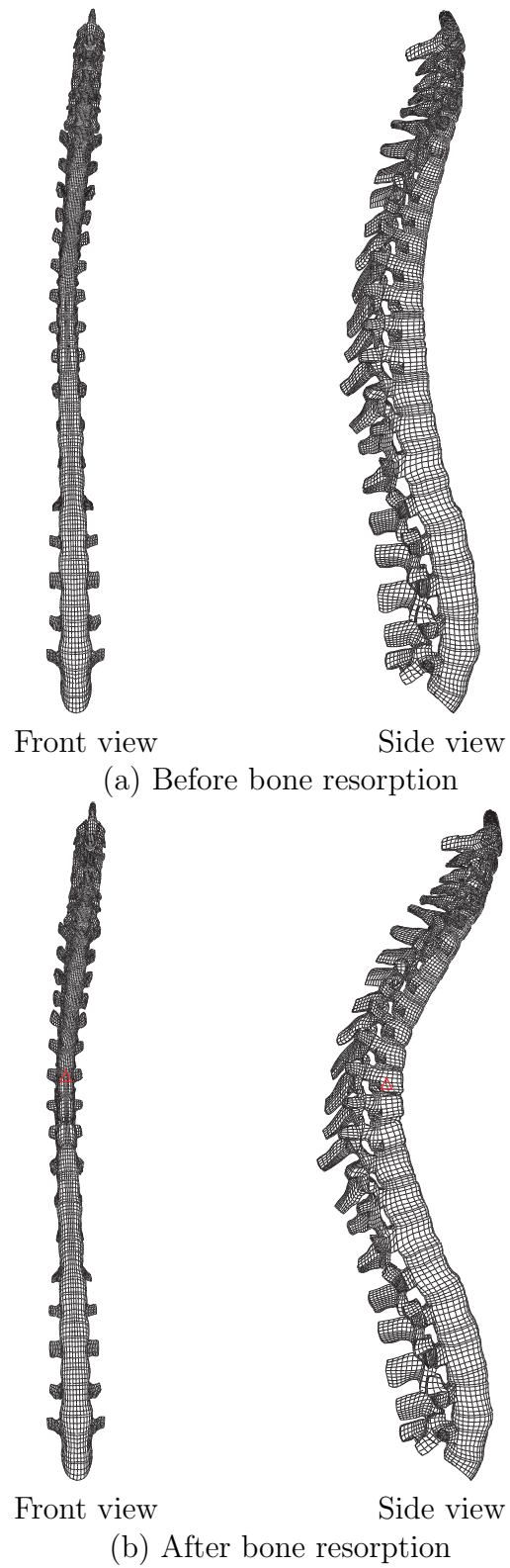


Figure 6.7: Comparison between before bone resorption and after bone resorption ($\lambda = 50$) (The biggest spatial displacement is around 16.97mm.)

6.4 Conclusion

In this chapter, in order to investigate the mechanism of progression of the idiopathic scoliosis, the influence of bone remodeling after the buckling was analyzed. From the results, it is confirmed that the bone formation corrects the original curve, while the bone resorption worsens the original curve. These results indicate that, the bone resorption with respect to strain at post-buckling can be a candidate of the developing mechanism of the idiopathic scoliosis.

Chapter 7

Conclusion

7.1 Achievement of this research

Idiopathic scoliosis still remains as a disorder of unknown etiology with a large number of hypotheses. A large number of hypotheses and physical models have been proposed for the pathogenesis of idiopathic scoliosis. We have focused on a hypothesis that idiopathic scoliosis is a buckling phenomenon induced by the growth of vertebral bodies. We tried to investigate the etiology and the developing mechanism of idiopathic scoliosis by means of computational mechanics.

The results of each chapter are summarized as below,

In Chapter 1, the features of idiopathic scoliosis, the treatment, and the various hypotheses on the etiology to cause idiopathic scoliosis were introduced at first. Especially, the background and information about the buckling hypothesis to cause idiopathic scoliosis was stated. The achievements and failures about the previous research on the buckling hypothesis from our research group was reviewed. At last the objective of this research was determined clearly.

In Chapter 2, we used simple plate models to confirm the existence of a buckling phenomenon that has various geometrical properties. We used three types of simple model having different properties to analyze linear buckling modes caused by the growth deformation, and we confirmed the existence of the buckling phenomena and clarified the range of the geometrical parameters in which this buckling occurs. By a comparison of different models, we investigated the influence of

the region of the buckling phenomena on the physiological curvature of the spine and the intervertebral articulation. Our results support buckling hypothesis that a flattening or reversal of normal thoracic kyphosis at the apex of the curvature of the spine causes the buckling phenomenon.

The result we obtained in Chapter 2 is valid for infinitesimal deformation and is not applicable to estimate the stability for nonlinear post-buckling behavior. In Chapter 3, we conducted nonlinear post-buckling simulations caused by the growth of vertebral bodies considering the geometrical nonlinearity using the simple plate model. After introducing initial imperfection to the buckling mode, stable deformations were obtained in almost modes of the simple plate model. Especially, for the 3rd Mode, an unstable deformation of the model during the analysis were obtained. From the nonlinear growth deformation analysis, the existence of the nonlinear buckling phenomena was confirmed in the simple plate model.

In Chapter 4, the finite element model of spine was used to complete the linear buckling analysis to investigate the buckling hypothesis. The new finite element model of spine which is more exact than the previous model was introduced. After the linear buckling analysis, the 4th Mode which is similar to the clinical scoliotic curves was obtained. We also tried to investigate the difficulty for the spine model to get buckled with respect to different growth regions. When the growth depth is around 10 mm, the smallest Load Proportionality Factor ζ_4 is recorded, which accords the results from the simple plate models in Chapter 2.

In Chapter 5, we conducted post-buckling simulations caused by the growth of vertebral bodies considering the geometrical nonlinearity using the spine models. However, we did not obtain any buckling phenomenon after introducing imperfections to the normal spine model. Thus, we shrank the width of the spine model, and fixed the node at the center of front boundary of C7 of the spine model considering the controllability of posture. Under this condition, the existence of the non-linear buckling phenomena was confirmed in the spine model with half width. Moreover, after the non-linear buckling phenomena, stable deformations were obtained for the spine model with half width. Thus, the pathogenesis of the onset in the idiopathic scoliosis can be

explained by the buckling hypothesis. However, the magnitudes of the post-buckling deformations are too small to explain the pathogenesis of the severe deformity observed in patients of idiopathic scoliosis. Thus, although the buckling hypothesis can explain the pathogenesis of the onset in the idiopathic scoliosis, it cannot explain the developing mechanism.

In Chapter 6, in order to investigate the mechanism of progression of the idiopathic scoliosis, the influence of bone remodeling on the buckling spine was investigated. The bone formation was simulated by increasing of the volume of the bone in proportion to the strain distribution which was obtained from the nonlinear post-buckling deformation analysis, and the bone resorption was simulated by decreasing of the volume of the bone in proportion to the strain distribution. From the results, the incremental deformation resulting from bone formation corrected the original curve. On the other hand, incremental deformation resulting from bone resorption worsened the original curve. These results suggested that, the bone resorption with respect to strain at post-buckling can be a candidate of the developing mechanism of the idiopathic scoliosis.

7.2 Future work

In this research, we used numerical results by FEM to investigate the effect of buckling phenomena in the etiology of idiopathic scoliosis. In the future, we hope this study could contribute to clinical applications for treatment and prevention of idiopathic scoliosis.

Various buckling modes obtained in this research explained the different types of clinical scoliotic shapes. Moreover, the finite element analysis in this study can be used to predict the symptom from the initial stage to the final stage for the patients without surgical treatment. Besides, these technology can be applied to predict the future development of scoliotic curve after surgery.

The improvement that should be made to enhance in this research are summarized as below.

- (1) The results of nonlinear analysis for bone resorption we obtained is too small to explain the pathogenesis of the severe deformity

observed in patients of idiopathic scoliosis. The future investigation is needed in order to obtain severe deformity like clinical scoliotic curves.

- (2) The accuracy of the finite element model of spine needs to be upgraded. In order to obtain better results, especially, the first-order triangular and tetrahedral elements should be improved.

Bibliography

- [1] Dorland. *Dorland's Illustrated Medical Dictionary (32nd ed.)*. Elsevier Saunders, 2012.
- [2] Carmine D. Clemente. *Anatomy A Regional Atlas of the Human Body 4th Edition*. Williams & Wilkins, Baltimore, 1997.
- [3] H. Sun and H. Azegami. Existence of buckling phenomena as a pathogenic mechanism of idiopathic scoliosis. *PathJournal of Biomechanical Science and Engineering*, Vol. 10, No. 2, pp. 14–00315, 2015.
- [4] R. Cobb. Outline for study of scoliosis. *American Academy of Orthopaedic Surgeons Instr Course Lectures*, Vol. 5, pp. 261–75, 1948.
- [5] 小野村敏信（編）. 脊椎・脊髄. 図説臨床整形外科講座 第1巻. メジカルビュー社, 1984.
- [6] Marie-Louise B Lenssinck, Astrid C Frijlink, Marjolein Y Berger, Sita MA Bierma-Zeinstra, Karin Verkerk, and Arianne P Verhagen. Effect of bracing and other conservative interventions in the treatment of idiopathic scoliosis in adolescents: a systematic review of clinical trials. *Physical therapy*, Vol. 85, No. 12, pp. 1329–1339, 2005.
- [7] Toru Maruyama, Theodoros B Grivas, and Angelos Kaspiris. Effectiveness and outcomes of brace treatment: a systematic review. *Physiotherapy theory and practice*, Vol. 27, No. 1, pp. 26–42, 2011.

- [8] Cathleen L Raggio. Sexual dimorphism in adolescent idiopathic scoliosis. *Orthopedic Clinics of North America*, Vol. 37, No. 4, pp. 555–558, 2006.
- [9] M. Ueno, M. Takaso, T. Nakazawa, T. Imura, W. Saito, R. Shintani, K. Uchida, M. Fukuda, K. Takahashi, S. Ohtori, et al. A 5-year epidemiological study on the prevalence rate of idiopathic scoliosis in tokyo: school screening of more than 250,000 children. *Journal of Orthopaedic Science*, Vol. 16, No. 1, pp. 1–6, 2011.
- [10] IGNACIO V Ponseti and Barry Friedman. Prognosis in idiopathic scoliosis. *J Bone Joint Surg Am*, Vol. 32, No. 2, pp. 381–395, 1950.
- [11] W.Y. Cheung and K. D. K. Luk. Focus on classification of adolescent idiopathic scoliosis. *The British Editorial Society of Bone and Joint Surgery*, pp. 1–4, 2013.
- [12] Theodoros B Grivas, Achilles Bountis, Irene Vrasami, and Nikolaos V Bardakos. Brace technology thematic series: the dynamic derotation brace. *Scoliosis*, Vol. 5, No. 1, p. 20, 2010.
- [13] H. A. King, J. H. Moe, D. S. Bradford, and R. B. Winter. The selection of fusion levels in thoracic idiopathic scoliosis. *J. Bone Joint Surg.*, Vol. 65, No. 9, pp. 1302–1313, 1983.
- [14] Roberto Padua, Sergio Padua, Lorenzo Aulisa, Enrico Ceccarelli, Luca Padua, Emilio Romanini, Gustavo Zanolli, and Andrea Campi. Patient outcomes after harrington instrumentation for idiopathic scoliosis: a 15-to 28-year evaluation. *Spine*, Vol. 26, No. 11, pp. 1268–1273, 2001.
- [15] 松山幸弘, 川上紀明, 松原裕二, 金村徳相, 荒尾和彦, 岩田久. 特発性側彎症の手術的治療における lenke 分類の意義: 特に king type ii に対して. 脊柱変形: 日本側彎症研究会会誌= Spinal deformity: the journal of Japanese Scoliosis Society, Vol. 16, No. 1, pp. 35–40, 2001.

- [16] L. G. Lenke. New comprehensive classification of adolescent idiopathic scoliosis. Scoliosis Research Society, 1997.
- [17] L. G. Lenke, K. H. Bridwell, D. H. Clements, T. G. Lowe, and H. I. Shufflebarger. Intraobserver and interobserver reliability of the classification of thoracic adolescent idiopathic scoliosis. *J. Bone Joint Surg.*, Vol. 80, No. 8, pp. 1097–1106, 1998.
- [18] L. G. Lenke, R. R. Betz, J. Harms, K. H. Bridwell, D. H. Clements, T. G. Lowe, and K. Blanke. Adolescent idiopathic scoliosis: a new classification to determine extent of spinal arthrodesis. *J. Bone Joint Surg.*, Vol. 83-A, No. 8, pp. 1169–1181, 2001.
- [19] O. Yaman and S. Dalbayrak. Idiopathic scoliosis. *Turkish neurosurgery*, Vol. 24, No. 5, pp. 646–657, 2013.
- [20] Thomas Niemeyer, Alexandra Wolf, Susanne Kluba, Henry F Halm, Klaus Dietz, and Torsten Kluba. Interobserver and intraobserver agreement of lenke and king classifications for idiopathic scoliosis and the influence of level of professional training. *Spine*, Vol. 31, No. 18, pp. 2103–2107, 2006.
- [21] 後藤学, 川上紀明, 松山幸弘, 川上寛, 稲生秀文, 吉原永武, 辻太一, 松原祐二, 金村徳相. 特発性側彎症に対する lenke 分類の検討. *脊柱変形*, Vol. 17, No. 1, pp. 34–38, 2002.
- [22] STUART L Weinstein, DC Zavala, and IV Ponseti. Idiopathic scoliosis: long-term follow-up and prognosis in untreated patients. *The Journal of Bone & Joint Surgery*, Vol. 63, No. 5, pp. 702–712, 1981.
- [23] Dale E Rowe, Saul M Bernstein, Max F Riddick, Federico Adler, John B Emans, and Daryle Gardner-Bonneau. A meta-analysis of the efficacy of non-operative treatments for idiopathic scoliosis*†. *The Journal of Bone & Joint Surgery*, Vol. 79, No. 5, pp. 664–74, 1997.
- [24] Y. Shimada, K. Sato, E. Abe, T. Kikuchi, and M. Yamamoto. Surface electrical stimulation for the treatment of idiopathic scoliosis. *脊柱変形*, Vol. 10, No. 1, pp. 104–109, 1995.

- [25] 宇野耕吉, 謝典穎, 白石英典, 司馬良一, 公文裕. 軽度側彎症に対する側彎体操 (アクティブコレクション法) の効果について. 脊柱変形, Vol. 10, No. 1, pp. 110–113, 1995.
- [26] 森下益多郎, 康野公則, 味八木次郎, 神崎浩二, 大屋裕志, 斎藤元. 軽度特発性側彎症に対する足底装具療法の検討. 脊柱変形, Vol. 10, No. 1, pp. 100–103, 1995.
- [27] 瀬本喜啓, 小野村敏信, 永田裕人, 濱本浩, 小坂理也, 岩井宏次. 新しい側彎矯正ギプス法の試み. 脊柱変形, Vol. 10, No. 1, pp. 100–103, 1995.
- [28] P. R. Harrington. Treatment of scoliosis, correction and internal fixation by spine instrumentation. *J. Bone Joint Surg.*, Vol. 44-A, pp. 591–661, 1962.
- [29] E. R. Luque. Segmental spinal instrumentation for correction of scoliosis. *Clin. Orthop.*, No. 163, pp. 192–198, 1982.
- [30] Y. Cotrel and J. Dubousset. A new technic for segmental spinal osteosynthesis using the posterior approach. *Rev. Chir. Orthop. Reparatrice Appar. Mot.*, Vol. 70, No. 6, pp. 489–494, 1984. (in French).
- [31] Y. Cotrel, J. Dubousset, and M. Guillaumat. New universal instrumentation in spinal surgery. *Clin. Orthop.*, No. 227, pp. 10–23, 1988.
- [32] Jeff Cassidy. Idiopathic scoliosis. In *JOURNAL OF BONE AND JOINT SURGERY-AMERICAN VOLUME*, Vol. 43, pp. 462–462. JOURNAL BONE JOINT SURGERY INC 20 PICKERING ST, NEEDHAM, MA 02192, 1961.
- [33] I. A. Stokes and M. Gardner-Morse. Three-dimensional simulation of Harrington distraction instrumentation for surgical correction of scoliosis. *Spine*, Vol. 18, No. 16, pp. 2457–2464, 1993.
- [34] M. Gardner-Morse and I. A. Stokes. Three-dimensional simulation of the scoliosis derotation maneuver with Cotrel-Dubousset instrumentation. *Spine*, Vol. 18, No. 16, pp. 2457–2464, 1993.

- [35] P. R. Harrington. The etiology of idiopathic scoliosis. *Clin. Orthop.*, No. 126, pp. 17–25, 1977.
- [36] Thomas G Lowe, Michael Edgar, Joseph Y Margulies, Nancy H Miller, V James Raso, Kent A Reinker, and Charles-Hilaire Rivard. Etiology of idiopathic scoliosis: Current trends in research*. *The Journal of Bone & Joint Surgery*, Vol. 82, No. 8, pp. 1157–1157, 2000.
- [37] Patrick Edery, Patricia Margaritte-Jeannin, Bernard Biot, Audrey Labalme, Jean-Claude Bernard, Joëlle Chastang, Behrouz Kassai, Marie-Helene Plais, Florina Moldovan, and Françoise Clerget-Darpoux. New disease gene location and high genetic heterogeneity in idiopathic scoliosis. *European Journal of Human Genetics*, Vol. 19, No. 8, pp. 865–869, 2011.
- [38] Angela MS Poon, Kenneth MC Cheung, D S Lu, and John CY Leong. Changes in melatonin receptors in relation to the development of scoliosis in pinealectomized chickens. *Spine*, Vol. 31, No. 18, pp. 2043–2047, 2006.
- [39] Keith M Bagnall, Murray Beuerlein, Paul Johnson, Janet Wilson, V James Raso, and Marc Moreau. Pineal transplantation after pinealectomy in young chickens has no effect on the development of scoliosis. *Spine*, Vol. 26, No. 9, pp. 1022–1027, 2001.
- [40] M. Machida, J. Dubousset, Y. Imamura, T. Iwaya, T. Yamada, and J. Kimura. Role of melatonin deficiency in the development of scoliosis in pinealectomised chickens. *J Bone Joint Surg Br.*, Vol. 77, No. 1, pp. 134–138, 1995.
- [41] M. Machida, J. Dubousset, Y. Imamura, Y. Miyashita, T. Yamada, and J. Kimura. A possible role in pathogenesis of adolescent idiopathic scoliosis. *Spine*, Vol. 21, No. 10, pp. 1147–1152, may 1996.
- [42] H Normelli, J Sevastik, and J Akriivos. The length and ash weight of the ribs of normal and scoliotic persons. *Spine*, Vol. 10, No. 6, pp. 590–592, 1985.

- [43] J. Sevastik, M. Agadir, and Sevastik B. Effects of rib elongation on the spine. Distortion of the vertebral alignment in the rabbit. *Spine*, Vol. 15, No. 8, pp. 822–825, 1990.
- [44] I. A. Stokes and J. P. Laible. Three-dimensional osseoligamentous model of the thorax representing initiation of scoliosis by asymmetric growth. *J. Biomechanics*, Vol. 23, No. 6, pp. 589–595, 1990.
- [45] Ian AF Stokes and Mack Gardner-Morse. Analysis of the interaction between vertebral lateral deviation and axial rotation in scoliosis. *Journal of biomechanics*, Vol. 24, No. 8, pp. 753–759, 1991.
- [46] Ian AF Stokes, Holly Spence, David D Aronsson, and Nicholas Kilmer. Mechanical modulation of vertebral body growth: implications for scoliosis progression. *Spine*, Vol. 21, No. 10, pp. 1162–1167, 1996.
- [47] Anne-Marie Huynh, Carl-Eric Aubin, Talib Rajwani, Keith M Bagnall, and Isabelle Villemure. Pedicle growth asymmetry as a cause of adolescent idiopathic scoliosis: a biomechanical study. *European Spine Journal*, Vol. 16, No. 4, pp. 523–529, 2007.
- [48] W. Adams. *Lectures on the Pathology and Treatment of Lateral and Other Forms of Curvature of the Spine*. John Churchill and Sons, London, 1865.
- [49] R. A. Dickson, J. O. Lawton, I. A. Archer, and W. P. Butt. The pathogenesis of idiopathic scoliosis biplanar spinal asymmetry. *J. Bone and Joint Surg.*, Vol. 60-B, No. 1, pp. 8–15, 1984.
- [50] R. A. Dickson. The etiology and pathogenesis of idiopathic scoliosis. *Acta orthopaedica belgica*, Vol. 58, pp. 21–25, 1991.
- [51] PA Millner and R. A. Dickson. Idiopathic scoliosis: biomechanics and biology. *European Spine Journal*, Vol. 5, No. 6, pp. 362–373, 1996.

- [52] Richard W Porter. Idiopathic scoliosis: the relation between the vertebral canal and the vertebral bodies. *Spine*, Vol. 25, No. 11, pp. 1360–1366, 2000.
- [53] Winnie CW Chu, Wynnie WM Lam, Yu-leung Chan, Bobby KW Ng, Tsz-ping Lam, Kwong-man Lee, Xia Guo, and Jack CY Cheng. Relative shortening and functional tethering of spinal cord in adolescent idiopathic scoliosis?: study with multiplanar reformat magnetic resonance imaging and somatosensory evoked potential. *Spine*, Vol. 31, No. 1, pp. E19–E25, 2006.
- [54] T. Shinoda and S. Murachi. Growth of children and idiopathic scoliosis (Consideration on etiology of scoliosis) (in Japanese). In *Kobatohakuen no ayumi*, Vol. 6, pp. 11–32. Aichi Human Service Center, Kasugai, Japan, 1976.
- [55] T. Shinoda and S. Murachi. Pathogenesis of idiopathic scoliosis (On the cage theory) (in Japanese). In *Kobatohakuen no ayumi*, Vol. 7, pp. 4–12. Aichi Human Service Center, Kasugai, Japan, 1977.
- [56] H. Azegami, S. Murachi, J. Kitoh, Y. Ishida, N. Kawakami, and M. Makino. Etiology of idiopathic scoliosis: Computational study. *Clinical Orthopaedics and Related Research*, Vol. 357, pp. 229–236, 1998.
- [57] K. Takeuchi, H. Azegami, R. Sasaoka, S. Murachi, J. Kitoh, Y. Ishida, N. Kawakami, M. Goto, M. Makino, and Y. Matsuyama. Numerical simulation on etiology of idiopathic scoliosis: Modal investigation. spinal deformity. *The Journal of Japanese Scoliosis Society, (in Japanese)*, Vol. 16, No. 1, pp. 11–16, 2001(in Japanese).
- [58] T. Aoyama, H. Azegami, and N. Kawakami. Nonlinear buckling analysis for etiological study of idiopathic scoliosis. *Journal of Biomechanical Science and Engineering*, Vol. 3, No. 3, pp. 399–410, 2008.

- [59] D. B. Lucas and B. Bresler. Stability of the ligamentous spine. Biomechanics laboratory rpt., Univ. of California, San Francisco, 1961.
- [60] Robert B Winter, F Denis, John E Lonstein, J Garamella, JE Lonstein, and JH Moe. Moe's textbook of scoliosis and other spinal deformities. *Philadelphia Saunders*, pp. 39–43, 1995.
- [61] 竹内謙善, 畔上秀幸, 村地俊二, 鬼頭純三, 石田義人, 川上紀明, 牧野光倫. 特発性側彎症の成因に関する数値シミュレーション—数値モデルの精密化—. 脊柱変形, Vol. 14, No. 1, pp. 25–28, 1999.
- [62] Dassault Systemes Simulia Corp. Analysis user 's manual. volume ii: Analysis. *Abaqus Version 6.12*, 2012.
- [63] Inc. Altair Engineering. Radioss theory manual 11.0 version. *Altair Engineering, Inc.*, 2011.
- [64] 川井忠彦. 座屈問題解析. コンピュータによる構造工学講座 II-6-B. 培風館, 1974.
- [65] T. Kawai and Y. Fujitani, editors. *Buckling problem analysis (in Japanese)*. Baifukan Co., Ltd., Tokyo, 2013.
- [66] K. Takeuchi, H. Azegami, S. Murachi, J. Kitoh, Y. Ishida, N. Kawakami, and M. Makino. Computational study on the etiology of idiopathic scoliosis: Buckling hypothesis induced by bone modeling against gravity. *Transactions of JSCEs, (in Japanese)*, Vol. 4, pp. 153–160, 2002.
- [67] E Riks. An incremental approach to the solution of snapping and buckling problems. *International Journal of Solids and Structures*, Vol. 15, No. 7, pp. 529–551, 1979.
- [68] Seung-Jung Lee, Gukgwon Choi, Ilhwan You, Min Han Oh, Nayoung Kim, Goangseup Zi, Soye Kim, et al. Evaluation of buckling strength for design consideration of offshore structures. In *The Twenty-fifth International Offshore and Polar Engineering Conference*. International Society of Offshore and Polar Engineers, 2015.

- [69] H. Noguchi and T. Hisada. Development of a new branch-switching algorithm in nonlinear fem using scaled corrector. *JSME international journal. Series A, mechanics and material engineering*, Vol. 37, No. 3, pp. 255–263, 1994.
- [70] 久田俊明, 野口裕久. 非線形有限要素法の基礎と応用. 丸善, 1995.
- [71] A. Schäffler and S. Schmidt. からだの構造と機能. 西村書店, 1998. 三木明德 井上貴央 監訳.
- [72] 畔上秀幸, 村地俊二, 石田義人, 鈴木隆之, 川上紀明, 牧野光倫, 荒尾和彦, 鬼頭浩史. 特発性側彎症に関する数値シミュレーション. 脊柱変形, Vol. 10, No. 1, pp. 16–19, 1995.
- [73] 畔上秀幸, 村地俊二, 鬼頭純三, 石田義人, 川上紀明, 牧野光倫. 特発性側彎症に関する数値シミュレーション — 胸郭モデルを用いた検討 —. 脊柱変形, Vol. 11, No. 1, pp. 9–12, 1996.
- [74] H. Azegami and Z. C. Wu. Domain optimization analysis in linear elastic problems (approach using traction method). *JSME Int. J. Series A*, Vol. 39, No. 2, pp. 272–278, 1996.
- [75] 林英和. 脊柱側弯症の成因に関する解析的研究. 修士論文, 豊橋技術科学大学, 1995.
- [76] 前久保義明. 脊柱側弯症成因解明のための有限要素解析モデルの精密化に関する研究. 修士論文, 豊橋技術科学大学, 1996.
- [77] 上田高行. 特発性側弯症成因解明のための大変形を考慮した数値シミュレーション. 修士論文, 豊橋技術科学大学, 1997.
- [78] 鈴木隆之. 脊柱側弯症発生メカニズムの解明に関する研究. 修士論文, 豊橋技術科学大学, 1994.
- [79] 畔上秀幸, 竹内謙善, 村地俊二, 鬼頭純三, 石田義人, 川上紀明, 牧野光倫. 特発性側彎症の成因に関する数値シミュレーション — 数値モデルの精密化 —. 第32回日本側彎症学会演題抄録集, p. 43, 1998.

- [80] 笹岡竜, 竹内謙善, 畔上秀幸, 村地俊二, 鬼頭純三, 石田義人, 川上紀明, 牧野光倫, 松山幸弘, 後藤学, 稲生秀文, 吉原永武. 特発性側彎症の成因に関する力学模型実験 — 精密な脊柱力学模型を用いた検討 —. 第35回日本側彎症学会演題抄録集, p. 68, 2001.
- [81] 笹岡竜, 畔上秀幸, 川上紀明. 脊柱力学模型による特発性側彎症の成因解明. 日本機械学会第15回バイオエンジニアリング講演会講演論文集. n. 02-35, 2002, p. 179-180, 2003.
- [82] 畔上秀幸. 領域最適化問題の一解法. 日本機械学会論文集 (A編), Vol. 60, No. 574, pp. 1479-1486, 1994.
- [83] 畔上秀幸, 呉志強. 線形弾性問題における領域最適化解析 (手法によるアプローチ). 日本機械学会論文集 (A編), Vol. 60, No. 578, pp. 2312-2318, 1994.
- [84] 畔上秀幸, 村地俊二, 鬼頭純三, 石田義人, 川上紀明, 牧野光倫. 特発性側彎症に関する力学模型実験. 脊柱変形, Vol. 13, No. 1, pp. 29-32, 1998.
- [85] H. Azegami, et al. Shape optimization with respect to buckling. In *Computer Aided Optimization Design of Structures VI*, pp. 57-66. WIT Press, Southampton, 1999.
- [86] 竹内謙善, 畔上秀幸, 村地俊二, 鬼頭純三, 石田義人, 川上紀明, 牧野光倫. 特発性側彎症に対する感度解析 — 構造最適化理論の応用 —. 第33回日本側彎症学会演題抄録集, p. 44, 1999.
- [87] 竹内謙善, 笹岡竜, 畔上秀幸, 後藤学, 川上紀明. 脊柱特発性側彎症における胸郭変形の成因. 第12回計算力学講演会 講演論文集, No. 99-5, pp. 709-710, 1999.
- [88] 日本エムエスシー株式会社. MSC/NASTRAN ユーザーガイド 線形静解析 (V68), 1994.
- [89] 日本エムエスシー株式会社. MSC/NASTRAN ユーザーガイド 非線形解析ハンドブック, 1994.
- [90] 竹内謙善, 畔上秀幸, 笹岡竜, 村地俊二, 鬼頭純三, 石田義人, 川上紀明, 後藤学, 牧野光倫, 松山幸弘. 特発性側彎症の成因に関する

- る数値シミュレーション — 多様なモードの成因—. 第34回日本側彎症学会演題抄録集, p. 49, 2000.
- [91] 竹内謙善, 笹岡竜, 畔上秀幸, 村地俊二, 鬼頭純三, 石田義人, 川上紀明, 牧野光倫. 脊柱特発性側彎症の成因に関する計算力学的研究 (重力に抗する骨構築に起因した座屈説). 日本計算工学会論文集, 2002. Paper No.20020006.
- [92] 竹内謙善, 畔上秀幸, 村地俊二, 鬼頭純三, 石田義人, 川上紀明, 牧野光倫. 特発性側彎症に対する感度解析 — 構造最適化理論の応用 —. 脊柱変形, Vol. 15, No. 1, pp. 24–27, 2000.
- [93] K. Takeuchi, H. Azegami, S. Murachi, J. Kitoh, Y. Ishida, N. Kawakami, and M. Makino. Sensitivity analysis with respect to idiopathic scoliosis: Application of structural optimization. In *Proceedings of the Eleventh International Conference on Mechanics in Medicine and Biology*, pp. 143–146, April 2000.
- [94] 竹内謙善, 笹岡竜, 畔上秀幸, 川上紀明. 脊柱特発性側彎症の治療法に関する検討 (座屈説に基く感度解析). 日本機械学会 2000年度年次大会講演論文集, 第1巻, pp. 487–488, 2000.
- [95] K. Takeuchi, H. Azegami, S. Murachi, J. Kitoh, Y. Ishida, N. Kawakami, and M. Makino. Study on treatment with respect to idiopathic scoliosis (sensitivity analysis based on buckling theory). *JSME International Journal Series C*, Vol. 44, No. 4, 2001.
- [96] 笹岡竜. 特発性脊柱側彎症の成因解明を目的とした脊柱力学模型の構築. 修士論文, 豊橋技術科学大学, 2000.
- [97] 笹岡竜, 竹内謙善, 畔上秀幸, 村地俊二, 鬼頭純三, 石田義人, 川上紀明, 牧野光倫, 松山幸弘, 後藤学, 稲生秀文, 吉原永武. 脊柱特発性側彎症の成因に関する力学模型実験 — 精密な脊柱力学模型を用いた検討 —. 脊柱変形, 日本側彎症学会誌, Vol. 17, No. 1, pp. 18–22, 2002.
- [98] R. Sasaoka, H. Azegami, S. Murachi, J. Kitoh, Y. Ishida, N. Kawakami, M. Makino, and Y. Matsuyama. Investigation of buckling phenomenon induced by growth of vertebral bodies

- using a mechanical spine model. *JSME International Journal Series C*, Vol. 46, No. 4, pp. 1382–1387, 12 2003.
- [99] 青山大樹, 畔上秀幸. 2114 脊柱特発性側彎症の成因に関する非線形座屈解析 (os-21c 計算バイオメカニクスとその応用 (硬組織の計算バイオメカニクス), os-21 計算バイオメカニクスとその応用). 計算力学講演会講演論文集, Vol. 2005, No. 18, pp. 221–222, 2005.
- [100] 青山大樹, 畔上秀幸, 村地俊二, 鬼頭純三, 石田義人, 川上紀明, 牧野光倫. 特発性側彎症の成因解明のための成長シミュレーション. 脊柱変形: 日本側彎症研究会会誌 = Spinal deformity: the journal of Japanese Scoliosis Society, Vol. 22, No. 1, pp. 3–7, 2007.
- [101] 青山大樹, 畔上秀幸. 脊柱特発性側彎症の成因解明のための非線形座屈解析. 理論応用力学講演会 講演論文集, Vol. 56, No. 0, pp. 85–85, 2007.
- [102] H. Yamada. *Strength of Biological Materials*. Williams & Wilkins, Baltimore, 1970.
- [103] K.L. Markolf. Deformation of the thoracolumbar intervertebral joints in response to external loads. *J. Bone and Joint Surg.*, Vol. 54-A, No. 3, pp. 511–533, apr 1972.
- [104] A. B. Schultz, D. R. Benson, and C. Hirsch. Force deformation properties of human cost-sternal and cost-vertebral articulations. *J. Biomechanics*, Vol. 7, pp. 311–318, 1974.
- [105] 孫涵, 畔上秀幸. 特発性側彎症発症メカニズムの非線形座屈解析による検討. 日本機械学会論文集, Vol. 81, No. 830, 2015.
- [106] A. E. Nehme, E. J. Riseborough, and R. B. Reed. Normal spine growth. In *Scoliosis 1979*, pp. 103–109. Academic Press, 1980.
- [107] Ehab Ellobody, Ran Feng, and Ben Young. *Finite Element Analysis and Design of Metal Structures*. Elsevier, 2013.
- [108] Y. C. Fung. *Biomechanics: Motion, Flow, Stress, and Growth*. Springer-Verlag, New York, 1990.

- [109] J. Wolff. Über die innere architektur der knochen und ihre bedeutung für die frage vom knochenwachstum. *Archiv für pathologische Anatomie und Physiologie und für klinische Medizin, Virchows Archiv*, Vol. 50, pp. 389–453, 1870.
- [110] C. T. Mehlman, A. Araghi, and D. R. Roy. Hyphenated history: the Hueter-Volkman law. *American journal of orthopedics (Belle Mead, NJ)*, Vol. 26, No. 11, pp. 798–800, 1997.
- [111] H. M. Frost. Skeletal structural adaptations to mechanical usage (satmu): 1. redefining Wolff's law: the bone modeling problem. *The Anatomical Record*, Vol. 226, No. 4, pp. 403–413, 1990.
- [112] H. M. Frost. Skeletal structural adaptations to mechanical usage (satmu): 2. redefining Wolff's law: the remodeling problem. *The anatomical record*, Vol. 226, No. 4, pp. 414–422, 1990.
- [113] H. M. Frost. Skeletal structural adaptations to mechanical usage (satmu): 3. the hyaline cartilage modeling problem. *The Anatomical Record*, Vol. 226, No. 4, pp. 423–432, 1990.
- [114] H. M. Frost. Bone “mass” and the “mechanostat”: a proposal. *The anatomical record*, Vol. 219, No. 1, pp. 1–9, 1987.
- [115] H. M. Frost. Bone's mechanostat: a 2003 update. *The Anatomical Record Part A: Discoveries in Molecular, Cellular, and Evolutionary Biology*, Vol. 275, No. 2, pp. 1081–1101, 2003.
- [116] F. Pauwels. Biomechanics of the locomotor apparatus: contribution on the functional anatomy of the locomotor apparatus. *Berlin: Spfinger-Verlag*, 1980.
- [117] B. K. E. Kummer. Biomechanics of bone: mechanical properties, functional structure, functional adaptation. In Y. C. Fung, N. Perrone, and M. Anliker, editors, *Biomechanics: Its Foundations and Objectives*, pp. 237–271. Prentice-Hall, Englewood Cliffs, N.J., 1972.
- [118] S.C. Cowin and D.H. Hegedus. Bone remodeling I: theory of adaptive elasticity. *Journal of Elasticity*, Vol. 6, No. 3, pp. 313–326, 1976.

- [119] William Frederick Neuman, Margaret W Neuman, et al. The chemical dynamics of bone mineral. *The chemical dynamics of bone mineral.*, 1958.
- [120] 後藤学, 川上紀明, 松原祐二, 金村徳相, 畔上秀幸, 竹内謙善, 笹岡竜, 松山幸弘. 特発性側彎症発生における座屈と骨リモデリングの関与 ～有限要素法を用いた検討～. 第33回日本側彎症学会演題抄録集, p. 45, 1999.
- [121] 後藤学, 川上紀明, 松原祐二, 金村徳相, 畔上秀幸, 竹内謙善, 笹岡竜, 松山幸弘. 特発性側彎症発生における座屈と骨リモデリングの関与 ～有限要素法を用いた検討～. 脊柱変形, Vol. 15, No. 1, pp. 28–31, 2000.
- [122] M. Goto, N. Kawakami, H. Azegami, Y. Matsuyama, K. Takeuchi, and R. Sasaoka. Buckling and bone modeling as factors in the development of idiopathic scoliosis. *Spine*, Vol. 28, No. 4, pp. 364–370, 2003.

Acknowledgement

I have worked as a Ph.D. student in the Department of Complex Systems Science at Graduate School of Information Science, Nagoya University for a period of three years.

At the completion of this thesis, first and foremost, I am deeply grateful to my supervisor professor, Prof. Hideyuki AZEGAMI (Nagoya University), who provided me with patient guidance and unflinching encouragement during my research. Without your assistance and dedicated involvement in every step throughout the process, this research would have never been accomplished. I would like to thank you very much for your support and understanding over these past three years.

I would also like to thank to Prof. Takashi WATANABE (Nagoya University), Prof. Masahiro OHKA (Nagoya University), and Prof. Noriaki KAWAKAMI (Meijo Hospital, Spine Center, Nagoya), whose meticulous comments were an enormous help to me.

Moreover, I thanks all the members in Azegami Laboratory for giving me so much help and light up my life here.

Finally, I would also like to express my gratitude to my dear family for their moral support and warm encouragements.

January 2016
Han SUN